

INTERFACIAL PHENOMENA IN ION IMPLANTED
SILICON-ON-INSULATOR MATERIALS

By

ANTONIO FERNANDO SAAVEDRA

A DISSERTATION PRESENTED TO THE GRADUATE SCHOOL
OF THE UNIVERSITY OF FLORIDA IN PARTIAL FULFILLMENT
OF THE REQUIREMENTS FOR THE DEGREE OF
DOCTOR OF PHILOSOPHY

UNIVERSITY OF FLORIDA

2004

Copyright 2004

by

Antonio Fernando Saavedra

This dissertation is dedicated my family, as well as the mentors who supported and influenced me throughout my educational endeavors.

ACKNOWLEDGMENTS

Henry David Thoreau said, "I would rather sit on a pumpkin and have it all to myself than be crowded on a velvet cushion." Such would describe how I have tried to live and work over the years. Anyone who truly knows me recognizes this sense of independence in my being. Nonetheless, a study so vast can only be undertaken with contributions from several sources.

I must begin by recognizing those individuals that had the most profound influence on my character. My parents, Antonio and Monica, instilled in me the moral and ethical values which I try, often failing, to live by. My father immigrated to the United States from Bolivia in 1969 without the ability to formulate sentences in English. Diligent work allowed him to become a respected scientist in aluminum casting technology, which he passed on to me. Oddly enough, I became the third generation metallurgist in the family, all having the same first name, Antonio. Maybe he planned it, maybe he did not; I have no complaints. Monica has always provided a source of support over the years that I can never repay or fully appreciate. She believed in me even when I felt no one else did. My mother's parents, Howard and Gladys, were pleased to provide a safe haven from home any time we chose. I will never forget the wonderful, relaxing times spent on their farm. Jose and Ruth, on my father's side, were the grandparents to the south that I hope to see more of in the future. Although oral communication is difficult due to my broken Spanish, our love is not bound. Vacation to their home in Bolivia made me appreciate the opportunities I had, yet taught me respect for all cultures no matter the mainstream perception. My brother, Luie, remains a formidable opponent in professional-style wrestling every time we meet, but knows to avoid the "Power of Tone" whenever possible. His

appreciation for "B" movies (e.g., *American Ninja*, various Chuck Norris titles, etc.) is rivaled only by mine. Ximena and Tania, my sisters, were always there to keep me in line when the parents were not around. I could rely on them to snitch me out whenever I chose to go into a creative dialogue of four-letter words. However, their love and kindness are unmatched by any other duo. My godson, Luke, has been an inspiration since his birth and makes me want to go back to wearing diapers. I must also recognize my sister-in-law, Sharon, and brothers-in-law, Ronnie and Dewey, for putting up with me. Although too numerous to include, I must acknowledge the aunts, uncles, and cousins in both hemispheres. They all hold special places in my heart.

The congregation at First United Methodist Church in Sheffield, Alabama, made me feel welcome every Sunday. My youth and choir director, Oliver Brazeale, exhibited patience on more than one occasion as we prepared for choir tour. The fondest memories of my life were the times spent touring around the country without any responsibility. Oliver's sacrifices can never be put into context. The members of the youth group were always a joy to be around and will remain friends forever. I single out Ged Grimmitt, Brad Bernard, Adam Littrell, Tyler and Matt Jones, for their continual friendship and look forward to our travels in the future.

I must also recognize the mentors I had in the Muscle Shoals City School System, particularly Robert Young for helping me grasp the fundamentals of algebra. By doing this he put me on the path to becoming an engineer. I cannot begin to thank the faculty in the Department of Metallurgical and Materials Engineering at the University of Alabama including Drs. Richard Bratt, Viola Acoff, Mark Weaver, John Barnard, Tom Piwonka, Nagy El-Kaddah, Garry Warren, Ramana Reddy, Doru Stefanescu, and Giovanni Zangari. They provided me with what I consider to be a true materials engineering education. Rather than sticking strictly

to a structure-properties curriculum, they taught me to think like an engineer by instilling the fundamentals of mass and energy balances, process controls, and transport phenomena. Unfortunately, current materials science and engineering education seems to only give the students the facts they should memorize rather than pushing an analytical thought process. One man, Dr. James Weston, showed me "the ropes" of engineering when I was an undergraduate. His patience was greatly appreciated and the knowledge I gained by looking over his shoulder is irreplaceable. I also acknowledge my officemates Dr. Tom Scharf, Dr. Kevin Minor, Dr. Jonathan Grant, Chris Hale, and Feng Huang, for providing an enjoyable work environment. Classmates Brett Standifer, Bill Lapp, Brian Floyd, Bobby Roberts, and Kelly Crawford, made MTE classes one of a kind.

Numerous people have been directly involved with my research at the University of Florida. I begin by acknowledging my committee members Drs. Paul Holloway and Cammy Abernathy for taking the time to follow my progress and providing guidance. The help of Dr. Michael Kaufman for providing TEM knowledge and suggestions is also appreciated. Dr. Valentin Craciun was indispensable for teaching me much of what I know about HRXRD, and his service on my committee is recognized. My advisors, Drs. Kevin Jones and Mark Law, have been instrumental in my scientific growth. They allowed me to work independently and skip weekly meetings without consequence; what else can I ask for? I also acknowledge the friends and colleagues of the SWAMP Center. Dr. Lahir Adam became a great friend as soon as I arrived in Gainesville and I miss his driving and goofiness. Dr. Ibrahim Avel, Russ Robison, Ljubo Radic, and Dr. Susan Earles provided help with modeling as well as good laughs. Dr. Patrick Keys instructed me in the art of TEM, for which I am very grateful. Dena Wrigley, Jackie Frazier, and Andrew King helped with some of the PTEM sample preparation. Robert

Crosby, Dr. Aaron Lilak, Dr. Chad Lindfors, Heather Randall, Renata Camillo-Castillo, Diane Hickey, Michelle Phen, and others helped balance the work environment. I am grateful for the secretarial staff including Sharon Carter and Teresa Stevens, who sent countless FedEx shipments and handled many travel reimbursements with a smile.

Finally, I must thank IBM and the Semiconductor Research Corporation for providing funding for my project. Dr. Kevin Chan was as an excellent mentor during my summer at Yorktown and his help in material processing is appreciated. Drs. Erin Jones and Omer Dokumaci are acknowledged for serving as my SRC liaisons and also providing material support. The work of the ASTL South laboratory including Chris D'Emic, Ray Sicina, Phil Saunders, Ed Sikorski, and Joe Newberry also aided with processing. Lastly, I recognize Mikhail Klimov from the University of Central Florida for providing SIMS analysis.

TABLE OF CONTENTS

	Page
ACKNOWLEDGMENTS	iv
LIST OF TABLES	xii
LIST OF FIGURES	xiii
ABSTRACT	xxv
 CHAPTER	
1 MOTIVATION.....	I
1.1 Scaling of Planar CMOS.....	1
1.1.1 The Silicon Age and Moore's Law	1
1.1.2 Short Channel Effects	2
1.1.3 Other Problems	2
1.2 Silicon-on-Insulator (SOI) for CMOS	3
1.2.1 Advantages over Bulk Silicon	3
1.2.2 Challenges for SOI.....	4
1.3 Objectives and Statement of Thesis.....	5
 2 LITERATURE REVIEW	 13
2.1 Ion Implantation and Damage Recovery.....	13
2.1.1 Ion Stopping and Primary Defects	14
2.1.2 Secondary Defects and Their Structure.....	15
2.1.2.1 Submicroscopic interstitial clusters (SMICs).....	17
2.1.2.2 {311} defects	19
2.1.2.3 Dislocation loops.....	21
2.1.3 Models for Defect Evolution	23
2.2 Dopant Diffusion in Bulk Silicon	25
2.2.1 Mechanisms of Dopant Diffusion	25
2.2.2 Equilibrium Diffusion	27
2.2.3 Non-equilibrium/Enhanced Diffusion	28
2.2.4 TED of Boron	28
2.2.5 Boron Interstitial Clusters (BICs).....	29
2.3 Silicon-On-Insulator (SOI) Materials	31
2.3.1 SIMOX	31

2.3.2	SOITEC	33
2.4	Interstitial and Dopant Interactions at Si/SiO ₂ Interfaces	34
2.4.1	Si (001) Free Surface and Si(001)/SiO ₂ Interface Structure	34
2.4.1.1	Si(001)	35
2.4.1.2	SiO ₂	36
2.4.1.3	Si/SiO ₂ interface	37
2.4.2	Point Defect Interactions at the Si/SiO ₂ Interface	39
2.4.2.1	Interface effects on interstitial kinetics under oxidizing conditions	40
2.4.2.2	Interface effects on interstitial kinetics under non-oxidizing conditions and due to ion implantation	46
2.4.3	Models for Interstitial Interactions at Si/SiO ₂ Interfaces	49
2.4.4	Dopant Segregation in the Proximity of Si/SiO ₂ Interfaces	51
2.4.4.1	Thermodynamic considerations	51
2.4.4.2	Dynamic boundary conditions	52
2.4.4.3	Static boundary conditions	54
2.4.4.4	Consequences of dopant segregation	56
2.4.4.5	Models for dopant segregation	57
2.5	Dopant Diffusion in SOI	59
2.5.1	Boron Diffusion in SOI	59
2.5.2	Donor Diffusion in SOI	62
2.6	Summary	62
3	EXPERIMENTAL METHODOLOGY	113
3.1	Design of Experiments	113
3.1.1	Self-Interstitial Experiments	114
3.1.2	Boron Activation Experiments	115
3.2	Analytical and Simulation Techniques	116
3.2.1	Transmission Electron Microscopy (TEM)	116
3.2.2	Hall Effect	118
3.2.3	Four-Point Probe	121
3.2.4	Secondary Ion Mass Spectrometry (SIMS)	122
3.2.5	High Resolution X-Ray Diffraction (HRXRD)	123
3.2.6	UT-Marlowe	125
3.2.7	Florida Object Oriented Process Simulator (FLOOPS)	126
4	SELF-INTERSTITIAL EXPERIMENTS IN SOI	139
4.1	Introduction	139
4.2	Non-Amorphizing Implants	139
4.2.1	Interface Effects on {311} Defect Evolution	139
4.2.1.1	Experimental	140
4.2.1.2	Results	141
4.2.1.3	Discussion	143
4.2.1.4	Conclusions	146

4.2.2 Kinetics of {311} Defect Evolution in SOI.....	146
4.2.2.1 Experimental.....	146
4.2.2.2 Results.....	148
4.2.2.3 Discussion.....	149
4.2.2.4 Conclusions.....	151
4.2.3 Interface Effects on Dislocation Loop Evolution.....	151
4.2.3.1 Experimental.....	151
4.2.3.2 Results.....	152
4.2.3.3 Discussion.....	154
4.2.3.4 Conclusions.....	156
4.3 Amorphizing Implants.....	157
4.3.1 Experimental.....	157
4.3.2 Results.....	157
4.3.3 Discussion.....	159
4.3.4 Conclusions.....	160
4.4 Summary.....	161
 5 MODELING EXTENDED DEFECT EVOLUTION IN SOI.....	 203
5.1 Introduction.....	203
5.1.1 Model Background.....	203
5.1.2 Modeling Results.....	204
5.2 Summary.....	205
 6 INVESTIGATION OF BORON INTERSTITIAL CLUSTERING IN SOI.....	 211
6.1 Introduction.....	211
6.2 TEM Analysis of Boron Implanted SOI.....	212
6.2.1 Experimental.....	212
6.2.2 Results.....	213
6.2.3 Discussion.....	214
6.2.4 Conclusions.....	215
6.3 Time and Temperature Dependence of Boron Activation in SOI.....	215
6.3.1 Experimental.....	215
6.3.2 Results.....	217
6.3.3 Discussion.....	219
6.3.4 Conclusions.....	225
6.4 Concentration Dependence of Boron Activation in SOI.....	226
6.4.1 Experimental.....	226
6.4.2 Results and Discussion.....	227
6.4.3 Conclusions.....	229
6.5 Role of Strain on Boron Activation.....	230
6.5.1 Experimental.....	230
6.5.2 Results and Discussion.....	231
6.5.3 Conclusions.....	235

6.6 Relationship Between Boron Segregation and TED.....	235
6.6.1 Experimental.....	235
6.6.2 Results and Discussion.....	236
6.6.3 Conclusions	238
6.7 Summary	238
7 SUMMARY AND FUTURE WORK	278
7.1 Summary	278
7.2 Future Work.....	280
7.2.1 Local Electrode Atom Probe (LEAP) for Monitoring Dopant Segregation in SOI	280
7.2.2 Modification of Surface Potential Using a MOS Capacitor Structure.....	281
7.2.3 Critical Amorphization Depth in SOI	281
7.2.4 Concentration Threshold for BIC Formation in SOI	282
7.2.5 N-Type Dopants in SOI.....	282
APPENDIX	
A QUANTITATIVE TEM FOR MEASURING TRAPPED INTERSTITIAL POPULATIONS	285
B FLOOPS CODE FOR SIMULATION OF {311} DEFECTS IN SOI	288
LIST OF REFERENCES.....	292
BIOGRAPHICAL SKETCH	306

LIST OF TABLES

<u>Table</u>	<u>page</u>
1-1. Advantages and disadvantages of SOI devices over bulk silicon [IBI03].....	10
2-1. Advantages and disadvantages of ion implantation compared to gas source and solid source diffusion.	64
2-2. Approximate fractional interstitial and vacancy components for various dopants in Si. .	74
2-3. Advantages and disadvantages of the SIMOX process.	78
2-4. Advantages and disadvantages of using Smart-cut process for fabrication of SOI substrates.	79
2-5. Segregation coefficients determined for various impurities in Si during oxidation.....	99
3-1. Implant conditions and anticipated defect microstructures of interest in current self-interstitial experiments. Shaded boxes indicate implant conditions that were actually studied. Note: microstructures are only valid for bulk Si.	128
3-2. Insight gained from analytical techniques with regards to the BIC evolutionary process and boron segregation in SOL.	132
4-1. Equivalent annealing times assuming 3.7 eV activation energy for {311} defects in bulk Si.	175
4-2. Ion range statistics determined using UT-Marlowe and SRIM simulations.....	176
4-3. Dose loss for 750 Å and 1450 Å SOI determined using UT-Marlowe.	177
4-4. Extracted activation energies from Figure 4-18 for SIMOX, SOITEC and bulk Si.	183

LIST OF FIGURES

Figure	page
1-1. Schematic of bulk silicon MOSFET device showing different ion implanted areas within device [JON98].	7
1-2. Moore's Law describing scaling of the number of transistors on a chip [MOO65].	8
1-3. Applications for varying surface Si and BOX thickness [SIG03].	9
1-4. Comparison of operating characteristics for SOI and bulk CMOS [IBM03].	11
1-5. Schematic of CMOS cross section illustrating elimination of latchup path in SOI [COL97].	12
2-1. Schematic of collision cascade produced by light ions (e.g. atomic weight less than Si) and heavy ions (e.g. atomic weight greater than Si).	65
2-2. Evolutionary path for point defects produced by ion implantation.	66
2-3. Formation energy as a function of cluster size for self-interstitial defects in Si. Closed diamonds represent formation energy for a compact cluster, while the open triangles are for an elongated cluster [KIM00].	67
2-4. Formation energy as a function of cluster size as determined by Cowern et al., [COW99a].	68
2-5. 3D representation of {113} defect in Si lattice. Light gray balls show interstitial chains along <110> direction [TAK91].	69
2-6. Atomic structure of planar {113} defect. Numbers represent rings different from those in a perfect crystal [TAK94].	70
2-7. Plan view TEM (PTM) weak beam dark field (WBDF) micrograph of {311} defects in Si.	71
2-8. Formation criteria for extended defects in Si [JON88].	72
2-9. Mechanisms of dopant diffusion in the Si lattice [CRO95].	73

2-10. Enhanced and retarded diffusion of dopants under nitridation ambient conditions [FAH89].	75
2-11. Example of TED of boron due to the presence of {311} defects. Sample was implanted with boron at 19 keV, $3 \times 10^{14} \text{ cm}^{-2}$ and annealed at 750°C. The {311}s regulate the release of the excess interstitials until their eventual dissolution at longer times.	76
2-12. Energetics of evolutionary pathways for BIC formation [PEL99a].	77
2-13. Schematic of the SOITEC process [SOI03].	80
2-14. Surface reconstruction of Si (001) (1x1) to (2x1). Larger circles represent surface atoms, while smaller ones are one layer below [BAL88].	81
2-15. Schematic of vicinal Si(001) surface illustrating orientation of dimers on adjacent steps. Note existence of two different single-layer steps S_A and S_B [ZAN00].	82
2-16. STM microscope image of vicinal Si(001) surface misoriented 0.5° along the [110] direction. Alternating S_A and S_B steps are shown. Note smoothness of S_A steps and high density of kinks along S_B steps [ZAN00].	83
2-17. Structural basis of silicon dioxide – the SiO_4 tetrahedron. Note the constant tetrahedral angle and varying Si-O-Si bond angle [BAL88].	84
2-18. Phase diagram of crystalline forms of SiO_2 [BAL88].	85
2-19. Continuous random network of A_2B_3 glass, similar to that present in fused silica [CHI97].	86
2-20. Schematic illustration of Si/ SiO_2 interface with crystalline, cristobalite, form of SiO_2 . Note presence of transition region consisting of non-stoichiometric SiO_x [BAL88].	87
2-21. Structure of broken bond defects at the Si/ SiO_2 interface. (a) The E' defect consists of a broken bond between two tetrahedra that would otherwise be bonded to O. (b) The P_b center consists of a broken bond in Si that would be bonded to another Si atom [BAL88].	88
2-22. Schematic illustration of generation, diffusion, and recombination sources in SOI and bulk structures [CRO95].	89
2-23. Schematic of surface retrogrowth process proposed by Hu at an inert Si/ SiO_2 interface [HUS74, HUS94].	90

2-24. Schematic cross sections of test structures used by Ahn et al., for determining (a) 1-D and (b) 2-D interstitial kinetics [AHN87].	91
2-25. SOI structure used by Tsoukalas to study interstitial kinetics through an oxide (a) before backside etching of W1 and (b) after etching [TSO93].	92
2-26. Difference in OSF length between thinned structure and control as a function of oxidation time for range of temperatures [TSO93].	93
2-27. Test structures used by Tsamis to monitor (a) depth dependence of interstitial behavior and (b) lateral diffusion of interstitials under an oxidizing ambient [TSA95].	94
2-28. OSF length as function of distance from mask edge for SOI with varying surface Si thickness after (a) dry and (b) wet oxidation at 1100°C [TSA95]. Simulations were performed using data from Taniguchi [TAN85].	95
2-29. HRTEM micrograph showing zig-zag {311} defects produced by low energy Si ⁺ implantation at 5 keV, 3×10^{14} cm ⁻² . Sample was annealed at 810°C for 10 minutes [AGA97a].	96
2-30. PTM micrographs showing defect evolution after Ge ⁺ implantation at 5 keV and 10 keV, 1×10^{15} cm ⁻² . (a) 10 keV unlapped, (b) 10 keV lapped, and (c) 5 keV. Samples were annealed at 750°C for 60 minutes [KIN03].	97
2-31. Effect of impurity redistribution on segregation coefficient and diffusivity in SiO ₂ [GRO64a].	98
2-32. SIMS profiles of dopant segregation for (a) arsenic, (b) phosphorus, and (c) boron after oxidation at 1100 °C for 30 minutes [SAK87].	100
2-33. Temperature dependence of the segregation coefficient during oxidation for B, P, and As [SAK87].	101
2-34. Test structure used by Charitat and Martinez to investigate boron segregation at a static Si/SiO ₂ interface [CHA84].	102
2-35. Boron segregation coefficient as a function of temperature for <100> orientation under neutral annealing ambient. Stars indicate segregation coefficients for a Si surface covered with a pad oxide only. Circles indicate segregation coefficients for a Si surface covered with a pad oxide and nitride as shown in Fig. 2-34 [CHA84].	103

- 2-36. Boron segregation coefficient as a function of temperature for <111> orientation under neutral annealing ambient. Stars indicate segregation coefficients for a Si surface covered with a pad oxide only. Circles indicate segregation coefficients for a Si surface covered with a pad oxide and nitride as shown in Fig. 2-34 [CHA84].
..... 104
- 2-37. SIMS profiles of B, 0.5 keV, $1 \times 10^{15} \text{ cm}^{-2}$ annealed at 700 °C for 2 hours. Sample was preamorphized with Ge, 15 keV, $1.2 \times 10^{15} \text{ cm}^{-2}$. Note uphill diffusion of boron near surface, as well as gettering of boron to EOR damage around 34 nm [DUF03].
..... 105
- 2-38. Potential energy diagram for electrons in p-type Si following Ar^+ implantation. Interfacial defects absorb positive charge from the bulk and create a space charge region (SCR) and electric field pointing back into the bulk. Positively charged interstitials are repelled back into the bulk by the field. Interstitials close to the surface are able to recombine since the Fermi level approaches midgap [JUN04].
..... 106
- 2-39. Simulation of boron TED experiment using model of Jung *et al.* Note incorporation of surface band bending results in best fit to overall profile [JUN04]. 107
- 2-40. SIMS profiles of boron after BF_2 implantation at 40 keV, $1 \times 10^{14} \text{ cm}^{-2}$ into (a) 1986 and (b) 1988 SIMOX material. Anneals were 880 °C for 100 minutes in a nitrogen ambient. Note difference in pileup of boron at native oxide/surface Si interface [NOR90]. 108
- 2-41. SIMS profiles of B implanted at 10 keV, $1 \times 10^{13} \text{ cm}^{-2}$ into SOITEC substrates with surface Si thickness of 60-70 nm and BOX thickness of 200 nm. Top curves show Si signals obtained from SIMS. Following the B implant a 1050 °C, 60 second anneal was performed. Solid curves had an additional Si^+ implant at 40 keV, $5 \times 10^{13} \text{ cm}^{-2}$. Both samples were then annealed at 800 °C for 30 minutes. Note increased pileup at both interfaces with addition of Si^+ implant [VUO99]. 109
- 2-42. SIMS profiles of B marker layers grown on SOITEC substrates using MBE. Solid curves also had a Si^+ implant at 25 keV, $1 \times 10^{14} \text{ cm}^{-2}$. Note enhanced segregation of B to surface Si/BOX interface with addition Si^+ implant [VUO99]. 110
- 2-43. SIMS profiles of B from BF_2 implanted at 60 keV, $7 \times 10^{13} \text{ cm}^{-2}$ and annealed at 1000 °C for 5 sec in nitrogen. Surface Si thickness used were 530 Å, 1050 Å, and 1550 Å [PAR99]. 111

2-44. SIMS profiles of P implanted at 36 keV, $7 \times 10^{13} \text{ cm}^{-2}$ and annealed at 1000°C for 5 sec in nitrogen. Surface Si thickness used were 530 Å, 1050 Å, and 1550 Å [PAR99].....	112
3-1. Logic behind design of self-interstitial experiments. Implants are designated as amorphizing or non-amorphizing. Appropriately altering implant energy and dose allows observance of a particular extended defect.	127
3-2. Experimental methodology invoked in first self-interstitial study of {311} defects and dislocation loops for non-amorphizing implants. Samples were implanted at a fixed dose with energies varying from 5 to 40 keV. Anneals were performed at 750°C for times ranging from 5 minutes to 2 hours. Note: all substrates were fabricated using the SOITEC method.	129
3-3. Design of experiment 2 for determining kinetics of {311} defect evolution in SIMOX and SOITEC substrates.	130
3-4. Experiment 3 methodology for determining effect of surface Si/BOX interface on EOR dislocation loop formation.	131
3-5. Experimental design for first study of boron activation in SOI.	133
3-6. Design of second experiment for investigating kinetics of BIC dissolution in SOI and bulk Si.	134
3-7. Principle behind weak beam dark field imaging in TEM for a edge dislocation. High intensity occurs close to dislocation core because planes are bent back to Bragg condition. From [WIL96]	135
3-8. Illustration of Hall effect occurring in a p-type specimen. From [SCH98].....	136
3-9. Primary components of Philips X'Pert System with 6-axis goniometer. From [PAN04]	137
3-10. Optics setup for rocking curve analysis using Philips X'Pert system. (a) Primary optics – hybrid mirror and (b) secondary optics – triple axis detector. From [LIN04].....	138
4-1. UT-Marlowe ion profile simulations for Si^+ implants into (a) 750 Å and (b) 1450 Å SOI at 15, 30 and 48.5 keV, $1 \times 10^{14} \text{ cm}^{-2}$	162
4-2. Dose loss calculated from UT-Marlowe simulations for implant energies used in the study.	163

4-3. Weak beam dark field images of SOI and bulk silicon for Si^+ , 15 keV, $1 \times 10^{14} \text{ cm}^{-2}$ implants after annealing at 750 °C for 5 and 15 minutes.	164
4-4. Concentration of trapped interstitials in all extended defects for Si^+ , 15 keV, $1 \times 10^{14} \text{ cm}^{-2}$ annealed at 750 °C.	165
4-5. Weak beam dark field images of SOI and bulk silicon for Si^+ , 30 keV, $1 \times 10^{14} \text{ cm}^{-2}$ implants after annealing at 750 °C for 5 and 15 minutes.	166
4-6. Concentration of trapped interstitials in all extended defects for Si^+ , 30 keV, $1 \times 10^{14} \text{ cm}^{-2}$ annealed at 750 °C.	167
4-7. Concentration of trapped interstitials in only {311} defects for Si^+ , 30 keV, $1 \times 10^{14} \text{ cm}^{-2}$ annealed at 750 °C.	168
4-8. Average size of {311} defects in SOI and bulk for Si^+ , 30 keV, $1 \times 10^{14} \text{ cm}^{-2}$ annealed at 750 °C.	169
4-9. Weak beam dark field images of SOI and bulk silicon for Si^+ , 48.5 keV, $1 \times 10^{14} \text{ cm}^{-2}$ implants after annealing at 750 °C for 5 and 30 minutes.	170
4-10. Concentration of trapped interstitials in all extended defects for Si^+ , 48.5 keV, $1 \times 10^{14} \text{ cm}^{-2}$ annealed at 750 °C.	171
4-11. Concentration of trapped interstitials in only {311} defects for Si^+ , 48.5 keV, $1 \times 10^{14} \text{ cm}^{-2}$ annealed at 750 °C.	172
4-12. Average size of {311} defects in SOI and bulk for Si^+ , 48.5 keV, $1 \times 10^{14} \text{ cm}^{-2}$ annealed at 750 °C.	173
4-13. “+1” value as a function of surface Si thickness for different implant energies used in the study.	174
4-14. Weak beam dark field micrographs of 750 Å SIMOX and bulk silicon for Si^+ , 30 keV, $1 \times 10^{14} \text{ cm}^{-2}$ implants after annealing at 700 °C for 40 and 122 minutes.	178
4-15. Concentration of trapped interstitials in {311} defects for Si^+ , 15 keV, $1 \times 10^{14} \text{ cm}^{-2}$ annealed at (a) 700 °C, (b) 750 °C, and (c) 825 °C. (Note: $S_{\text{H}} = 6 \times 10^9 \text{ cm}^{-2}$ is TEM detection limit).....	179
4-16. Concentration of trapped interstitials in {311} defects for Si^+ , 30 keV, $1 \times 10^{14} \text{ cm}^{-2}$ annealed at (a) 700 °C, (b) 750 °C, and (c) 825 °C.	180
4-17. Concentration of trapped interstitials in {311} defects for Si^+ , 48.5 keV, $1 \times 10^{14} \text{ cm}^{-2}$ annealed at (a) 700 °C, (b) 750 °C, and (c) 825 °C.	181

4-18. Plot of time constant as function of $1/kT$ for (a) 15 keV, (b) 30 keV, and (c) 48.5 keV.....	182
4-19. Ion profiles from UT-Marlowe for (a) 300 Å, (b) 700 Å, (c) 1600 Å, and (d) bulk Si after Si^+ implantation from 5 – 40 keV $2 \times 10^{14} \text{ cm}^{-2}$	184
4-20. Percentage of dose retained in surface Si layer of SOI for Si^+ implants from 5 keV to 40 keV, $2 \times 10^{14} \text{ cm}^{-2}$	185
4-21. Plan-view TEM micrographs illustrating defect evolution in 300 Å SOI and bulk Si for 5 keV, $2 \times 10^{14} \text{ cm}^{-2}$ after annealing at 750° C.	186
4-22. Concentration of trapped interstitials (Si_i) in extended defects for 5 keV, $2 \times 10^{14} \text{ cm}^{-2}$ after annealing at 750° C.....	187
4-23. Plan-view TEM micrographs illustrating defect evolution in 300 Å SOI and bulk Si for 10 keV, $2 \times 10^{14} \text{ cm}^{-2}$ after annealing at 750° C.	188
4-24. Concentration of trapped interstitials in extended defects for 10 keV, $2 \times 10^{14} \text{ cm}^{-2}$ after annealing at 750° C.....	189
4-25. Plan-view TEM micrographs illustrating defect evolution in 700 Å SOI and bulk Si for 20 keV, $2 \times 10^{14} \text{ cm}^{-2}$ after annealing at 750° C.	190
4-26. Concentration of trapped interstitials in extended defects for 20 keV, $2 \times 10^{14} \text{ cm}^{-2}$ after annealing at 750° C.....	191
4-27. Plan-view TEM micrographs illustrating defect evolution in 700 Å SOI and bulk Si for 40 keV, $2 \times 10^{14} \text{ cm}^{-2}$ after annealing at 750° C.	192
4-28. Concentration of trapped interstitials in extended defects for 40 keV, $2 \times 10^{14} \text{ cm}^{-2}$ after annealing at 750° C.....	193
4-29. UT-Marlowe RBS profile showing percent amorphization versus depth. Amorphous layer is approximately 15 nm thick.....	194
4-30. PTEM micrographs of EOR loops in SOI/TEC and bulk Si after annealing at 835 °C in nitrogen. Implant was Si^+ , 5 keV, $1 \times 10^{15} \text{ cm}^{-2}$	195
4-31. QTEM data for EOR loops annealed at 835°C including (a) concentration of trapped interstitials, (b) defect density, and (c) defect size.	196
4-32. PTEM micrographs of oxidation stacking faults (OSFs) that appeared to nucleate off EOR loops upon further annealing at 835 °C. Note significant difference in aspect ratio between 300 Å SOI and the other materials. Implant was Si^+ , 5 keV, $1 \times 10^{15} \text{ cm}^{-2}$	197

4-33. QTEM data for OSFs at 835°C including (a) concentration of trapped interstitials, (b) defect density, (c) major axis length, and (d) aspect ratio.	198
4-34. Concentration of trapped interstitials for both loops and OSFs at 835°C. Note increase in concentration as OSFs begin to nucleate off EOR loops.....	199
4-35. QTEM data for EOR loops annealed at 900°C including (a) concentration of trapped interstitials, (b) defect density, and (c) defect size.	200
4-36. QTEM data for OSFs at 900°C including (a) concentration of trapped interstitials, (b) defect density, (c) major axis length, and (d) aspect ratio.	201
4-37. QTEM data for OSFs at 1000°C including (a) concentration of trapped interstitials, (b) defect density, (c) major axis length, and (d) aspect ratio.	202
5-1. Trapped interstitial dose in SOI and bulk Si for Si^+ , 15 keV, $1 \times 10^{14} \text{ cm}^{-2}$ annealed at 750 °C. Data points are from QTEM data, lines are FLOOPS simulations. Note reduction in Si_i in 750 Å SOI as annealing proceeds.....	206
5-2. Defect density for Si^+ , 15 keV, $1 \times 10^{14} \text{ cm}^{-2}$ annealed at 750 °C. Defects dissolve faster in 750 Å SOI as anneal time proceeds. Model predicts large decrease in initial defect density in 750 Å SOI.	207
5-3. Trapped interstitial dose in SOI and bulk Si for Si^+ , 30 keV, $1 \times 10^{14} \text{ cm}^{-2}$ annealed at 750 °C. Note reduction in Si_i in 750 Å and 1450 Å SOI as annealing proceeds. Model predicts no {311} formation in 750 Å SOI.	208
5-4. Defect density for Si^+ , 30 keV, $1 \times 10^{14} \text{ cm}^{-2}$ annealed at 750 °C. A significant enhancement in defect decay rate occurs in 750 Å SOI. Model predicts no defects form in 750 Å SOI.	209
5-5. FLOOPS simulation of defect size for 1450 Å and bulk Si implanted at Si^+ , 30 keV, $1 \times 10^{14} \text{ cm}^{-2}$. Model overestimates differences in defects size between SOI and bulk Si.	210
6-1. PTEM WBDF micrographs of defect evolution in SOI and bulk for B^+ , 6.5 keV, $3 \times 10^{14} \text{ cm}^{-2}$	240
6-2. Trapped interstitial concentration (Si_i) as a function of annealing time for B^+ , 6.5 keV, $3 \times 10^{14} \text{ cm}^{-2}$ specimens.	241
6-3. PTEM WBDF micrographs of defect evolution in SOI and bulk for B^+ , 19 keV, $3 \times 10^{14} \text{ cm}^{-2}$	242

6-4. Concentration of trapped interstitials as a function of time for B ⁺ , 19 keV, 3x10 ¹⁴ cm ⁻² specimens	243
6-5. UT-Marlowe ion profile simulations for B ⁺ implants at 1 keV, 3.5 keV, 6.5 keV, 3x10 ¹⁴ cm ⁻² . Note location of surface Si/BOX interface for 300 Å, 700 Å and 1600 Å SOI.	244
6-6. Percent retained dose of boron in surface Si layer as function of implant energy for 300 Å, 700 Å and 1600 Å SOI. Calculated using UT-Marlowe ion profiles.	245
6-7. Isothermal Hall data for B ⁺ , 1 keV, 3x10 ¹⁴ cm ⁻² at 750 °C including (a) active dose, (b) hole mobility, and (c) sheet resistance. Note that the active dose contribution from the background (~5x10 ¹³ cm ⁻² to 6x10 ¹³ cm ⁻²) must also be subtracted from the bulk Si numbers.	246
6-8. Isothermal Hall data for B ⁺ , 6.5 keV, 3x10 ¹⁴ cm ⁻² at 750 °C including (a) active dose, (b) hole mobility, and (c) sheet resistance. Note that the active dose contribution from the background (~5x10 ¹³ cm ⁻² to 6x10 ¹³ cm ⁻²) must also be subtracted from the bulk Si numbers.	247
6-9. Comparison of sheet resistance data measured by four point probe and Hall Effect for (a) 1 keV, (b) 3.5 keV, and (c) 6.5 keV, 3x10 ¹⁴ cm ⁻² annealed at 750 °C. Solid symbols and lines represent four point probe measurements and open symbols represent Hall measurements.	248
6-10. Isochronal Hall data for B ⁺ , 1 keV, 3x10 ¹⁴ cm ⁻² after annealing 30 minutes showing (a) active dose, (b) hole mobility, and (c) sheet resistance. Note that the active dose contribution from the background (~5x10 ¹³ cm ⁻² to 6x10 ¹³ cm ⁻²) must also be subtracted from the bulk Si numbers.	249
6-11. Isochronal Hall data for B ⁺ , 6.5 keV, 3x10 ¹⁴ cm ⁻² after annealing 30 minutes showing (a) active dose, (b) hole mobility, and (c) sheet resistance. Note that the active dose contribution from the background (~5x10 ¹³ cm ⁻² to 6x10 ¹³ cm ⁻²) must also be subtracted from the bulk Si numbers.	250
6-12. Boron concentration profiles from SIMS for 300 Å SOI implanted at 6.5 keV, 3x10 ¹⁴ cm ⁻² then annealed at 750 °C. Note segregation of boron into buried oxide.	251
6-13. Clustered dose in SOI and bulk Si for B ⁺ , 6.5 keV, 3x10 ¹⁴ cm ⁻² annealed at 750 °C. Dose was obtained by integrating the B concentration profiles that lie above a level of 1x10 ¹⁹ cm ⁻³	252
6-14. Active fraction of boron in SOI and bulk for 6.5 keV 3x10 ¹⁴ cm ⁻² annealed for 30 minutes.	253

- 6-15. Carbon and oxygen SIMS profiles for 1600 Å SOI and bulk Si implanted with B^+ , $6.5 \text{ keV } 3 \times 10^{14} \text{ cm}^{-2}$, and annealed at 600°C for 30 minutes.254
- 6-16. (a) Boron ion profiles from UT-Marlowe for 15 keV, $3 \times 10^{14} \text{ cm}^{-2}$ and $1 \times 10^{15} \text{ cm}^{-2}$. Vertical lines indicate the location of the surface Si/BOX interface. (b) Percent retained dose for 750 Å, 1450 Å, and bulk Si.255
- 6-17. (a) Sheet number versus time for 15 keV, $3 \times 10^{14} \text{ cm}^{-2}$ annealed at 825°C . Open symbols indicate RTA and closed circles indicate furnace anneals (FA). (b) Fractional active dose for 750 Å, 1450 Å, and bulk Si under same anneal conditions. Note that the active dose contribution from the background ($\sim 5 \times 10^{13} \text{ cm}^{-2}$ to $6 \times 10^{13} \text{ cm}^{-2}$) must also be subtracted from the bulk Si numbers.256
- 6-18. (a) Hole mobility versus time for 15 keV, $3 \times 10^{14} \text{ cm}^{-2}$ annealed at 825°C . Open symbols indicate RTA and closed circles indicate furnace anneals (FA). (b) Sheet resistance for 750 Å, 1450 Å, and bulk Si under same anneal conditions. Note that the active dose contribution from the background ($\sim 5 \times 10^{13} \text{ cm}^{-2}$ to $6 \times 10^{13} \text{ cm}^{-2}$) must also be subtracted from the bulk Si numbers.257
- 6-19. (a) Sheet number versus time for 15 keV, $1 \times 10^{15} \text{ cm}^{-2}$ annealed at 825°C . Open symbols indicate RTA and closed circles indicate furnace anneals (FA). (b) Fractional active dose for 750 Å, 1450 Å, and bulk Si under same anneal conditions. Note that the active dose contribution from the background ($\sim 5 \times 10^{13} \text{ cm}^{-2}$ to $6 \times 10^{13} \text{ cm}^{-2}$) must also be subtracted from the bulk Si numbers.258
- 6-20. Sheet number versus time for 15 keV, $3 \times 10^{14} \text{ cm}^{-2}$ annealed at 750°C for 30 seconds. Note insignificant difference in activation between SIMOX and SOITEC materials.259
- 6-21. Schematic of (a) lattice/surface miscut and (b) bonding misorientation present in SOITEC materials. White lines in (b) show planes corresponding to wafer B, while black lines correspond to wafer A.260
- 6-22. Erroneous (004) ω -2 θ rocking curves for 1600 Å SOITEC wafers implanted with B^+ , 3.5 keV, $3 \times 10^{14} \text{ cm}^{-2}$. Anneals were performed for 30 minutes at 750°C . Samples were aligned to substrate, rather than surface Si layer.261
- 6-23. (004) ω rocking curves for 1600 Å SOITEC wafers as-implanted with B^+ , 3.5 keV, $3 \times 10^{14} \text{ cm}^{-2}$. Misalignment between the surface Si Bragg peak and substrate peak is shown.262
- 6-24. (004) ω -2 θ rocking curves for unimplanted 1600 Å SOITEC wafers, illustrating presence of Pendellosung fringes. Samples were aligned to surface Si layer.263

6-25. (004) ω -2 θ rocking curves for unimplanted, as-implanted, and annealed 1600 Å SOI implanted with B ⁺ , 3.5 keV, 3×10^{14} cm ⁻² . Anneal was 900°C for 30 minutes. ...	264
6-26. (004) ω -2 θ rocking curves for unimplanted and as-implanted bulk Si implanted with B ⁺ , 3.5 keV, 3×10^{14} cm ⁻²	265
6-27. (004) ω -2 θ rocking curves for bulk Si implanted with B ⁺ , 3.5 keV, 3×10^{14} cm ⁻² . Anneals were performed at 600°C, 750°C, 900°C, and 1000°C for 30 minutes.	266
6-28. Comparison of (004) ω -2 θ rocking curves for 1600 Å SOI and bulk Si as-implanted with B ⁺ , 3.5 keV, 3×10^{14} cm ⁻²	267
6-29. Comparison of (004) ω -2 θ rocking curves for 1600 Å SOI and bulk Si implanted with B ⁺ , 3.5 keV, 3×10^{14} cm ⁻² . Anneals were performed at 900°C for 30 minutes. Oscillatory pattern belongs to SOI, while the high intensity peak is bulk Si.	268
6-30. SIMS profiles of SOITEC and bulk Si materials implanted with B ⁺ , 1 keV, 3×10^{14} cm ⁻² . Anneals were 750°C for 30 minutes. Note depletion of B on surface Si side of interface, as well as pileup on BOX side.	269
6-31. SIMS profiles of SOITEC and bulk Si materials implanted with B ⁺ , 6.5 keV, 3×10^{14} cm ⁻² . Anneals were 750°C for 30 minutes.	270
6-32. QTEM data for B ⁺ , 3.5 keV, 3×10^{14} cm ⁻² annealed at 750°C for various times. Note little difference in dissolution between SOI and bulk Si.	271
6-33. Comparison of TED behavior in 1600 Å SOI and bulk Si after implantation at B ⁺ , 6.5 keV, 3×10^{14} cm ⁻² . Anneals were performed at 750°C for 120 minutes. Note slight tail enhancement in 1600 Å SOI compared to bulk Si.	272
6-34. SIMS profiles of SOITEC and bulk Si materials implanted with B ⁺ , 19 keV, 3×10^{14} cm ⁻² . Anneals were 750°C for 30 minutes.	273
6-35. SIMS profiles of SOITEC and bulk Si materials implanted with B ⁺ , 1 keV, 3×10^{14} cm ⁻² . Anneals were 1050°C for 30 minutes. Note box-shape profile after annealing SOI materials.	274
6-36. SIMS profiles of SOITEC and bulk Si materials implanted with B ⁺ , 6.5 keV, 3×10^{14} cm ⁻² . Anneals were 1050°C for 30 minutes.	275
6-37. Retained concentration versus surface Si layer thickness for B ⁺ , 1 - 19 keV, 3×10^{14} cm ⁻² . Anneals were performed at 1050°C for 30 minutes. Concentrations were taken as the average concentration across the surface Si layer, while avoiding transient effects near interfaces.	276

6-38. Segregation coefficients versus surface Si thickness after annealing at 1050°C for various times. Implants were B ⁺ , 1 keV, 6.5 keV, and 19 keV, with a dose of 3x10 ¹⁴ cm ⁻² .	277
7-1. Schematic of LEAP constituents near a surface containing microtips for analysis. From [KEL00].	283
7-2. Schematic of MOS capacitor structure that could be used to alter surface potential at Si/SiO ₂ interface.	284

Abstract of Dissertation Presented to the Graduate School
of the University of Florida in Partial Fulfillment of the
Requirements for the Degree of Doctor of Philosophy

INTERFACIAL PHENOMENA IN ION IMPLANTED SILICON-ON-INSULATOR
MATERIALS

By

Antonio Fernando Saavedra

August 2004

Chair: Kevin S. Jones

Major Department: Materials Science and Engineering

Silicon-on-insulator (SOI) allows for many short channel effects to be overcome, leading to faster operating speeds and lower power dissipation in metal-oxide-semiconductor (MOS) devices. Integration of SOI requires an understanding of interstitial mediated processes, such as extended defect evolution and dopant activation. It has been shown recently that ion implantation of dopants in SOI results in anomalous diffusion profiles leading to dopant loss to the buried oxide (BOX), and preventing that dopant from providing electrical conduction within the surface silicon film.

The first goal of this study was to investigate the role of the surface silicon/BOX interface on {311} defect, dislocation loop, and oxidation stacking fault (OSF), evolution in partially-depleted (PD) and fully-depleted (FD) SOI. This helps to elucidate the degree to which the interface acts as a sink for excess interstitials produced by ion implantation. Energies ranging from 5 keV to 48.5 keV and doses from $1 \times 10^{14} \text{ cm}^{-2}$ to $1 \times 10^{15} \text{ cm}^{-2}$ were used to understand the effect of the interface on non-amorphizing and

amorphizing Si⁺ implants. Nucleation of {311}s and loops was shown to be strongly dependent on the implant energy and surface silicon thickness. The FLOOPS process simulator was used to simulate the {311} defect evolution in SOI. The model overestimates the effect of the surface Si/BOX interface on interstitial recombination indicating that it is not as strong a sink for interstitials as previously thought.

Investigation of boron interstitial clustering (BICs) in SOI comprised the second part of the study. Boron implants ranging from 1 keV to 19 keV, $3 \times 10^{14} \text{ cm}^{-2}$ were used to provide varying amounts of dose loss to the BOX. Hall effect data determined the time and temperature dependence of boron activation in SOI. SIMS, TEM, and HRXRD were used investigate the roles of strain and dopant segregation on boron activation. At temperatures less than 750 °C, the active dose of boron in SOI was slightly less than bulk Si. However, above 750 °C the activation in SOI began to approach bulk Si. Truncation of the boron implant profile by the interface was found to reduce BIC formation within the surface Si layer.

CHAPTER I MOTIVATION

A number of alternative materials are being considered to replace the traditional bulk silicon substrate. One of the most promising candidates is silicon-on-insulator (SOI). This chapter focuses on the roadblocks to continued scaling of planar bulk complementary metal-oxide-semiconductor (CMOS) devices, as well as the advantages of moving to SOI. Lastly, the goals for the current investigation are stated.

1.1 Scaling of Planar CMOS

The continued drive for computers that will perform greater numbers of operations per second requires the shrinking of the components of the metal-oxide-semiconductor field effect transistor (Figure I-1). Moore's Law provides guidance so that the demand for computational power can be supplied based on the economy. Scaling requires higher doping levels, shallower junctions and narrower gate lengths. Unfortunately, these requirements lead to a number of parasitic effects, such as latchup, short channel effects, junction capacitance, and power dissipation.

1.1.1 The Silicon Age and Moore's Law

Different stages of development within a society are often classified according to advances in materials science. Examples of these include the Stone Age, Bronze Age and Iron Age. Since the invention of the transistor in 1948 [BAR01] and the integrated circuit in 1959 [KIL01], the Silicon Age has transformed our world in ways that could not have been imagined 50 years ago.

In 1965, Gordon Moore put into context the trend (Figure 1-2) that has been the driving force of the semiconductor industry [MOO65]. Although Moore's prediction that the number of transistors on a chip would double every year overestimated the actual industry performance, it laid a foundation. Moore's Law, as it became known, predicts that the number of transistors on a chip doubles every 18 to 24 months. In essence, it requires continued miniaturization of the devices on an integrated circuit chip.

1.1.2 Short Channel Effects

The reduction in dimensions of the MOSFET leads to undesirable device characteristics, known as short channel effects. This is primarily a result of a decrease in the threshold voltage as the channel length is reduced [TAU98]. Some of these effects include charge sharing, drain-induced barrier lowering (DIBL), punchthrough, hot electron effects, and increased leakage current. In general, as the junction depth, x_j , and gate length, L , are reduced the short channel effects (SCE) become more pronounced. This is one reason significant research is now being conducted in ultra shallow junction formation technologies [JON98].

In order to curb SCE and tailor threshold voltage, a number of different ion implantation steps are necessary as illustrated in Figure 1-1. A threshold voltage adjust channel implant is used to modify threshold voltage for the NMOS and PMOS devices. The source/drain extension implants provide a concentration gradient from the deep/source drain to the conducting channel in order to reduce the maximum electric field. Halo/punchthrough implants prevent the intersection of source and drain depletion regions when the device is turned on, thus preventing alternate paths for current flow [ZIE00].

1.1.3 Other Problems

Latchup occurs when a parasitic NPNP thyristor is triggered between adjacent NMOS and PMOS devices. This can result in abnormally large currents, as well as taking the supply

voltage straight to the ground potential, causing failure of the devices. Latchup is accounted for by building CMOS devices in a lightly doped epitaxial Si layer deposited on a highly doped substrate. Alternatively, high energy ion implantation can also be used to create deep, highly doped wells below the devices [PLU00].

Another constraint being placed on bulk silicon is the increased power used by chips as the transistors are made smaller [FRA02]. One method for reducing power consumption in a device is to use a lower operating or supply voltage. Portable electronic systems rely heavily on devices that operate under a low supply voltage. It is not without coincidence that alternative materials are now being considered to help simplify processing [COL97], reduce SCE [VEE89], and control power consumption [FRA02].

1.2 Silicon-on-Insulator (SOI) for CMOS

By incorporating a thin layer of silicon on top of an insulating material, e.g., silicon dioxide, many of the problems plaguing the scaling of bulk Si CMOS can be remedied. Altering the thickness of the layers allows for SOI to be tailored towards a variety of device applications. This is illustrated in Figure 1-3. However, there are several challenges to scaling and integration of SOI; these are addressed below.

1.2.1 Advantages over Bulk Silicon

SOI is an ideal candidate for low voltage/low power, as well as radiation hard electronic applications [COL98, PLO00, ADA98]. It allows for increased chip speed, lower operating voltage, reduced parasitic capacitance, elimination of latchup, and reduced susceptibility to interference from outside radiation sources [COL97]. SOI is also able to operate over a wider temperature range making it desirable for high temperature operation.[FLA95] Table I-1 summarizes the advantages and disadvantages of using SOI over bulk silicon for CMOS applications.

Figure 1-4 compares operating characteristics for SOI and bulk silicon CMOS. This shows that the threshold voltage can be tailored depending on the surface Si thickness. Another advantage of SOI is that the presence of the BOX prevents interference from cosmic radiation (a.k.a soft error), making SOI a popular material for use in satellite communication and deep space systems.[HIR99] An SOI substrate may also be used to completely eliminate latchup formation. This is illustrated in Figure 1-5.

Perhaps the most important reason for switching to an SOI substrate is for low voltage/low power operating conditions. Using SOI allows for a 2X-3X reduction in power consumption compared to bulk CMOS. Another advantage of using SOI is a simplification in manufacturing by reduction of processing steps. It eliminates the need for a deep well formation step, which is required in bulk CMOS. Also, use of FD SOI does away with the need for an anti-punchthrough implant since the depletion region extends the entire thickness of the channel region.[COL97] It is evident that using SOI provides for numerous advantages over bulk silicon for fabrication of future CMOS integrated circuits.

1.2.2 Challenges for SOI

Any fair discussion should also mention the disadvantages and challenges that are posed by SOI. Most of these challenges relate to the kink effect and a number of floating body effects that occur during device operation.[COL97] The kink effect shows up when high potentials are applied to SOI MOSFETs after saturation has been reached. This creates electron hole pairs due to impact ionization within the channel of the device and leads to unreliability in device performance.

SOI MOSFETs also require the fabrication of two gates rather than the singular gate used in bulk MOSFETs. The front gate is used to control the conduction within the channel, while the back gate is typically in a grounded configuration. This helps prevent an inversion

layer from forming at the surface Si/BOX interface. [COL97] However, this adds to the complexity of fabricating an SOI MOSFET.

Perhaps the single greatest challenge to the implementation of SOI is its lack of knowledge base. Bulk Si has been the standard substrate for over three decades and a plethora of information is available. For example, very little is known about how the presence of an additional silicon/silicon dioxide interface affects dopant diffusion and activation. Anomalous diffusion profiles have been observed in SOI materials recently, adding to the complexity of developing models to design advanced devices. [PAR99] It is also not known how the surface Si/BOX interface affects interstitial release from extended defects such as {311} defects and dislocation loops. Understanding this is critical to understanding why dopants diffuse the way they do in SOI.

1.3 Objectives and Statement of Thesis

The goal of this research is to understand the role of the surface Si/BOX interface on interstitial mediated processes in SOI materials. This is done by first determining how self-interstitial populations are affected by the interface. Once this is understood, it can be applied to the problem of dopant diffusion and activation. This thesis provides significant scientific contribution in the following areas:

- Proximity of damage to the surface Si/BOX interface on {311} defect and dislocation loop evolution for non-amorphizing implantation in fully depleted and partially depleted SOI.
- Kinetics of the {311} dissolution reaction for non-amorphizing implants in SOI.
- Effect of proximity of damage to the surface Si/BOX interface on {311} defect and dislocation loop evolution for amorphizing implantation in FDSOI and PDSOI.
- Development of a physically based model for predicting interstitial evolution in FDSOI and PDSOI.
- Investigation of time, temperature, energy, and concentration dependence of boron activation in FDSOI and PDSOI.

- Determination of mechanism for low electrical activation of boron in SOI.

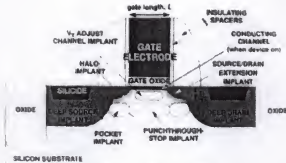


Figure 1-1. Schematic of bulk silicon MOSFET device showing different ion implanted areas within device [JON98].

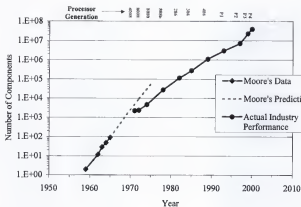


Figure 1-2. Moore's Law describing scaling of the number of transistors on a chip [MOO65].

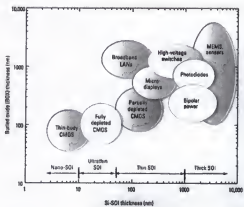


Figure 1-3. Applications for varying surface Si and BOX thickness [SIG03].

Table 1-1. Advantages and disadvantages of SOI devices over bulk silicon [IB103].

	FD SOI	PD SOI	Bulk
Junction capacitance	Small	Small	Large
Body effect	Small	Large	Large
Floating body effect	Small	Large	None
V_{th} control	Difficult	Easy	Easy
Subthreshold Leakage	Small	Larger	Large
S/D silicidation	Difficult	Easy	Easy
Lay-out area	Small	Small	
Circuit design	Easy	Difficult	
Scalability	Difficult	Easy	Difficult
Manufacturability	Difficult	Easy	

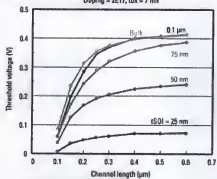
SHORT CHANNEL EFFECT IN THIN SOI* Doping = ZE17, $t_{ox} = 7$ nm

Figure 1-4. Comparison of operating characteristics for SOI and bulk CMOS [IBM03].

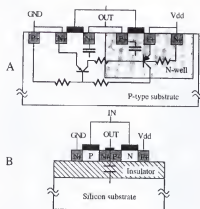


Figure 1-5. Schematic of CMOS cross section illustrating elimination of latchup path in SOI [COL97].

CHAPTER 2 LITERATURE REVIEW

The need for a faster and more efficient CMOS device has led to the insurgence of SOI. This chapter reviews the status of SOI technology to date. Scaling of integrated circuits has relied heavily on the ability of ion beams to create shallow, abrupt as-implanted doping profiles in bulk Si. Unfortunately, post-implant thermal processing must be performed in order for the dopant atoms to occupy substitutional lattice sites and contribute electrically. This can result in unacceptable junction depths and sheet resistance due to dopant interactions with point defects. For this reason, fundamentals of ion implantation, atomistic diffusion, and segregation in the proximity of interfaces are also reviewed in the context of Si microelectronic processing. Emphasis is placed on the Si/SiO₂ interface since it is of most interest in the investigations of later chapters.

2.1 Ion Implantation and Damage Recovery

The discovery that atoms in the gas phase could be ionized by their bombardment with electrons is credited to the German physicist, Eugen Goldstein. [GOL86] The work of Wien [WIE98], Thomson [THO12], Rutherford, and Bohr [BOH13] was also critical to understanding the behavior of ionized particles in electromagnetic fields [MOF95, WIE99]. Ion implantation was first proposed by Shockley as a method for fabricating doped regions within semiconductor devices. [SHO03] Ever since, it has been the preferred technique for introducing dopants into silicon in controlled amounts. It offers a number of advantages over gas and solid source diffusion, shown in Table 2-1. Ion implantation is a very versatile process that has also been

used for introducing gettering layers, synthesis of compounds, and surface modification of metals and polymers. Unfortunately, the main drawback of using ion implantation is resulting damage to the target, consisting mainly of point defects. For silicon, this damage can lead to the deleterious effects of transient enhanced diffusion, dopant-defect clustering, as well as leakage current within the depletion region of transistors.

2.1.1 Ion Stopping and Primary Defects

The process of ion implantation is a highly non-equilibrium one. Physical, chemical and structural changes may occur when the ions become embedded in the target material. A number of elastic and inelastic effects also result, leaving the silicon in a damaged, metastable state. Lattice atoms may be displaced from their equilibrium positions when the displacement energy (15 eV for Si) is exceeded. As an energetic ion comes to rest, it may undergo a number of collisions with atoms in the Si lattice, which leads to the production of a damage or collision cascade. This damage cascade, illustrated in Fig. 2-1, consists of interstitials, vacancies, amorphous regions, ionized atoms, etc. These defects produced in the "as-implanted" state are typically referred to as primary defects [ZIE00].

The density of a damage cascade depends significantly on the ion mass and stopping or energy-loss mechanism. The two primary stopping mechanisms are nuclear and electronic stopping. Nuclear stopping is characterized by a significant transfer of energy between the nuclei of the energetic ion and the nuclei of a lattice atom. This results in a very dense damage cascade. An ion that undergoes electronic stopping is decelerated by interacting with the electron cloud surrounding a lattice atom. Thus, the energy losses in electronic stopping are much less per stopping event and the collision cascade is less dense. In general, nuclear

stopping is observed at lower implant energies and heavier ions (e.g., As, Sb), while electronic stopping occurs at higher energies and for low mass ions (e.g., B, H).

Damage cascades are also affected by the ability of the ion to channel, which is related to the ion mass, as well as the crystal orientation relative to the incident ion beam. Channeling refers to the phenomenon whereby an ion is able to traverse great distances into the crystal by moving through the interstices present in the lattice. For this reason, {100} Si wafers are typically oriented relative to the beam direction with a tilt of 7° in the [110] direction followed by a rotation of 22° around the [100] direction. This aids in reducing channeling and improving the reproducibility of implant profiles. Thin screen oxides and pre-amorphization are also common procedures for controlling channeling. [ZIE00]

2.1.2 Secondary Defects and Their Structure

A large increase in the excess interstitial population occurs after ion implantation. Secondary defects are those that form during subsequent thermal processing and are nearly exclusively extrinsic, or interstitial, in nature. Post-implant annealing is always required since the majority of implanted dopant ions are not on substitutional lattice sites. These implanted dopants do not contribute electrically and are considered inactive. Upon annealing, the damaged silicon lattice tends toward a more equilibrium state. Excess interstitials undergo a number of evolutionary processes, shown in Fig. 2-2, in order to reduce the free energy associated with the silicon lattice. These processes may be broadly classified into recombination and clustering. Recombination occurs when the strain field surrounding an interstitial interacts with that of a vacancy resulting in a mutual attraction and annihilation. Frenkel pairs, a interstitial and vacancy pair around a host lattice site, may recombine during implantation or annealing at temperatures $<600^\circ\text{C}$. Clustering of excess interstitials often

results in the formation of submicroscopic interstitial clusters (SMICs), $\{311\}$ defects, and dislocation loops in order to reduce the Gibbs free energy of the system. While the final annealed state may not be an entirely equilibrium one, it is desired that the final state does not significantly change with time at the temperature required for device operation.

The location of the majority of excess interstitials depends on whether the implanted dose is sufficient to produce enough disorder in the silicon lattice ($\sim 10\%$) to create an amorphous layer. This dictates where the secondary defects form relative to the surface. For non-amorphizing implants the majority of excess interstitials lie around the projected range of the implant. In the case of amorphization, the excess interstitials are found just beyond the amorphous-crystalline interface after regrowth of the amorphous layer has commenced. Based on dislocation loop analysis of non-amorphizing implants, the number of excess interstitials was found to be approximately equal to the implanted dose [JON88]. This was later termed the "plus one" model [GIL91]. However, it has been shown that the "plus one" model varies depending on the ion mass [HER98, PEL98].

Secondary defects are particularly important because they are believed to drive the phenomenon of transient enhanced diffusion (TED). They do this by maintaining an interstitial supersaturation until their eventual dissolution. [EAG94] Extended defects, such as $\{311\}$ s and loops, may also act as sources of leakage current in devices [LAN86]. This occurs because the strain field of the dislocation behaves as a mid-band gap recombination center. Jones et al., provided a classification scheme for extended defects produced upon thermal annealing of silicon [JON88]. $\{311\}$ defects and dislocation loops are observed for non-amorphizing implants (Type I) as well as continuous amorphous layers (Type II). Hairpin defects (Type III) result from imperfect regrowth of a continuous amorphous layer. Clamshell defects (Type IV),

also associated with solid phase epitaxial regrowth, occur whenever a buried amorphous layer is formed. These defects form at the intersection of the two amorphous-crystalline interfaces upon regrowth. Precipitation related defects (Type V) are observed when an impurity is implanted to very high concentrations above the solid solubility of the impurity in the matrix. $\{311\}$ defects and dislocation loops are discussed in detail below, since they are the two extended defects of most interest in the present study.

2.1.2.1 Submicroscopic interstitial clusters (SMICs)

As their name suggests, submicroscopic interstitial clusters (SMICs) are secondary defects that cannot be resolved optically using current microscopy techniques. SMICs, after the interstitial point defect, are believed to be the basis from which the microscopic extended defects evolve, although a structural transformation appears necessary [COF99]. Unfortunately, very little is known about how SMICs evolve, as well as their influence on TED. It has been shown that TED can occur in the absence of extended defects, providing a basis for the existence of SMICs [ZHA95]. Due to their small size, detection is commonly done using deep level transient spectroscopy (DLTS) [BEN97, BEN98], photoluminescence (PL) [COF99, LIB01], and electron paramagnetic resonance (EPR). *Ab initio* calculations also provide insight into the energetically favorable SMIC configurations and their evolutionary pathways.

Benton et al., [BEN97] implanted p-type Czochralski (CZ) and epitaxially grown substrates with Si^+ at energies of 145 keV – 2 MeV and doses of $1 \times 10^{10} \text{ cm}^{-2}$ – $5 \times 10^{13} \text{ cm}^{-2}$. DLTS was used to monitor the low temperature (100 – 680 °C) evolution of point defects into SMICs and $\{311\}$ defects. At doses less than $1 \times 10^{10} \text{ cm}^{-2}$ nearly all Frenkel pairs recombined and SMICs were not observed to form. For higher doses (1×10^{12} – $7 \times 10^{13} \text{ cm}^{-2}$) annealed at temperatures above 600 °C, two self-interstitial type defects were observed at $E_v + 0.29 \text{ eV}$ and

$E_v+0.48$ eV in the absence of $\{311\}$ defects. Annealing of the $5 \times 10^{13} \text{ cm}^{-2}$ above 680°C resulted in the formation of $\{311\}$ s and a DLTS signal at $E_v+0.50$ eV. The subsequent decrease in the two DLTS signals at $E_v+0.29$ eV and $E_v+0.48$ eV led the authors to conclude that the SMICs are either the precursors of the $\{311\}$ or they compete as sinks for the self-interstitials. In a similar experiment for n-type material, Benton et al., [BEN98] identified 5 DLTS signals associated with the interstitial type defects: $E_c-0.14$ eV, $E_c-0.29$ eV, $E_c-0.37$ eV, $E_c-0.50$ eV, and $E_c-0.58$ eV. They indicate that the defects at $E_v+0.29$ eV and $E_v+0.48$ eV are related to those at $E_c-0.29$ eV and $E_c-0.50$ eV since they show similar annealing characteristics. The defect at $E_c-0.58$ eV appeared only in the presence of a higher oxygen concentration. They conclude that the thermal stability of interstitial clusters was enhanced due to an increase in the interstitial concentration as the dose increased.

The appearance of a sharp peak in the PL spectrum at 1376 nm was observed by Coffa et al., to indicate a structural transformation from SMICs to $\{311\}$ s [COF99]. However, they were unable to identify the size or configuration of the SMICs present in their specimens. This problem has led to a number of studies using *ab initio* total-energy calculations [PAY92] and inverse modeling techniques.

Kim et al., used tight-binding and *ab initio* local density approximation simulations to determine the formation energy, E_f , of interstitial clusters ranging from the di-interstitial ($n=2$) to the $\{311\}$ ($n=\infty$), where n denotes the number of interstitials in the cluster [KIM00]. Figure 2-3 shows the formation energy as a function of the number of interstitials. E_f can be seen to decrease as the cluster size increases until it approaches the most stable configuration of the $\{311\}$. On the other hand, Arai et al., found the most stable configuration to occur when $n=4$ [ARA97, KOH99]. This was further supported by Cowern et al., which found local minima in

the formation energy at $n=4$ and $n=8$ (Fig. 2-4) [COW99a]. This has since been used to model a number of boron TED experiments by coupling of a SMIC model with a diffusion model [COW99a, LAM03].

2.1.2.2 {311} defects

The most studied of all the extended defects in Si is the {311} (a.k.a. {113}) defect, due to its direct link to TED [EAG94]. Since then, considerable effort has been undertaken to better understand their characteristics. Hundreds of experiments have been conducted to determine their affect on the diffusion of every technologically important dopant in Si. These experiments are made easier since the {311} is microscopic and can be easily monitored by use of the TEM. This allows the defect microstructure to be correlated with dopant diffusion, commonly measured using secondary ion mass spectrometry (SIMS) or Rutherford backscatter spectrometry (RBS). It should be mentioned that {311} defects are not a requirement in order for TED to be observed, both SMICs and dislocation loops also drive TED.

Figure 2-5 shows a 3D representation of a {311} defect within the Si lattice. Two types of {311} defects may be observed depending on whether or not they are elongated/rod-like or planar. Both defects lie on the {311} habit plane and extend in $\langle 110 \rangle$ directions. A burger's vector of $\mathbf{b} = a/25 \langle 116 \rangle$ has been measured using high resolution TEM (HRTEM) by Takeda et al., [TAK94] Planar {311} defects are less studied, and may be produced using irradiation with high energy electrons [TAK95]. They have a stacking periodicity of $a/4 \langle 110 \rangle$ and consist of structural units of 5-, 6-, 7- (I units), and 8- (O units), membered rings, as shown in Fig. 2-6. The interstitial atoms are found within the 6-membered ring. Note also that no dangling bonds are left in the {110} cross section. However, since the I and O units are not necessarily periodic the interstitial density around planar {311}s varies by 5 nm^{-2} [TAK92]. It should be mentioned

that the planar defects are not true stacking faults although a small fringe contrast may be observed in the HRTEM [CLA03].

For ion-implanted Si, the rod-like {311} defect is commonly observed, shown in Fig. 2-7. Their elongation results due to the fact that self-interstitials can be added along the {110} cross section without introducing dangling bonds. For this reason, these defects do not significantly change in width ~ 4 nm [EAG94]. Using the structure of Takeda [TAK94], which found an areal density of interstitials of $5.1 - 5.5 \text{ nm}^{-2}$ along the {113} cross section, the total interstitials within a rod-like {311} can be estimated to be approximately 26 nm^{-1} . This estimate commonly serves as a basis for quantitative TEM studies to determine interstitial populations within extended defects.

It should be mentioned that below a threshold dose, {311} defects do not form and only SMICs might be present. This threshold is debatable, but appears to be between 7×10^{12} [ZIE00] and $1 \times 10^{13} \text{ cm}^{-2}$ [LIB01] Si^+ doses. These doses are easily reached in modern IC fabrication, so {311} defects will nearly always form. However, the misconception that {311} defects are the sole source of interstitials should be avoided.

{311} defects can be made to dissolve upon annealing above 700°C . Release of interstitials from {311} defects has been shown to follow an exponential relationship according to

$$Si_i = Si(0)e^{-t/\tau} \quad (2.1)$$

where Si_i is the planar density of interstitials trapped in {311}s, $Si(0)$ is the pre-exponential, t is the anneal time, and τ is the time constant for dissolution. This time constant obeys first order reaction kinetics to yield an activation energy for dissolution via the Arrhenius relationship

$$\tau = \tau(0)e^{-E_a/RT} \quad (2.2)$$

where $\tau(0)$ is the pre-exponential, E_a the activation energy for $\{311\}$ dissolution, k Boltzmann's constant, and T the temperature in Kelvin. The value of E_a for $\{311\}$ defects has been determined to be approximately 3.7 eV [SOL91].

$\{311\}$ defects do not necessarily have to dissolve, though. Li and Jones have qualitatively shown that $\{311\}$ defects are the source of dislocation loops for non-amorphizing implants. They showed, via in-situ HRTEM, that $\{311\}$ defects can either dissolve or undergo an unfaulting reaction to form dislocation loops [LIJ98]. These defects are the subject of the next section.

2.1.2.3 Dislocation loops

Somewhat less studied in comparison to the $\{311\}$ defect is the dislocation loop, although it can also drive TED long after $\{311\}$ defects have dissolved [ZIE00, NOD00]. Dislocation loops can be stable at moderately high temperatures (750°C – 850°C) for hours. Another drawback of these defects is their ability to provide leakage current paths and degrade carrier lifetimes when lying across a junction. This is due to the introduction of localized energy levels that sit near the middle of the band gap in Si [MIY97, BUL78]. On the other hand, a great advantage can be gained by using dislocation loops to getter out metallic impurities. By introducing a dislocation loop band well below the device junctions, any metallic impurities lying in the active regions will be attracted to the strain field introduced by the loop band [CHA97].

These defects always form under amorphizing implant conditions, assuming the implant energy is not ultra low energy, as well as non-amorphizing conditions when the dose is marginally high. Figure 2-8 shows the conditions under which extended defects, particularly loops, are expected to form for varying doses and ion mass [JON88]. Faulted Frank loops and

perfect elongated loops are the two common dislocation loops observed in ion implanted Si. They are both two-dimensional precipitates placed in between adjacent $\{111\}$ planes of Si, but have different burger's vectors. The faulted loops have a $\mathbf{b} = a/3 \langle 111 \rangle$, while the perfect loops have a $\mathbf{b} = a/2 \langle 110 \rangle$. The planar density of interstitials is believed to be approximately the same, $1.566 \times 10^{15} \text{ cm}^{-2}$. Loops that form as a result of amorphizing implants are termed end-of-range (EOR), but bear no relation to the faulted or perfect loop; both types are observed as EOR loops [CLA03].

As mentioned, compared to $\{311\}$ defects, dislocation loops are much more thermally stable. They exhibit an activation energy for dissolution in range of 5 eV. Another key difference is their ability to Ostwald ripen, allowing a larger dislocation loop to absorb the interstitials from a smaller one [JA102]. Thus, the larger dislocation loops are more stable. Still an issue of debate is whether or not $\{311\}$ defects truly Ostwald ripen. Moller et al., found the average size of $\{311\}$ defects to increase as annealing proceeded [MOL98]. Others have noted that $\{311\}$ s should acquire an equilibrium shape at long times, but the aspect ratio should be constant during ripening [EAG00, COW00]. However, Law and Jones [LAW00] have used the experimental results of Li [LIJ98] to develop a model for $\{311\}$ evolution that does not depend on Ostwald ripening. They note that dissolution of $\{311\}$ s depends on the ability of interstitials to hop off the ends of the defects, thus smaller $\{311\}$ s dissolve faster than larger ones, but not necessarily because they are more stable. Similarly, interstitials can only be added to the $\{311\}$ by attaching to the ends of the defect, whereas in dislocation loops the interstitials may attach anywhere along the edge.

2.1.3 Models for Defect Evolution

A number of models for predicting the evolution of $\{311\}$ defects and dislocation loops have been developed, but only after their link to TED. Only recently has coupling between $\{311\}$ models and loop models been achieved. Clearly, the ultimate goal is to provide a universal model that accurately predicts all the evolutionary stages of clustering starting with the self-interstitial and ending with its dissociation from a secondary defect.

The first $\{311\}$ model to be developed was based on first order kinetics, but was only applied to the results of one experiment [RAF96]. In it, the interstitial release rate was determined by the hopping frequency and binding energy to the cluster, while the cluster growth was depended on the ability of the cluster to trap diffusing interstitials. Unfortunately, this model did not consider defect size or the dependence of the interstitial binding energy on cluster size. This was the basis of the first model of Law and Jones [LAW96], as well as others [HOB97, GEN97], which used a two-moment method to predict the $\{311\}$ clustering and dissolution process. However, the models of Hobler et al., [HOB97] and Gencer and Dunham [GEN97] used parameters that allowed for an energy dependence of the defect based on their size.

This was the motivation for the second model of Law and Jones [LAW00] since a line defect should not exhibit such dependence. This model incorporated three new ideas. First, that the $\{311\}$ defect size does not affect the binding energy of interstitials to it. Second, the dissolution of the defect is governed by the ability of the interstitials to dissociate from the ends of the defects rather than their diffusion to the surface. Third, nucleation of the defects is heterogeneous in nature, i.e. defects form from damage created by the ion implantation process.

Based on this, the number of interstitials in $\{311\}$ s and SMICs are solved, as well as the defect size as a function of time according to

$$\frac{dC_{311}}{dt} = \frac{D_{311}(C_i - C_{311E_q})}{\tau_{311}} \quad (2.3)$$

$$\frac{dD_{311}}{dt} = \frac{-D_{311}C_{311E_q}}{\tau_{311}} \frac{D_{311}}{C_{311}} \quad (2.4)$$

$$\frac{dC_{SMIC}}{dt} = \frac{C_{SMIC}(C_i - C_{SMICE_q})}{\tau_{SMIC}} \quad (2.5)$$

where C_{311} is the concentration of interstitials trapped in $\{311\}$ defects, D_{311} is the density of $\{311\}$ defects, τ_{311} is the dissolution time constant for $\{311\}$ s, C_i is the total concentration of interstitials, C_{311E_q} is the equilibrium concentration of interstitials in $\{311\}$ s, and t is time.

Notation for parameters with the subscript SMIC apply to the SMIC defects.

The coupled $\{311\}$ and loop model developed by Avci et al., [AVC04] is based partly off the model of Law and Jones [LAW00], with the slight addition of a nucleation rate term. This model is reviewed in detail since it forms the basis of the model developed in the current studies. It assumes the dislocation loop size to be governed by the interaction of the loop boundary with point defects. It calculates the effective equilibrium concentrations of point defects according to that given by Borucki [BOR92]

$$C_{ib} = g_{bc} C_i^* (P) e^{-\Delta E_f / kT} \quad (2.6)$$

$$C_{vb} = g_v^{-1} C_v^* (P) e^{\Delta E_f / kT} \quad (2.7)$$

where C_{ib} is the effective equilibrium concentration of interstitials at loop boundaries, C_{vb} is the effective equilibrium concentration of vacancies, g_{bc} is a geometric factor (~ 0.7), C_i^* is the equilibrium concentration of interstitials, C_v^* is the equilibrium concentration of vacancies, P is pressure, and ΔE_f is the change in the defect formation energy as a result of self-force of a

dislocation loop developed by Gavazza et al. [GAV76]. The interstitial and vacancy continuity equations are then modified as

$$\frac{\partial C_i}{\partial t} = \nabla [D_i C_i^*(P) \nabla (\frac{C_i}{C_i^*(P)})] - K_R (C_i C_v - C_i^*(P) C_v^*(P)) - K_{IL} \int_{0+}^{\infty} (C_i - C_{ib}) f_D(R) dR \quad (2.8)$$

$$\frac{\partial C_v}{\partial t} = \nabla [D_v C_v^*(P) \nabla (\frac{C_v}{C_v^*(P)})] - K_R (C_i C_v - C_i^*(P) C_v^*(P)) - K_{vL} \int_{0+}^{\infty} (C_v - C_{vb}) f_D(R) dR \quad (2.9)$$

where K_R is the bulk recombination rate, D corresponds to the interstitial and vacancy diffusivity, respectively, K_{IL} is the reaction rate constant between interstitials and loops, and K_{vL} is the reaction rate constant between vacancies and loops. This leads to the formulation for the change in dislocation loop density with time according to

$$\frac{dD_{all}}{dt} = N_{rate}^{Dall} - \frac{1}{(C_i/C_{ib} + 10)} \frac{2D_{all}}{R_p^2} K_R \quad (2.10)$$

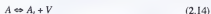
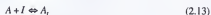
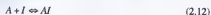
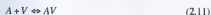
where N_{rate}^{Dall} is the loop nucleation rate, D_{all} is the loop defect density, and R_p is the average loop radius. Avci applied the model to a variety of implant and anneal conditions with reasonable success and details can be found elsewhere. [AVC02]

2.2 Dopant Diffusion in Bulk Silicon

A brief review of dopant diffusion mechanisms is now given due to its importance in the current investigations. More detailed reviews can be found in a number of excellent sources and the reader is referred to those for a comprehensive discussion of the literature [FAH89, HUS94, CHA97, JAI02, SHA03, HAY00]. Topics have been selected as they pertain mainly to boron interactions with point defects and the modeling associated with it.

2.2.1 Mechanisms of Dopant Diffusion

Dopants migrate through the Si lattice by interaction with point defects via 4 main mechanisms, shown in Fig. 2-9. These can be understood as 4 separate, reversible reactions:



where A represents a impurity atom in a substitutional configuration, I a self-interstitial, V a vacancy, and A_i a impurity atom in a interstitial position. The forward of the first reaction occurs when a substitutional dopant pairs with a nearby interstitial to form a dopant-vacancy pair. This is commonly referred to as the vacancy mechanism of diffusion. In the second reaction a substitutional dopant pairs with a self-interstitial forming a dopant-interstitial pair. This is known as the interstitialcy mechanism, whereas Eq. 2.13 is the interstitial mechanism. These two are different in that the interstitial mechanism requires either the self-interstitial or substitutional dopant be completely "kicked" off the lattice site. In the interstitialcy mechanism the AI pair sort of share a lattice site as they migrate. It should be mentioned that the distinction between the interstitialcy/interstitial mechanisms is rarely made. The last reaction is known as the dissociative reaction or Frank-Turnbull mechanism diffusion. This requires a substitutional dopant to hop into an interstitial position, leaving behind a vacancy.

Most dopants are dominated by diffusion of either interstitials or vacancies. B, P, and Ga, diffuse mainly through interaction with interstitials, while Sb is nearly a pure vacancy diffuser. Arsenic, on the other hand, diffuses by interactions with both types of point defects. The fractional interstitial, f_i , or fractional vacancy, f_v , component determines the degree to which that dopant species prefers to diffuse via the particular point defect. These values are shown for different dopants in Table2-2.

2.2.2 Equilibrium Diffusion

Although point defects are efficiently created at room temperature, it does not approach the large supersaturation that can be created using ion implantation or other processes such as oxidation or nitridation. Under this case, a near equilibrium formulation for dopant diffusion can be introduced based on Fick's Laws of diffusion. Under these intrinsic and dilute dopant concentrations the flux of dopant A is expressed as

$$-J_A = d_{AV} \frac{\partial C_{AV}}{\partial x} + d_{AI} \frac{\partial C_{AI}}{\partial x} \quad (2.15)$$

where d_{AV} and d_{AI} are the diffusivities associated with the particular defect complex, C_{AV} and C_{AI} are the concentrations of the particular complex, and x is the one-dimensional distance of interest [FAH89]. This is a form of Fick's first law of diffusion which states that a flux of the impurity will occur in the presence of a concentration gradient. It can be shown that Fick's second law can be applied to near equilibrium such that

$$\frac{\partial C_A}{\partial t} = D_A^* \frac{\partial^2 C_A}{\partial x^2} \quad (2.16)$$

where C_A is the concentration of the dopant, t is time, and D_A^* is the equilibrium diffusivity of the dopant defined to be the sum of the equilibrium diffusivities of the AV and AI complexes [FAH89]. Basically, the change in concentration with time within a volume element is dependent on the difference in the flux of the impurity entering and leaving the volume element. Unfortunately, these formulations are highly idealized situations and are not applicable to the processes that take place during IC fabrication. This requires the use of equations that take into account the local point defect populations.

2.2.3 Non-equilibrium/Enhanced Diffusion

Enhanced diffusion refers to the phenomenon whereby dopants diffuse rapidly under a supersaturation of point defects. TED is a type of enhanced diffusion that proceeds for a specified amount of time, as long as secondary defects are able to store interstitials. A number of processes that commonly occur during IC fabrication significantly alter the point defect populations. It is obvious from the previous discussions that damage created by ion implantation can easily do this. Oxidation of the silicon surface is another method. Only a submonolayer of Si is required to form a monolayer of SiO_2 (ratio of $\sim 1:2.25$). This results in the injection of interstitials due to the net volume expansion difference between Si and SiO_2 . Oxidation enhanced diffusion (OED) of B and P is observed, while oxidation retarded diffusion (ORD) is observed for Sb [HUS74]. The opposite phenomena occurs as a result of nitridation (NED) and silicidation (SED). NED is believed to occur as interstitials are swept toward the surface, where they react to form Si_3N_4 leaving behind an excess of vacancies. In SED, vacancies are generated at the interface as silicon atoms are removed to react at the silicide-metal interface. Under these conditions, B and P diffusion is retarded, whereas Sb and As are enhanced. Examples of enhanced diffusion under nitridation is illustrated in Fig. 2-10. A number of non-equilibrium formulations are available to couple point defect and dopant diffusion and the reader is referred to the review articles for specifics.

2.2.4 TED of Boron

As mentioned previously, TED results from dopant interactions with interstitials stored in secondary defects. For a dopant such as B, which interacts very strongly with interstitials, this leads to unacceptable junction depths in bulk Si [JON98]. Figure 2-11 shows an example of the TED behavior of B as a result of the presence of $\{311\}$ defects. Significant motion of the profile is seen to occur at shorter times, while at long times the $\{311\}$ s have mostly dissolved

and can no longer drive TED. At this point, the B profile is mostly stable and the diffusivity exhibits more of the characteristics of near-equilibrium diffusion.

TED of B has a number of interesting characteristics and is affected by a number of implant and anneal parameters, including dose, energy, time, temperature, ramp rate, etc. Implant energy and dose tend to increase the amount of observed TED. However, saturation in the amount of TED occurs as the dose increases above approximately $1 \times 10^{15} \text{ cm}^{-2}$. This is attributed to stable dislocation loop formations, that act as strong sinks for excess interstitials. Similarly, intuition tells us that as time increases so does TED; at least under isothermal conditions. TED can be reduced by annealing at higher temperatures for shorter times, though. [JAI02] For this reason there has been considerable effort aimed at alternative annealing technologies such as rapid thermal annealing (RTA), laser thermal annealing (LTA), and FLASH lamp annealing. Each of these has specific advantages and disadvantages, but in general the goal is to obtain shallow junction depths by reducing TED, while at the same time enabling high dopant activation.

2.2.5 Boron Interstitial Clusters (BICs)

Equilibrium solid solubility of boron is well above $1 \times 10^{20} \text{ cm}^{-3}$ at temperatures of 850°C and higher [TRU60]. However, these levels of dopant activation are not obtained after annealing of ion implanted boron in silicon, even after TED has ended. The reason for this is attributed to the formation of boron interstitial clusters (BICs) due to a high interstitial supersaturation [STO95]. These defects consist of one or more boron atoms bound with one or more self-interstitials and should not be confused with the SMIC discussed earlier. In general, BICs are immobile and electrically inactive for the most part, although active BICs are believed to exist [LIL01]. An immobile peak in Fig. 2-11 is observed near the surface, which is where

the BICs reside. Complete dopant activation cannot be obtained until they dissolve; this requires long periods at high temperatures.

The kinetics of BIC dissolution have been investigated by a number of authors and the most significant findings are now discussed [PEL99b, HUA98, CRI03, MAN00, MAN01, SOL00, SCH00, LIL02, RAD02, MIR03]. The boron concentration threshold for BIC formation appears to be between $1 \times 10^{18} \text{ cm}^{-3}$ and $1 \times 10^{19} \text{ cm}^{-3}$. The amount of clustering depends strongly on the separation between the region of high boron concentration and peak of the interstitial concentration [JON96]. A thermal activation energy for BIC dissolution has been experimentally determined to be between 3.0 eV [LIL02] and 3.2 eV [MIR03]. These are significantly less than that found by Mokheri, et al., of 4.7 eV [MOK02]. However, this could be due to the different doses used in the studies. Lilak et al., [LIL02] used a dose of boron of $2 \times 10^{16} \text{ cm}^{-2}$, whereas Mokheri et al., [MOK02] used $1 \times 10^{15} \text{ cm}^{-2}$. These differences in concentration could result in BIC species with significantly different binding energies.

Ab initio and tight binding calculations have provided useful information on the relative stability of specific BIC configurations [ZHU96, CAT98, PEL99a, LIU00, LEN00, LUO01, ADE03, HWA03]. The model of Pelaz et al., is shown in Fig. 2-12 illustrating the formation energies required for evolution of BICs up to a size of B_4I_4 [PEL99a]. They came to the conclusion that BICs with a high interstitial content (e.g., BI_2 , B_3I_3 , B_4I_4) form at early times when the interstitial supersaturation is greatest. As annealing proceeds, the BICs emit interstitials that can contribute to TED leading to BICs with a lower interstitial content. Therefore, the most stable configurations are those where $m < n$ for a B_nI_m cluster. When the BICs completely dissociate the immobile peak then dissolves out, but only long after TED has ended.

2.3 Silicon-On-Insulator (SOI) Materials

Lilienfeld first proposed the idea of a three terminal device operating with an insulated gate in 1926 [LIL26]. His patent describes a thin layer of semiconductor deposited on an insulating material; thus, one could argue that the idea of a field effect transistor was first proposed as an SOI structure. SOI is most commonly described as a thin layer of silicon (typically hundreds of Å to a few microns thick) on top of an insulating material with an underlying bulk silicon substrate. The most common insulating material currently is silicon dioxide. To date, SOI has been incorporated into the process flow of nearly every major semiconductor company including IBM, Motorola, AMD, Intel, Philips, Canon, etc. [HAN02].

For years the advantages of SOI devices over bulk silicon were well documented, but SOI suffered from the inability to produce adequate, device-quality materials [HOV96]. Bulk silicon had a huge experience base and scaling in accordance with Moore's Law was easily met. In effect, SOI had a huge mountain to climb, in order to gain acceptance as a viable alternative.

Early SOI materials, such as silicon-on-sapphire (SOS), were mainly used in niche markets including space exploration and high temperature environments. In the late 1970s, separation by implanted oxygen (SIMOX) was developed and has become the most mature of all commercially available SOI materials [IZU98]. The 1990s saw development of advanced techniques for fabrication of SOI materials, such as the Smart-cut® and Nanocleave® methods. Today, the fabrication of SOI materials is a multi-billion dollar industry and is projected to account for 50% of the production of all wafers by 2008 [SOI03].

2.3.1 SIMOX

At present, the most mature of all SOI materials is the separation by implantation oxygen (SIMOX) process. Oxygen ion implantation was first used for the synthesis of silicon oxide in the late 1960s [WAT66]. However, it was not until the late 1970s that the SIMOX process was

actually developed [IZU78]. The 1980s and early 1990s saw considerable interest in enhancing the quality and throughput of SIMOX materials, as evidenced by the number of studies conducted [HEM83, JAU85, HAY80a, HAY80a, HAY80b, CEL86, CHA87, DOU87, WHI87, HOL84, MAO86]. In order to form a buried insulator using conventional ion implantation took over 2.5 days to implant a dose of $1.2 \times 10^{18} \text{ cm}^{-2}$ with a beam current of 100 μA [IZU91]. The development of a high current oxygen implanter by Eaton Corporation significantly reduced the processing time devoted to the implant step. The quality of the surface Si layer was enhanced by the use of lower doses and higher post-implant annealing temperatures [NAK90]. The advantages and disadvantages of the SIMOX process are shown in Table 2-2. Today, the IBIS Corporation is the largest producer of SIMOX wafers [IBI03].

The SIMOX process basically consists of three steps. The first step consists of high dose oxygen implantation at an elevated temperature ($> 500^\circ\text{C}$). This is done in order to prevent complete amorphization of the surface Si layer. Creation of an amorphous surface Si layer would be disastrous because it would be impossible to recrystallize off an amorphous BOX. Typical implant energies and doses would be 180 keV, $1.8 \times 10^{18} \text{ cm}^{-2}$ for standard SIMOX (180 nm surface Si/400 nm BOX), or 30 keV, $1 \times 10^{17} \text{ cm}^{-2}$ for low dose SIMOX (57 nm surface Si/47 nm BOX). A high temperature annealing step at 1300°C for 6 hours follows this. The annealing step is necessary in order to synthesize a box shaped buried SiO_2 layer. The final step may consist of polishing in order to remove oxidation at the surface as a result of the high temperature annealing. Despite the high temperature annealing, the BOX properties vary from thermally grown SiO_2 due to the presence of silicon islands, stoichiometry, increased oxygen concentration in surface Si, etc. For this reason, research has been done into other methods of SOI fabrication such as the Smart-cut® and Nanocleave® processes. However, the recent

development of the internal oxidation of Si (ITOX) process can help improve the dielectric properties of the surface Si/BOX interface in SIMOX materials, as well as eliminate many of the silicon islands [COL97].

2.3.2 SOITEC

While the SOI community made huge strides with the development of the SIMOX process, higher quality SOI materials could be made by utilizing thermal oxidation followed by wafer bonding [CON96, STA97]. Early attempts, such as bonded and etch-back SOI (BESOI), could not overcome the problem of material waste [COL97]. In the early 1990s, the Smart-cut® process was invented [BRU96] and resulted in the formation of the company SOITEC, now the largest producer of SOI wafers [SOI03]. The advantages of the Smart-cut® process are shown in Table 2-3.

An illustration of the Smart-cut® process is shown in Fig. 2-3. It utilizes two wafers, but results in one final SOI wafer and another bulk silicon wafer, which may be reused. The first step involves thermal oxidation of one wafer, which will later provide the BOX of the SOI wafer. Next, hydrogen ion implantation is performed through the BOX to the surface silicon thickness desired. The implant energy can be tailored to dictate the thickness of the surface Si layer, while the dose is around $5 \times 10^{16} \text{ cm}^{-2}$. The two wafers are then bonded together at room temperature via van der Waals forces at the two surfaces. A low temperature anneal (~600-700°C) is then performed in order for the implanted hydrogen to coalesce into micro bubbles. As the micro bubbles grow the pressure inside them increases until they fracture resulting in the splitting of the SOI wafer from the recyclable wafer. A second anneal is performed at 1100°C for two hours to strengthen the bond at the bonded interface. A final polishing step is required in order to smooth the surface after splitting [BRU97].

2.4 Interstitial and Dopant Interactions at Si/SiO₂ Interfaces

The foundation has been laid for understanding point defect-dopant interactions in bulk Si; this is now discussed in the context of the current investigations. Oxide growth kinetics and the Si/SiO₂ interface structure are one of the most well understood phenomena related to Si microelectronic fabrication thanks to the work of Deal and Grove [DEA65a]. Routine growth of SiO₂ on Si occurs for the formation of field oxides, masking oxides, pad oxides, and gate oxides, during IC fabrication. These are all in addition to the native oxide/Si interface that exists anytime a clean Si surface is exposed to the atmosphere. Thus, the presence of numerous Si/SiO₂ interfaces is unavoidable. The structure of these interfaces determines the manner in which point defects interact with them. Predicting dopant diffusion in SOI is further complicated due to the presence of a buried Si/SiO₂ interface, in addition to the native oxide/surface Si interface. Significant numbers of investigators have sought a better grasp of the interface reconstructions and electrical defects that exist at Si/SiO₂ interfaces, but few of these bothered to apply their findings to point defect interactions. It is also known that certain dopants prefer to remain in Si, while others tend to segregate towards SiO₂. However, only a handful of these studies used SOI substrates to understand the effect of a buried interface. These are discussed in the final section of the chapter.

2.4.1 Si (001) Free Surface and Si(001)/SiO₂ Interface Structure

Clearly the most studied of all condensed matter interfaces are the Si(001) surface and Si(001)/SiO₂ system. They are used in well over 95% of all semiconductor devices produced by the microelectronics industry [ZAN00]. This is due to excellent stability between Si and silicon dioxide, both thermally and electrically, as well as the low density of structural and electrical defects. Si(001) is the most common crystallographic orientation used for MOS fabrication due to its low interface state density ($\sim 1 \times 10^{10}$ charges/cm²) [STR00].

2.4.1.1 Si(001)

The surface free energy is governed by the ability of surface atoms to rearrange themselves into more favorable configurations. Surfaces that already possess a low surface free energy will not tend to reconstruct (e.g., metals), while those with high energies will. A perfect cut along the Si(001) leaves each surface atom with two dangling bonds. This causes the surface atoms to reconstruct into a (2x1) unit cell, forming rows of dimerized atoms, shown in Fig. 2-14. The driving force for the (2x1) reconstruction is the reduction in the number of dangling bonds from 2 to 1. The reconstruction appears to be stable up to temperatures of 1200 °C, although (1x1) and (4x2) unit meshes have also been observed [BAL88].

Vicinal Si(001) surfaces consist of rows of dimerized atoms that are orthogonal on adjacent terraces separated by single or odd number-layered steps, shown in Fig. 2-15. Thus, the existence of the (1x2) reconstruction must also be conjectured. The figure also illustrates the existence of two different types of single-layer steps, S_A and S_B . Dimers at the S_A step run parallel with the dimers in the upper terrace, while the S_B step dimers run perpendicular those in the upper terrace. This results in abrupt (S_A) or graded (S_B) steps depending on the orientation of the step dimer. The S_B step contains significant densities of kinks, while S_A steps appear to be fairly smooth. A scanning tunnelling microscope (STM) image of alternating S_A and S_B steps are shown in Fig. 2-16 illustrating the difference in the two steps [ZAN00].

For the current investigations, the free Si surface primarily idealistic. Interstitials would be able to annihilate if they were able to diffuse to surface and attach themselves to a step or kink. Thus, many investigators have treated the surface as an infinite source of vacancies and infinite sink for interstitials. However, the surface is practically always covered with some form of silicon oxide that will affect this treatment. Oxidation occurs by transport of oxygen (O_2) or

H₂O to the Si/SiO₂ interface where it reacts, pushing the interface deeper into the substrate. The position of the interface is continually changing, so the existence of a free Si surface is not critical in the present context, rather it is the arrangement of Si and O atoms at the Si/SiO₂ interface.

2.4.1.2 SiO₂

More than 95% of all rockforms on the earth possess silicon dioxide as the main constituent [PAN75]. It consists of tetrahedral SiO₄ structural units with an Si-O bond distance varying between 0.152 nm and 0.169 nm, shown in Fig. 2-17. Each oxygen atom is bonded to two silicon atoms, while each silicon is bonded to four oxygen atoms. The O-Si-O bond angle is 109.18°, while the Si-O-Si angle varies from 120° to 180° in crystalline SiO₂. There is also a rotational angle between tetrahedral that is either 0° or 60° for crystalline SiO₂. The way in which the SiO₄ tetrahedron are arranged in 3-D determines the specific crystal structure, or if it is random/amorphous. Figure 2-18 shows the different allotrophs of SiO₂ that exist at high pressures and elevated temperatures. Note under most oxidation temperatures the stable form is tridymite, but α and β quartz may also exist at lower temperatures. The density of these phases depends strongly on the Si-O bond length and Si-O-Si bond angle. Coesite is the densest form of SiO₂ due to its small, 120° bond angle. Three properties distinguish crystalline SiO₂ from amorphous SiO₂: (1) Rotational angle between adjacent tetrahedra may be any angle, (2) variation in Si-O-Si bond angle of 150 ± 15°, and (3) number of tetrahedra in rings may also vary, but 8, 10 and 12-membered rings are more energetically favorable [CHI97].

At room temperature for thermally grown oxides there is no long range order present. Instead, fused/amorphous silica is believed to be similar to a continuous random network (shown in Fig. 2-19) or collection of microcrystalline grains of SiO₄ tetrahedron arranged in

space. The network model can be thought of consisting of 8, 10, and 12-membered rings. The presence of voids in the structure can be seen; this accounts for the low measured density of fused silica ($\sim 2.2 \text{ g/cm}^3$) [CHI97]. The microcrystalline model presumes the distribution of Si-O-Si bond angles to be due to the presence of small grains that cannot be resolved using x-ray diffraction techniques. The grains would consist of different SiO_2 crystalline phases. A combination of the two models is likely most representative of amorphous silica. Thus, there may be short range order of the Si-O-Si bond angles, but a variation in the bond angles over the long range [BAL88].

2.4.1.3 Si/SiO₂ interface

While the growth kinetics of silicon oxidation are well understood, there remains a large amount of debate over the precise configuration of Si and O atoms in the vicinity of the Si/SiO₂ interface. The interface is not atomically abrupt, rather the transformation from Si to SiO₂ takes place over a few monolayers. Idealized models have been proposed using both crystalline and amorphous SiO₂, although both assume no broken bonds to exist at the interface [BAL88]. It is generally accepted that the interface consists of a transition region sandwiched between the bulk Si and amorphous silica regions, as shown in Fig. 2-20. The local bulk Si and SiO₂ are also altered near the transition region.

The transition region is believed to consist of non-stoichiometric suboxides, SiO_x that vary depending on their proximity to either the bulk Si or SiO₂. The suboxides can be detected using methods such as x-ray photoelectron spectroscopy (XPS) or photoemission spectroscopy (PES), although PES appears more sensitive [LUZ93]. The oxidation states Si^{+1} , Si^{+2} , and Si^{+3} , are associated with the Si 2p core levels and correspond to Si atoms with one, two, and three nearest oxygen neighbors, respectively [HOL83]. The thickness of the transition layer has been

estimated using quantitative PES and XPS to be between 0.6 and 1.5 monolayers ($\sim 5\text{-}8 \text{ \AA}$) thick [LUZ93]. The relative amounts of the particular oxidation state are sensitive to the growth temperature of oxidation [LUZ95]. Lu et al., found the areal density of the +2 and +3 states to increase with growth temperature, while the +1 state was fairly constant [LUZ95]. They attributed this to strain relaxation at the interface as more oxygen reaches the interface during growth.

Two structural defects are of primary interest to the Si/SiO₂ interface and are illustrated in Fig. 2-21. The E' defect consists of a broken bond between two tetrahedra that would otherwise be bonded to an O atom. One of the Si atoms then becomes positively charged, while the other keeps its unpaired electron in a dangling bond orbital. It has been hypothesized that the E' defect is the source of fixed positive interface charge [BAL88]. The P_b center consists of a broken bond in Si that would be bonded to another Si atom. This defect has been extensively studied using electron spin resonance (ESR).

Electrical defects of interest to the Si/SiO₂ system can be divided into four categories. Fixed oxide charge, Q_f , is net positive charge existing within the transition region of the interface with an areal density of $10^9 - 10^{11} \text{ cm}^{-2}$. It is given this nomenclature because the positive charge persists under normal device operation. This charge is believed to be due to incompletely oxidized Si atoms having obtained a positive charge. Q_{it} refers to trapped interface charge and may have a positive, negative, or neutral charge state. Similar to Q_f , these defects are believed to be due to Si atoms with unsatisfied bonds. The other two types of electrical defects are present in the oxide, but away from the transition region. Mobile ionic charge, Q_m , is associated with cations of alkali metals such as Na⁺ or K⁺. Oxide trapped charge, Q_{ox} , is due to broken Si-O bonds present in the oxide, created during processes such as ion implantation and

reactive ion etching. Fortunately, these last two defects are less significant today because of stringent contamination control and the ability of broken bonds to repair themselves during thermal processing. However, charge trapping due to Q_{ss} can cause shifts in threshold voltage in devices requiring current to be passed through the oxide (e.g., EPROM).

2.4.2 Point Defect Interactions at the Si/SiO₂ Interface

For a number of years the ability of an interface to alter point defect populations has been a concern and an issue of debate. TED is expected to be strongly affected by this, since it is strongly dependent on the interstitial supersaturation. If an interface efficiently allows interstitials to be trapped or annihilated it would serve to reduce TED. Thus, the ability to model the behavior of an interface greatly increases the reliability of process simulators for predicting dopant diffusion profiles.

Classically the silicon surface has been thought of as an infinite source of vacancies or infinite sink for interstitials. An interstitial diffusing towards the surface will instantaneously be annihilated. On the other hand, a vacancy diffusing to the surface acts to expand the free surface by annihilating a surface Si atom. Thus, many authors generically speak of kinks and traps as sites for interstitials to recombine or become immobile at the Si/SiO₂ interface, while mentioning nothing regarding what a kink or trap physically is. While this rudimentary picture is very useful for understanding processes such as epitaxy that involve atomic attachment to free surfaces, it does not create a realistic picture of interstitial recombination at the Si/SiO₂ interface. However, before delving into the intricacies of the physical processes underlying this, it is necessary to give a general description of the parameters for determining point defect generation and annihilation at interfaces.

The continuity equations governing point defects appear as a modification to Fick's second law with the addition of another term, thus for the two types of native point defects

$$\frac{\partial C_I}{\partial t} = d_I \frac{\partial^2 C_I}{\partial x^2} - k_{I,V} (C_I C_V - C_I^* C_V^*) \quad (2.17)$$

$$\frac{\partial C_V}{\partial t} = d_V \frac{\partial^2 C_V}{\partial x^2} - k_{I,V} (C_I C_V - C_I^* C_V^*) \quad (2.18)$$

where terms have been defined previously in Eqs. 2.8 and 2.9. These equations can be understood to mean the change in concentration of point defects in a volume element is determined by the flux entering and leaving minus the bulk recombination rate of both types of point defects. Thus, those defects that enter the volume element and do not leave must recombine with the opposite point defect within the bulk. In the case of an interface, where point defects can be created or annihilated it becomes necessary to invoke additional formulations

$$g_I + d_I \frac{\partial C_I}{\partial x} - K_{surf,I} (C_I - C_I^*) = 0 \quad (2.19)$$

$$g_V + d_V \frac{\partial C_V}{\partial x} - K_{surf,V} (C_V - C_V^*) = 0 \quad (2.20)$$

where g is the flux of point defect injection into the bulk, and K_{surf} is the recombination velocity. These equations can be understood as point defects created at an interface that do not diffuse into the bulk recombine at the interface. These processes are illustrated in Fig. 2-22 for the cases of bulk Si and SOI with the obvious difference being the presence of an additional interface for recombination in SOI.

2.4.2.1 Interface effects on interstitial kinetics under oxidizing conditions

The majority of studies for determining interface recombination velocities have involved measurement of the growth and shrinkage of oxidation induced stacking faults (OISF) and

oxidation stacking faults (OSF). Structurally, there is no difference between OISFs and OSFs; they are distinguished by how they are nucleated. OSFs nucleate off defects present before oxidation begins, such as dislocation loops, while OISFs prefer a more homogeneous path. These stacking fault defects are easily produced as interstitials are injected during high temperature oxidation of Si and form on {111} planes. Because of their extrinsic nature, the OSFs can drive the phenomenon of OED. The work of Hu was highly instrumental in this field as far as tailoring the OSF results with surface processes [HUS74, HUS75, HUS85a, HUS85b]. Since oxidation, under most conditions, follows a linear-parabolic growth law [DEA65a], Hu proposed a similar parabolic dependence of the interstitial injection flux

$$g_i(t) = \frac{A}{\sqrt{t_0 + t}} \quad (2.21)$$

where A is the oxidation growth rate constant, t is time, and t_0 is the time constant for separating the linear-parabolic transition [HUS85b]. This was later modified to a power law dependence by Fahey et al., as

$$g_i(t) = A(t_0 + t)^{-n} \quad (2.22)$$

that prevents infinite flux at time zero. [FAH89] In the absence of an energy barrier to recombination, Hu determined the interstitial recombination velocity to be

$$K_{surf,r} = \pi \rho a_0 d_i \quad (2.23)$$

where ρ is the density of surface kinks, and a_0 the capture radius [HUS85b, FAH89]. This equation assumes a constant kink density, but it is entirely possible that these sites could become saturated if the number of interstitials attempting to recombine is greater than the kink density. Hu also proposed the kink site density to be dependent on orientation [HUS74]. The mechanism of interstitial recombination proposed by Hu is illustrated in Fig. 2-23 [HUS74,

HUS94]. In this process, an interstitial or di-interstitial diffuses to the interface and recombines along a step edge or kink site near the transition region.

Taniguchi et al., used a boron implant to define the depth of OSFs followed by frontside and backside oxidation to observe their growth and shrinkage [TAN83]. Since the boron implant was close to the surface, backside etching had to be used to move the backside interface closer to the damage so the OSFs could nucleate. Polysilicon and silicon nitride films were deposited on the frontside prior to oxidation, so that only backside oxidation would take place. They found the maximum length of OSFs to decrease exponentially as the thickness of silicon increased. For silicon thickness 40 μm or less, the OSF length increased with oxidation time. The growth rate also increased as the thickness of silicon decreased. The 500 μm film did not result in growth of OSFs, while the 80 μm had a modest decrease at early times followed by an increase with oxidation time. They then developed a model based on the following: oxidation at the backside injects interstitials that diffuse to the frontside causing OSF growth. However, the interstitial concentration at the frontside must be greater than the equilibrium interstitial concentration in the vicinity of the fault in order for growth to occur. Using this model they were able to develop an empirical expression for the interstitial recombination velocity at the frontside interface, given by:

$$K_{\text{surf},f} = 4.6 \times 10^{-3} e^{\left(\frac{-2.4 \text{ eV}}{kT}\right)} \quad (2.24)$$

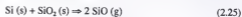
where $K_{\text{surf},f}$ is given in cm/s.

Ahn et al., used two different test structures to investigate 1-D and 2-D interstitial kinetics, shown in Fig. 2-24 [AHN87]. Figure 2-24(a) shows the 1-D test structure with 4 points of interest within the structure. Position 1 is blocked from oxidation since both the surface and backside are protected with silicon nitride, thus the phosphorus marker should diffuse close to

equilibrium conditions. Position 2 is protected at the backside, but interstitial injection occurs at the surface. Position 3 is protected at the surface, while backside oxidation occurs. Finally, the fourth position is not protected at either interface, so interstitial injection occurs from two directions. The 2-D test structure in Fig. 2-24(b) illustrates the reduction of trench width down to 3 μm , as interstitial injection occurs at the surface. They found the recombination velocity to vary based on the trench width, which they attribute to stress produced by bending of the silicon membrane. For a 20 μm trench they extracted $K_{\text{surf},1}$ to be 5×10^{-7} cm/s, while a 104 μm trench was found to be 2×10^{-7} cm/s. They seem to report an average recombination velocity of 3×10^{-7} cm/s at 1100°C. This is more than a factor of 2 less than that reported by Taniguchi et al., that found $K_{\text{surf},1}$ to be 7×10^{-7} cm/s at the same temperature [TAN83]. However, both these values of $K_{\text{surf},1}$ are lower than that extracted by Scheid and Chenevier [SCH86]. They found $K_{\text{surf},1}$ to be 25×10^{-7} cm/s. Ahn [AHN87] attempts to reconcile these differences by noting that Scheid and Chenevier [SCH86] assumed their nitride to be perfectly reflecting, while trying to obtain the recombination velocity at the pad-oxide interface. Differences in processing conditions could also lead to different oxide properties that could affect $K_{\text{surf},1}$. Taniguchi et al., [TAN83], used OSFs to determine the recombination velocity, whereas Ahn et al., [AHN87] used dopant diffusion of phosphorus. This difference could also explain the difference in values reported by the two authors.

In another experiment, Ahn et al., used both phosphorus and antimony diffusion, as well as OSF growth and shrinkage to monitor interstitial kinetics at the SiO_2/Si interface [AHN89]. In this case, the post fabrication annealing was done in an inert ambient using argon. They noted enhanced Sb diffusion, retarded P diffusion, and enhanced shrinkage of OSFs in the

proximity of the SiO_2/Si interface. This is attributed to a vacancy supersaturation due to the formation of SiO molecules as self-interstitials diffuse into the oxide according to the reaction:



It is proposed that the fast diffusing, gaseous SiO molecules efficiently transport interstitials from the interface. Unfortunately, the authors give no analytical evidence that such a reaction takes place, so another vacancy mechanism cannot be ruled out. It is also unclear whether the SiO formation only occurs under high temperature processing, since the authors only annealed at 1100°C . This has, in fact, been suggested by Celler and Trimble in a number of papers [CEL89a, CEL89b].

Only a few studies have been aimed specifically at studying interstitial interactions with interfaces using SOI materials. In their first study, Tsoukalas, Tsamis, and Stoemenos set out to investigate interstitial reactions with a thin oxide film in the structure shown in Fig. 2-25 [TSO93]. They oxidized a SIMOX wafer (W2) at 1100°C for 2 hours in order to grow OSFs, which they then directly bonded to another SIMOX wafer (W1). Prior to bonding, W1 had a thin oxide of 8 nm grown on the surface to serve as the transport site for the interstitials. After bonding, KOH etching was used to thin through the Si bulk from the backside of W1. The surface Si layer of W1 was then oxidized to inject interstitials that then diffused to the thin oxide to react. The growth of the OSFs was monitored to determine the transport mechanism of the interstitials through the oxide. Figure 2-26 shows the OSF length difference between the thinned SOI structure and reference samples as a function of oxidation time. It illustrates that the thinned samples tend to grow longer than the reference samples. A clear temperature dependence of the change in OSF length can also be seen. There is also a delay time constant associated with the OSF growth. The authors attribute this difference in growth [TSO93] and in

another study of isotopic Si diffusion [TSO01] to SiO formation at the front interface of the thin oxide given by the reaction of Eq. 2.25. Further, the SiO molecules then diffuse through the thin oxide and react at the back interface, according to the reverse reaction of Eq. 2.25. This effectively injects interstitials into the OSF layer leading to the growth. There are some problems with this explanation though. Once again, no analytical evidence is provided to suggest the reaction actually takes place. The authors also ignore the effects that oxidation of the thin oxide could play. Although most of the oxygen is expected to react at the surface, a small amount will also react at the other interfaces [COL97]. This could also provide additional interstitials to create the growth of OSFs. In their second study, Tsamis et al. investigated the lateral distribution of interstitials under a nitride mask using bonded SOI substrates [TSA95]. The test structures shown in Fig. 2-27 were used to investigate both the depth distribution of interstitials and the lateral distribution. Oxidation of the trenches was used to inject the interstitials and the growth of OSFs was monitored at the surface Si/BOX interface and under the nitride/pad oxide. Figure 2-28 shows the OSF length for varying surface Si thickness under wet and dry oxidation conditions. The data shows that thinner surface Si films result in smaller OSFs compared to bulk Si. Also, the effect is stronger under dry oxidation conditions compared to wet. The authors believe the reduction of OSF length in the lateral study is due to interstitials that diffuse to the surface Si/BOX interface and recombine. However, they do not explain why differences exist between the wet and dry oxidation. This is could be due to differences in the roughness of the Si/SiO₂ interface. Dry oxidation is known to create a rougher interface that could, in principle, lead to a higher recombination velocity at the surface. This roughness could be in the form of dangling bond defects or kink sites. This would explain why the OSFs are larger in the case of wet oxidation, but cannot explain the difference that is observed between

the different materials because the surface roughness would be the same. This suggests that there may also be differences at the surface Si/BOX interface due to the oxidation conditions.

Other studies using SOI materials were mainly aimed at reducing OISF formation for low-energy SIMOX fabrication [GIL99a, GUI92, GIL94]. During this process, sacrificial oxidation of the surface Si layer followed by etching in dilute HF is used to obtain thinner surface Si films. In their paper, Giles et al., propose a model based on vacancy injection from the surface at temperatures above 1190°C. They suggest this suppresses the interstitial supersaturation, thus inhibiting the growth of OISFs in SOI. It is also suggested that the interstitial supersaturation is further reduced by recombination at the surface Si/BOX interface, as mentioned above. Giles et al., also extended their studies to include bonded SOI wafers [GIL99b]. In this study they noted a stronger temperature dependence of OISF shrinkage in bonded SOI versus SIMOX. Also, the length of OISFs was, on average, greater in SIMOX.

2.4.2.2 Interface effects on interstitial kinetics under non-oxidizing conditions and due to ion implantation

Up to this point the analysis of recombination velocities dealt with injection of interstitials due to oxidation. Ion implantation potentially allows for interstitial recombination to be observed without injection of point defects from the surface during annealing. The implant damage may be brought closer to the surface by reducing the implant energy or by using a higher energy implant followed by lapping of the surface. The effect of the surface can then be studied using TEM studies of extended defect evolution. Other studies have used Si⁺ implantation close to a marker layer and then observed motion of the marker layer. Unfortunately, this has led to a range of experimental interpretations and significant debate remains over the effect of the surface on a interstitial supersaturation.

Lim et al., studied the affect of surface removal on the motion of a boron marker layer after it had been implanted with Si^+ [LIM95]. They found the Dt product to decrease monotonically with etch depth. The data was then found to fit with a recombination length of $0.1 \mu\text{m}$. From their study, they conclude that the surface is a strong sink for interstitials. A similar study was performed by Gossmann et al., without etching and by annealing in vacuum[GOS95]. They claim a depletion of interstitials occurs during annealing in vacuum, but do not propose any mechanisms for the behavior. Cowern et al., attempted to elucidate the effect of the surface by etching an amorphous layer produced by a 150 keV , $2 \times 10^{15} \text{ cm}^{-2}$, Ge^+ implant to varying depths [COW99b]. This was followed by a boron implant at 3 keV , $1 \times 10^{14} \text{ cm}^{-2}$ into the different layers. They noted a linear decrease in the diffusion enhancement as the EOR loop layer was brought farther from the surface. Their conclusion is that the surface is a great sink for interstitials, although their data seems to contradict that of Lim [LIM95]. Cowern basically concludes that a shallower amorphous layer enhances the diffusivity of boron because the interstitials are recombining at the surface, whereas Lim claims the recombination of interstitials reduces the boron diffusivity. It is unclear how these two authors came to the same conclusion, although their data is contradictory.

Similar results were also reported by Agarwal et al., but instead of etching the surface they simply reduced the Si^+ implant energy [AGA97b]. They found the diffusivity enhancement of boron doping superlattices (DSL) to decrease as the Si^+ implant energy was reduced from 5 keV to 1 keV [AGA97b]. From this they came up with a recombination length less than 10 nm , which is one order of magnitude less than that reported by Lim et al. [LIM95]. In a defect study without the boron DSL, Agarwal et al., noticed the formation of zig-zag $\{311\}$ defects, shown in Fig. 2-29, for low energy Si^+ implants [AGA97a, EAG96]. During growth, these particular

{311} defects appeared to unfault and then continue growing on another {311} plane. The zig-zag defects were also found to be significantly more stable than the normal rod-like {311}s. They also found that both types of {311} defects formed at energies as low as 1 keV, $3 \times 10^{14} \text{ cm}^{-2}$. This indicates that {311} defects still form before the interstitials can recombine at the Si/SiO₂ interface. This seems to contradict their other work in [AGA97b], but the authors do not address the point.

Other authors have all but confirmed the Si/SiO₂ interface is not a significant sink for interstitials under most conditions. The effect of the surface on EOR defect evolution after Ge⁺ implantation has been studied by a couple of authors. Omri et al., used etching of a single amorphous layer to bring the EOR damage closer to the surface [OMR96]. In their study, a 150 keV, $2 \times 10^{15} \text{ cm}^{-2}$ implant was used to produce a 175 nm continuous amorphous layer. Etching the amorphous layer down to 30 nm did not significantly change the flux of trapped interstitials to the surface. A change in defect density was observed when the amorphous layer was thinned to below 55 nm. They propose that the a/c interface acts as a diffusion barrier as the EOR loops begin to nucleate. However, only after solid phase epitaxy (SPE) has occurred while the loops are in the coarsening phase can the surface begin to have an effect. King et al., also studied EOR dislocation loop evolution after Ge⁺ implantation [KIN03a]. They studied the effect of lapping on the loop evolution for 5, 10, and 30 keV, $1 \times 10^{15} \text{ cm}^{-2}$ implants. These implants produced amorphous layers of varying depths, which were then lapped to bring the EOR damage closer to the surface. For example, the 10 keV amorphous layer was lapped to less than that of the 5 keV, yet the defect evolution did not vary between the 10 keV lapped and unlapped samples. The defects produced from the 5 keV implant dissolved faster than either of the 10 keV samples, shown in Fig. 2-30. This indicated that the 5 keV defects did not dissolve because

they were closer to the surface, but rather because of an implant energy effect. In a follow up study, King et al., found that the surface began to affect the defect evolution when the damage was brought to a depth of $\sim 60 \text{ \AA}$ [KIN03b].

2.4.3 Models for Interstitial Interactions at Si/SiO₂ Interfaces

Physically based modeling of interstitial recombination has been the subject of at least three groups' attention, in addition to the work of Hu discussed previously. Dunham developed a model to explain OED and ORD behavior, which he then applied to non-oxidizing conditions [DUN92]. He claims, based on his interpretation of other author's experiments, that the majority of interstitials produced during oxidation flow back into the growing oxide rather than diffuse into the bulk. The interstitial segregation coefficient is defined as the ratio of the equilibrium concentration of interstitials between SiO₂ and Si:

$$m = \frac{C_{SiO_2}^*}{C_{Si}} \quad (2.26)$$

Dunham's proposition would seem to be a legitimate basis for a model when the interstitial segregation coefficient is considered [AGA95, TSA98]. This is at least three orders of magnitude higher for interstitials in SiO₂ at 1100° C, according to the work of Agarwal [AGA95] and Tsamis [TSA98]. However, as Hu points out [HUS94], an anisotropic segregation coefficient, as suggested by Dunham could result in a perpetual motion device where two crystallographic faces intersect.

Tsamis and Tsoukalas developed a time dependent recombination velocity for non-oxidizing conditions, as suggested by Ahn [AHN87, TSA98]. Intuitively, this model makes sense since if the number of sites that can result in recombination is assumed to be a finite number. Thus, the interface would lose its effectiveness as a sink for interstitials with annealing time. They make the following assumptions: there exists a fixed concentration of interstitials in SiO₂,

the oxide extends infinitely in the lateral direction, and no sinks or sources of interstitials exist in the oxide. From this, they are able to define the time dependent effect surface recombination velocity:

$$K_{surf,eff}(t) = K_{surf,i}(0)e^{\frac{t}{t_0}} \operatorname{erfc}\left(\sqrt{\frac{t}{t_0}}\right) \quad (2.27)$$

which does not consider Si reaction at the interface. For reaction at the interface to form SiO it takes the form:

$$K_{surf,eff}(t) = 2k_i \frac{\sqrt{S_i+1}}{S_i} (\sqrt{S_i+1}-1)e^{\frac{(S_i+1)t}{t_0}} \operatorname{erfc}\left(\frac{(S_i+1)t}{t_0}\right) \quad (2.28)$$

where k_i is the reaction rate constants for Si and S_i is the supersaturation ratio of self interstitials in bulk Si. Some of the limitations of the model should be pointed out. The model is not applied to temperatures below 1050°C, which is more relevant in modern IC fabrication. The authors point out that interstitial incorporation into the oxide will decrease with temperature. This could severely limit the applicability of this model except in the case of oxidation.

Law et al., have also investigated point defect recombination at the Si/SiO₂ interface [LAW91, LAW98]. They were the first to attempt to correlate TED with OED by proposing di-interstitial recombination as a dominant mechanism [LAW98]. In the case of recombination being dominated by single interstitials, $K_{surf,i}$ is expressed as

$$F_{surf,i} = K_{surf,i}(C_i - C_i^*) \quad (2.29)$$

where $F_{surf,i}$ is the recombination flux of silicon interstitials at a non-oxidizing interface. For di-interstitial recombination, the recombination flux becomes proportional to the square of the interstitial concentration according to

$$F_{surf,i} = K_{surf,eff,2}(C_i^2 - C_i^{*2}) \quad (2.30)$$

where $K_{\text{surf},\text{SiO}_2}$ includes both the surface recombination velocity and a temperature dependent factor for the dependence of di-interstitial population on the interstitial concentration. Subsequently, the model is able to fit a variety of OED data and TED data including the interstitial concentration as a function of lateral distance for long and short channel stripe widths. The advantage of this model is that it can be applied at lower temperatures, where TED and SPE take place.

2.4.4 Dopant Segregation in the Proximity of Si/SiO₂ Interfaces

The following question should now be posed: Why is dopant segregation important? First, it may lead to alterations in the channel and source/drain doping profiles. This, in turn, affects the threshold voltage and device drive currents. Second, segregation to the oxide could change the properties of a gate oxide and the surface state density. These are just two reasons; others will be pointed out along the way. In this section, we begin with a thermodynamic description of impurity redistribution in a two phase system. Next, the effect of static (e.g., inert) and dynamic (e.g., oxidation) interfaces on dopant segregation is described. Finally, the specific studies aimed at understanding dopant distributions in SOI materials are reviewed.

2.4.4.1 Thermodynamic considerations

In order to understand the reasoning as to why an atom prefers to reside in one material instead of another, one must turn to a thermodynamic approach. Our present system can be thought of as a two phase region (Si and SiO₂) with a additional component/impurity (e.g., dopant atom). In order for the impurity to attain equilibrium within the two phase region, the chemical potential of the impurity on either side of the phase boundary/interface must be equal. The chemical potential is related to the activity according to

$$\mu_i^A - \mu_i^{A*} = \Delta\mu_i^A = RT \ln a_i^A = N_A kT \ln \alpha_i^A \quad (2.31)$$

where $\Delta\mu_k^A$ is the chemical potential of component A in phase k relative to a reference state, R is the ideal gas constant, T is temperature, and a_k^A is the activity of component A in phase k. In the last formulation, N_A is Avogadro's number and k is Boltzmann's constant. The activity given in Eq. 2.31 is valid at a particular temperature, composition, and pressure. The activity coefficient is typically used to describe the behavior of a component in a solution as is given as

$$a_k^A = \gamma_k^A X_k^A \quad (2.32)$$

where γ_k^A is the activity coefficient of component A in k, and X_k^A is the mole fraction. This suggests that if $\gamma_k^A > 1$, then $a_k^A > X_k^A$ and the impurity behaves as if there is actually more of it in k. On the other hand, if $\gamma_k^A < 1$, then $a_k^A < X_k^A$ and the component behaves as if there is less than suggested by the composition [DEH93]. For a dopant impurity at the Si/SiO₂ interface the concentration of the dopant on either side will be related to the activity coefficients as

$$\gamma_{Si}^A C_{Si}^A = \gamma_{SiO_2}^A C_{SiO_2}^A \quad (2.33)$$

where C_{Si}^A and $C_{SiO_2}^A$ are the concentrations of the dopant in Si and SiO₂, respectively. We can now redefine the segregation coefficient for dopants, along with volume and pressure, as

$$m = \frac{C_{Si}^A}{C_{SiO_2}^A} = e^{\left(\frac{V_{SiO_2}^A P_{SiO_2} + \Delta\mu^A}{RT}\right)} \times \frac{\gamma_{SiO_2}^A}{\gamma_{Si}^A} \quad (2.34)$$

where the terms are the same as those defined previously [GRO64a, CHA84]. Thus, when $C_{Si}^A > C_{SiO_2}^A$ the impurity is rejected from the SiO₂, while $C_{Si}^A < C_{SiO_2}^A$ means it tends to segregate to the oxide.

2.4.4.2 Dynamic boundary conditions

The case of oxidation represents a significantly different problem compared to inert ambient studies. This was studied extensively by Grove and others in the early 1960s [ATA60, GRO64a, GRO64b, DEA65b, SNO65]. Here the interface behaves as a moving boundary as the

SiO_2 grows at the expense of Si, effectively pushing the interface deeper within the bulk. This causes continual redistribution of the dopant during the oxidation process.

The diffusivity of the dopant in the oxide also plays a major role in the redistribution. A high diffusivity in the oxide could mean that the dopant tends to escape from the oxide into the gaseous ambient, leading to a dose loss effect. This will further affect the concentration of dopant in the silicon by means of Eq. 2.33. This is illustrated in Fig. 2-31 for both $m < 1$ and $m > 1$. A fast diffusing species in the oxide is shown to reduce both C_s^A and $C_{\text{SiO}_2}^A$ for either $m > 1$ or $m < 1$. Note that when diffusion through the oxide is slow, and $m < 1$, a pileup results on the Si side of the interface. This effect becomes even more pronounced during oxidation, and is often referred to as a "snow plow" effect.

Segregation coefficients for a number of dopants are summarized in Table 2-5. Although the precision of the numbers is low, a few general comments can be made. Boron appears to be the only dopant that prefers to reside in the oxide (e.g., $m < 1$), while P, As, Sb, and Ga, prefer Si (e.g., $m > 1$). The variation in m found by different authors seems to be due to their specific experimental conditions used to study the dopant segregation. Figure 2-32 shows secondary ion mass spectrometry (SIMS) profiles of As, P, and B, after oxidation in dry O_2 at 1100 °C for 30 minutes [SAK87]. Note the snow plow effect observed in P and As as oxidation proceeds, and its absence in B.

Several authors have proposed a temperature dependence of the segregation and mass transfer coefficients in order to model the behavior [SAK87, ALE98]. This also accounts for some of the discrepancies found in Table 2-5. The results of the temperature dependence of the segregation coefficient are shown in Fig. 2-33, as determined by Sakamoto et al. [SAK87]. Note that the B segregation coefficient shows a much more pronounced temperature dependence than

that of P or As. Aleksandrov and Afonin noted that the segregation coefficient can be a function of temperature, yet independent of the oxidation rate, when one considers the that

$$m = e^{\frac{(\varphi_{ox} - \varphi_{Si})}{kT}} \quad (2.35)$$

where φ_{ox} and φ_{Si} are the concentration-independent portions of the chemical potential in the oxide and silicon, respectively [ALE98].

2.4.4.3 Static boundary conditions

More recently, the segregation of dopants at stationary Si/SiO₂ interfaces has taken on increased importance. This is due to the drive towards continually shallower junctions, which often use low energy ion implantation close to the surface to produce the shallow dopant profiles. This can result in the phenomenon referred to as "uphill diffusion", whereby a dopant appears to diffuse towards the surface rather than into the bulk.

Charitat and Martínez investigated boron segregation at the Si/SiO₂ interface using the nitride stripe pattern shown in Fig. 2-34 [CHA84]. This allowed them to also include the role of stress on the segregation. In addition, they also studied the orientation dependence. Figures 2-35 and 2-36 show the segregation coefficient as a function of temperature for <100> and <111> orientations, respectively. The nitride layer can be seen to significantly increase the segregation coefficient for both orientations by preventing the incorporation of boron into the pad oxide. On the contrary, the orientation does not appear to affect the segregation coefficient to any substantial degree. In general, m appears to increase between 850 °C and 950 °C, followed by a gradual decrease as the temperature is further increased. The authors attribute this phenomenon to viscous flow of the oxide above 1000 °C. They suggest the pressure term in Eq. 2.34 plays the most important role in affecting m . Unfortunately, they were unable to quantitatively measure the stress to strengthen their argument. Tensile stress in the nitride film is able to

explain the increase in m . Since boron produces a tensile stress in the Si lattice, another tensile stress at the surface will serve to repel the boron preventing further incorporation into the oxide.

Numerous authors have observed the phenomenon of uphill diffusion of B [WAN01, KAS00, SHI01, DUF03], Sb [SAI85] and As [KAS98, SAI85] in recent years. Figure 2-37 illustrates this for an ultra-low energy boron implant. Note the segregation of boron near the surface towards the native oxide. In general, the same trends are observed for the different dopants as discussed previously: B segregates to the oxide, while As tends to pileup on the Si side of the interface. Duffy et al., found the uphill diffusion of B to be highly sensitive to the Ge preamorphization energy [DUF03]. They found very little pileup of B without preamorphization, while the pileup increased as the preamorphization energy was increased. The amount of tail diffusion also increased with preamorphization energy, and this was attributed to both the increased EOR damage and a "chemical pump" effect as a result of a high substitutional concentration of B. These results were somewhat contradictory to those found by Kasnavi et al., when comparing B and BF_3 implants [KAS00]. They found the dose loss to the oxide to increase as the BF_3 energy was reduced, and the loss was greater than that for B alone. This difference can partly be attributed to the fact that the BF_3 implants were amorphizing, although it is unclear the role that F could be playing. This is supported by the fact that they saw a reduction in dose loss for BF_3 implants performed at $2 \times 10^{13} \text{ cm}^{-2}$. Kasnavi et al., also used XPS to determine that the majority of segregated As resides within the first monolayer of Si [KAS98]. Similarly, Sai-Halasz et al., previously found Sb and As to be confined to a single monolayer at the interface [SAI85].

2.4.4.4 Consequences of dopant segregation

Three consequences of dopant segregation should now be emphasized: dopant trapping, precipitation, and electrical deactivation. Clearly, the loss of dopant to an oxide will show an electrical deactivation effect since there cannot be any donors or acceptors in such an insulating material. It has also been reported that trapping of dopants at the interface also results in deactivation [SAI85, VUO00]. Precipitates of segregated impurities such as Pb, [HOL88] Ag, [HOL88] As, [IAC98b] Ge, [IAC98a, RAI96] and Sb, [WIL92] have been observed to form at the Si/SiO₂ interface upon annealing.

As mentioned above, the work of Sai-Halasz et al., found the majority of segregated Sb and As to be confined to a monolayer at the interface [SAI85]. After implantation and annealing in an inert ambient, the dopants segregated to the interface and appeared to remain attached. The dopants remained attached until an areal density of dopants approaching $2 \times 10^{14} \text{ cm}^{-2}$ was realized. Using Van der Pauw measurements they were able to determine that the trapped Sb dopants at the interface were electrically inactive. They also note that if a interface sticking coefficient of unity is assumed, ~25% of the implanted As dose can effectively be lost when the implant dose is less than $5 \times 10^{14} \text{ cm}^{-2}$.

The importance of dopant precipitation at the interface is also of profound importance, since it can affect the gate oxide quality. Iacona et al., found SiAs precipitates to form at relatively high doses ($3 \times 10^{16} \text{ cm}^{-2}$) during oxidation, but did not form at $3 \times 10^{15} \text{ cm}^{-2}$ [IAC98b]. The precipitates were determined to have a monoclinic crystal structure and lie on the {111} plane of Si. Their presence also led to significant changes in not only the interface morphology, but also the surface roughness.

2.4.4.5 Models for dopant segregation

In recent years, a number of authors have recognized the need for accurate modeling of dopant-interface interactions. Vuong et al., investigated the affect of dopant trapping on device characteristics for BF_2 , P, and As implants [VUO00]. They were able to successfully model the device data for surface-channel and buried-channel devices for both NMOS and PMOS using a trap and detrap methodology. Their model is based on the hypothesis that a flux of dopant arrives from the bulk and becomes trapped at the Si/SiO_2 interface according to

$$J_{\text{trap}} = r_t C_{\text{Si}}^A \left(1 - \frac{Q_{\text{trap}}}{N_{\text{trap}}}\right) \quad (2.36)$$

where J_{trap} is the flux of dopants becoming trapped at the interface, r_t is the dopant trapping rate, C_{Si}^A is the active dopant concentration, Q_{trap} is the areal trapped dose, and N_{trap} is the maximum number of trap sites. In Eq. 2.36, note that the trapped flux is proportional to the active dopant concentration indicating that trapping will become increasingly important at future technology nodes. They also developed another equation to simulate detrapping effects

$$J_{\text{detrap}} = \frac{r_d Q_{\text{trap}}}{t_{\text{trap}}} \quad (2.37)$$

where J_{detrap} is the detrap flux, r_d the detrap rate, and t_{trap} the thickness of the trapped layer.

Ab initio methods were used by Dabrowski et al., to investigate the mechanism of dopant segregation of P and As [DAB02]. These included substitutional donor atoms just below the interface, bonding donor and oxygen atoms, Si dangling bonds, dopant pairs, and defects with unoxidized Si. The last mechanism included a silicon bridge, ledge atom, or a Si vacancy at an unoxidized but fully coordinated Si atom. They found a high energy gain for donor trapping at electrically active defects (e.g., unoxidized dangling bonds), but this process was only efficient at low donor concentrations. For trapping at electrically inactive defects (e.g., unoxidized step

ledges and bridges) the energy gain was lower, but still occurred frequently at high concentrations. This mechanism relied on migration and recombination of dangling bonds, along with reoxidation of the Si bridges. Dopant pairing trapping mechanisms were found to dominate at very high concentrations because the interface becomes saturated with as much as a monolayer of inactive donors.

More recently, work in the laboratory of E. G. Seebauer has sought alternative explanations for the phenomenon of dopant segregation [DEV03, JUN04, DEV04]. Using photoreflectance (PR), they were able to quantify the degree of band bending at the Si/SiO₂ interface after Ar⁺ implantation at 0.5 keV, $1 \times 10^{15} \text{ cm}^{-2}$ [DEV03]. Band bending persisted at temperatures up to 940 °C for several minutes. This resulted in a change in the surface potential of 0.4 and 0.52 eV for as-implanted with oxidation and oxide-free surfaces, respectively. The presence of the change in surface potential results in a net electric field as shown in Fig. 2-38. The electric field tends to repel positively charged interstitials attempting to move from the bulk towards the surface. Interstitials closer to the surface can be negatively charged due to the position of the Fermi level near midgap, and move uninhibited towards the surface. Jung et al., developed a model for predicting both TED and dopant segregation based on these results [JUN04]. Using the general form of Eqs. 2.17 and 2.18, and incorporating an electromigration term to Fick's first law, they were able to model a variety of TED and segregation data. Their general flux and electric field equations are given as

$$J_j = -D_j \frac{\partial C_j}{\partial x} + z\mu_j C_j E(x) \quad (2.38)$$

$$E(x) = -\frac{\partial \Psi}{\partial x} \quad (2.39)$$

where z is the charge on species j , μ the mobility, E the electric field, and Ψ the electrostatic potential. They included boron interstitial transitions of $(+/-)$ and $(+/0)$ and a $(++/0)$ transition for self-interstitials in the model. Their model shows an excellent fit with both the tail diffusion and surface effects exhibited by boron in Fig. 2-39. They also indicate that their model provides an alternative explanation for the boride-enhanced diffusion (BED), previously observed in a number of studies [AGA99, COW99c]. Jung et al., indicates that the formation of a boride phase will then lead to a number of interfaces with possibly larger potentials; this could make the diffusion appear more enhanced [JUN04].

2.5 Dopant Diffusion in SOI

This section focuses specifically on diffusion studies performed using SOI substrates. Boron is focused on because of its pertinence to the studies in Chapter 6. It should be emphasized that as SOI material has evolved over the years, so the results of experiments may also vary over the course of a few years. Thus, the results from earlier studies must be put into context with more recent ones. For example, an experiment performed using early SIMOX material will likely yield different results from one using state of the art SIMOX today.

2.5.1 Boron Diffusion in SOI

The ability of SOI material quality to affect the physics of processing was recognized in early studies of boron diffusion by Normand et al. [NOR90]. They studied BF_3 implants in SIMOX materials that had been fabricated in 1986 and 1988. Figure 2-40 shows SIMS profiles for BF_3 implants at 40 keV, $1 \times 10^{14} \text{ cm}^{-2}$ into the 1986 and 1988 specimens. Significant differences in the pileup of boron near the surface can be seen to occur upon annealing in nitrogen at 880 °C for 100 minutes. The boron appears to pileup over a larger depth and lower concentration in the 1986 SIMOX compared to the 1988. However, a higher concentration of

boron at the surface Si/BOX interface was found in the 1986 sample. Cross-sectional TEM (XTEM) analysis showed a high density of SiC precipitates and threading dislocations in the 1986 specimens, while the 1988 showed no signs of process induced defects. This difference was attributed to carbon contamination as a result of a long implant time used to fabricate the 1986 substrates. The 1988 SIMOX were fabricated using a high current implanter, similar to that used to produce state of the art SIMOX today and allows for a much shorter implant time. The threading dislocations may have been the reason for the enhanced diffusivity of B in the tail region for the 1986 SIMOX. Spreading resistance profilometry (SRP) of the surface Si layer showed that the boron piled up near the surface was inactive.

The most extensive studies of boron diffusion in SOI materials were done by Crowder et al., in the mid 90s [CRO94a, CRO94b, CRO95]. They used boron marker layers to study OED and TED in SIMOX and bonded SOI materials. They noted an enhancement in the recombination velocity of interstitials in single implant versus multiple implant SIMOX materials. They attributed this to differences in the surface Si/BOX interfacial roughness. SUPREM IV was used to simulate the OED and TED profiles. An effective recombination velocity at the surface Si/BOX interface for bonded SOI was extracted and found to be $K_{\text{surf}}/D_1 = 4.7 \times 10^{-3} \exp(+1.34/kT)$.

Vuong et al., studied the phenomena of B pileup and clustering in SOTTEC materials with surface Si thickness of 60-70 nm and BOX thickness of 200 nm [VUO99]. They used both B marker layers and implants along with, in some cases, Si⁺ implants. SIMS profiles of B implanted at 10 keV, $1 \times 10^{13} \text{ cm}^{-2}$ are shown in Fig. 2-41. Top curves show Si signals obtained from SIMS. Following the B implant a 1050 °C, 60 second anneal was performed. Solid curves had an additional Si⁺ implant at 40 keV, $5 \times 10^{13} \text{ cm}^{-2}$. Both samples were then annealed at 800

°C for 30 minutes. A significant increase in the pileup at both the screen oxide/surface Si and surface Si/BOX interface can be seen to occur with the addition of the Si⁺ implant. Figure 2-42 shows SIMS profiles of B marker layers grown on SOITEC substrates using molecular beam epitaxy (MBE) and doped to a concentration of $1 \times 10^{18} \text{ cm}^{-3}$. Solid curves also had a Si⁺ implant at 25 keV, $1 \times 10^{14} \text{ cm}^{-2}$. Once again, enhanced segregation of B to the surface Si/BOX interface occurred with the additional Si⁺ implant. This allowed the authors to come to the conclusion that self-interstitials significantly aid the pileup of boron in SOI films. However, the marker layer was grown extremely far from the surface Si/BOX interface (~100 nm). If this were not the case, perhaps noticeable segregation would have occurred in the unimplanted case. SIMS is unable to resolve the low concentrations of B far from the marker layer, so it is impossible to comment on the unimplanted marker. In their clustering study, they found little difference in the clustering behavior between SOI and bulk Si. Less diffusion did occur in the tail region in SOI, though. The authors believe the clusters form at early times before interstitial recombination becomes a critical factor.

Recent work at IBM has investigated the effect of implant energy and surface Si thickness on B diffusion [PAR99, DOK02]. In Park's experiment, using SIMOX of varying thickness they implanted B and BF₂ at equivalent energies to give the same projected range of the implant [PAR99]. Figure 2-43 shows the B from BF₂ redistribution after RTA at 1000 °C for 5 seconds in nitrogen. A pileup of B appears on both sides of the surface Si/BOX interface in the 530 Å SOI, but the effect diminishes as the surface Si thickness is increased. The effect was also not as pronounced at low implant energies.

2.5.2 Donor Diffusion in SOI

In their study, Park et al., also investigated P and As diffusion [PAR99]. Phosphorus SIMS profiles are shown for each of the different thickness in Fig. 2-44. It shows a significant reduction in the pileup of P compared to the B in Fig. 2-43. A similar result was obtained for As. They proposed a model to try and account for differences between B, P, and As in SOI. It incorporated stress at the surface Si/BOX interface due to compressive stress in the BOX, gradual oxygen concentration at the interface, interface transport, and thermomigration.

Arsenic diffusion has also been studied by a few other investigators [OGU01, NOR89, ROB90, SAT95]. In general, all these authors found As to pileup on the surface Si side of the surface Si/BOX interface. Normand et al., also noted an enhanced diffusivity of As in their SOI films [NOR89], but this was disputed by Robinson et al. in their experiment [ROB90].

Phosphorus diffusion was also studied extensively by Crowder in experiments similar to those mentioned previously [CRO94a, CRO94b, CRO95]. They found significantly less diffusion of P in their OED experiments and this was confirmed by Uchida and co-workers [UCH00].

2.6 Summary

This chapter has reviewed the current understanding of point defect physics and how they relate to SOI technology. After ion implantation, interstitials may undergo a number of evolutionary stages that determine the effect they have on the diffusion of dopants. The presence of interfaces is unavoidable in microelectronic processing and their interactions with point defects and dopants must be accounted for in order for process simulators to provide accurate results. Conflicting results from a number of studies cloud the true nature of how the Si/SiO₂ interface interacts with interstitials. Several methods are currently available for

fabricating SOI substrates, but the most prevalent are the Smart-cut™ and SIMOX methods. It is clear that the type and age of a SOI substrate may significantly alter the process physics and must be accounted for when conducting a experiment.

Table 2-1. Advantages and disadvantages of ion implantation compared to gas source and solid source diffusion.

Advantages	Disadvantages
Easy introduction of desired impurity into target	Ion channeling
Good mass-charge separation	Crystal damage
Accurate dose control	Transient enhanced diffusion (TED) makes ultra shallow junction formation difficult
Not confined to surface	Extended defects can be source of leakage current within device
Not limited by solid solubility	
Reproducibility of impurity profiles	
Lower process temperature	
Ability to tailor doping profiles	

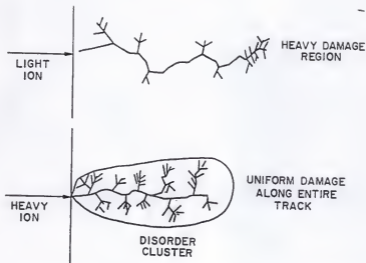


Figure 2-1. Schematic of collision cascade produced by light ions (e.g. atomic weight less than Si) and heavy ions (e.g. atomic weight greater than Si).

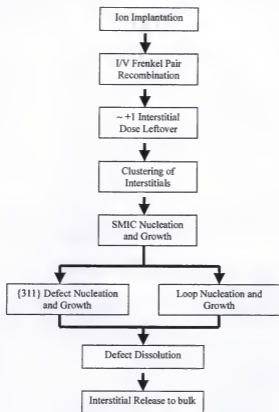


Figure 2-2. Evolutionary path for point defects produced by ion implantation.

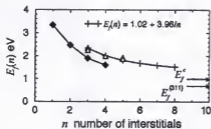


Figure 2-3. Formation energy as a function of cluster size for self-interstitial defects in Si. Closed diamonds represent formation energy for a compact cluster, while the open triangles are for an elongated cluster [KIM00].

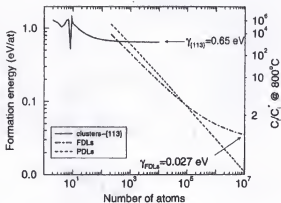


Figure 2-4. Formation energy as a function of cluster size as determined by Cowern et al., [COW99a].

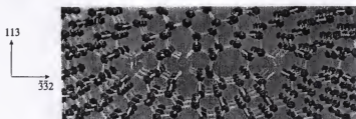


Figure 2-5. 3D representation of {113} defect in Si lattice. Light gray balls show interstitial chains along $\langle 110 \rangle$ direction [TAK91].

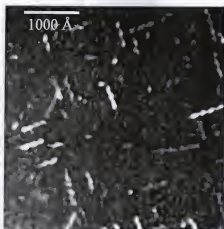


Figure 2-7. Plan view TEM (PTEM) weak beam dark field (WBDF) micrograph of {311} defects in Si.

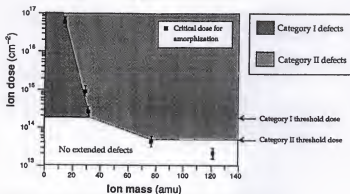


Figure 2-8. Formation criteria for extended defects in Si [JON88].

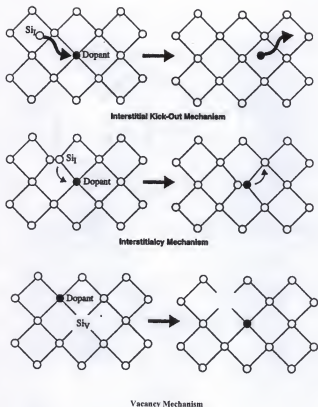


Figure 2-9. Mechanisms of dopant diffusion in the Si lattice [CRO95].

Table 2-2. Approximate fractional interstitial and vacancy components for various dopants in Si.

Impurity	Fractional Interstitial	Fractional Vacancy
Boron	0.8 - 1	0 - 0.2
Phosphorus	0.9 - 1	0 - 0.1
Arsenic	0.4	0.6
Antimony	0.02	0.98
Silicon	0.6	0.4

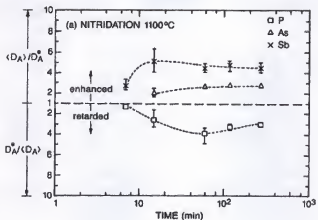


Figure 2-10. Enhanced and retarded diffusion of dopants under nitridation ambient conditions [FAH89].

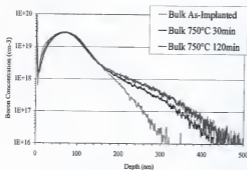


Figure 2-11. Example of TED of boron due to the presence of $\{311\}$ defects. Sample was implanted with boron at 19 keV, $3 \times 10^{14} \text{ cm}^{-2}$ and annealed at 750°C. The $\{311\}$ s regulate the release of the excess interstitials until their eventual dissolution at longer times.

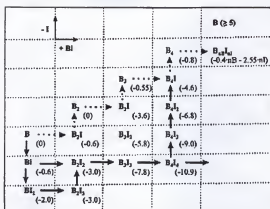


Figure 2-12. Energetics of evolutionary pathways for BIC formation [PEL99a].

Table 2-3. Advantages and disadvantages of the SIMOX process.

Advantages	Disadvantages
Most mature SOI technology	Silicon islands
One bulk wafer yields one SOI wafer	Process time
Defect density can be made low	Requires high current implanter
Simpler process	
Cheap in terms of SOI materials	

Table 2-4. Advantages and disadvantages of using Smart-cut process for fabrication of SOI substrates.

Advantages	Disadvantages
One bulk Si wafer produces one SOI wafer	Alignment during bonding
Absence of silicon islands in BOX	Poor adhesion during layer transfer
Better electrical properties than SIMOX	Touch polishing required
No significant damage to device layer due to H^+ implantation	Newer technology
Good uniformity of layers	

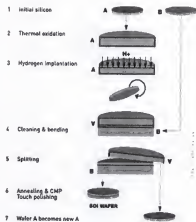


Figure 2-13. Schematic of the SOITEC process [SOI03].

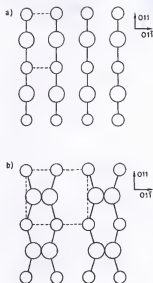


Figure 2-14. Surface reconstruction of Si (001) (1x1) to (2x1). Larger circles represent surface atoms, while smaller ones are one layer below [BAL88].

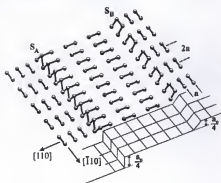


Figure 2-15. Schematic of vicinal Si(001) surface illustrating orientation of dimers on adjacent steps. Note existence of two different single-layer steps S_A and S_B [ZAN00].

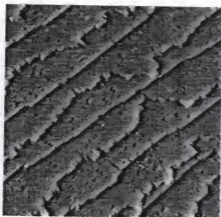


Figure 2-16. STM microscope image of vicinal Si(001) surface misoriented 0.5° along the $[110]$ direction. Alternating S_A and S_B steps are shown. Note smoothness of S_A steps and high density of kinks along S_B steps $[ZAN00]$.

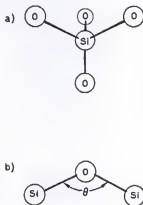


Figure 2-17. Structural basis of silicon dioxide – the SiO_4 tetrahedron. Note the constant tetrahedral angle and varying Si-O-Si bond angle [BAL88].

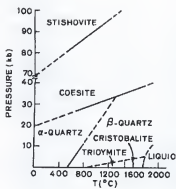


Figure 2-18. Phase diagram of crystalline forms of SiO_2 [BAL88].

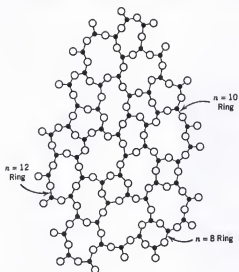


Figure 2-19. Continuous random network of A_2B_3 glass, similar to that present in fused silica [CHI97].

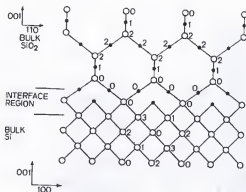


Figure 2-20. Schematic illustration of Si/SiO₂ interface with crystalline, cristobalite, form of SiO₂. Note presence of transition region consisting of non-stoichiometric SiO_x [BAL88].

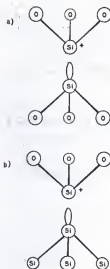


Figure 2-21. Structure of broken bond defects at the Si/SiO₂ interface. (a) The E' defect consists of a broken bond between two tetrahedra that would otherwise be bonded to O. (b) The P_b center consists of a broken bond in Si that would be bonded to another Si atom [BAL88].

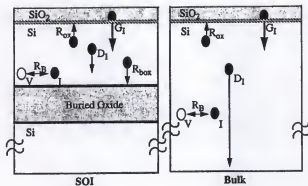


Figure 2-22. Schematic illustration of generation, diffusion, and recombination sources in SOI and bulk structures [CRO95].

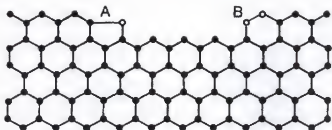


Figure
2-23.

Schematic of surface retrogrowth process proposed by Hu at an inert Si/SiO₂ interface [HUS74, HUS94].

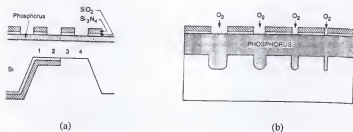


Figure 2-24. Schematic cross sections of test structures used by Ahn et al., for determining (a) 1-D and (b) 2-D interstitial kinetics [AHN87].

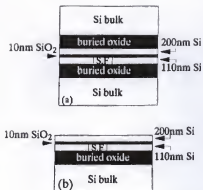


Figure 2-25. SOI structure used by Tsoukalas to study interstitial kinetics through an oxide (a) before backside etching of W1 and (b) after etching [TSO93].

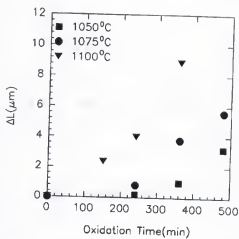


Figure 2-26. Difference in OSF length between thinned structure and control as a function of oxidation time for range of temperatures [TSO93].

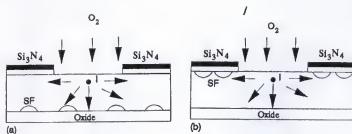


Figure 2-27. Test structures used by Tsamis to monitor (a) depth dependence of interstitial behavior and (b) lateral diffusion of interstitials under an oxidizing ambient [TSA95].

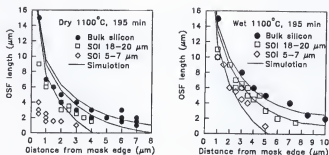


Figure 2-28. OSF length as function of distance from mask edge for SOI with varying surface Si thickness after dry and wet oxidation at 1100°C [TSA95]. Simulations were performed using data from Taniguchi [TAN85].

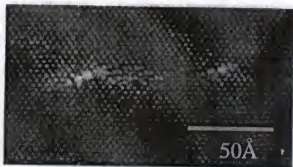


Figure 2-29. HRTEM micrograph showing zig-zag {311} defects produced by low energy Si^+ implantation at 5 keV, $3 \times 10^{14} \text{ cm}^{-2}$. Sample was annealed at 810°C for 10 minutes [AGA97a].



Figure 2-30. PTM micrographs showing defect evolution after Ge⁺ implantation at 5 keV and 10 keV, $1 \times 10^{15} \text{ cm}^{-2}$. (a) 10 keV unlapped, (b) 10 keV lapped, and (c) 5 keV. Samples were annealed at 750°C for 60 minutes [KIN03].

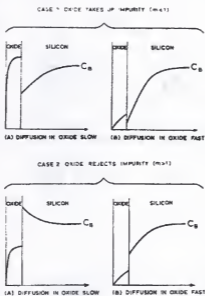
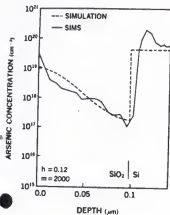


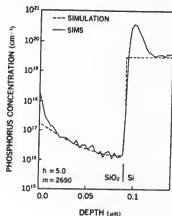
Figure 2-31. Effect of impurity redistribution on segregation coefficient and diffusivity in SiO_2 [GRO64a].

Table 2-5. Segregation coefficients determined for various impurities in Si during oxidation.

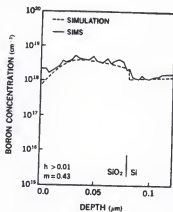
Boron	Phosphorus	Arsenic	Antimony	Gallium
0.3 [GRO64a]	10 [GRO64a]	10 [GRO64a]	10 [GRO64a]	20 [GRO64b]
0.01 [GRO64b]	2650 [SAK87]	2000 [SAK87]		
0.43 [SAK87]	175 [STI88]	800 [FAI81]		
0.1-0.5 [ANT79]				
0.1-0.33 [VAN85]				
0.58->2 [FAI78]				



(a)



(b)



(c)

Figure 2-32. SIMS profiles of dopant segregation for (a) arsenic, (b) phosphorus, and (c) boron after oxidation at 1100 $^{\circ}\text{C}$ for 30 minutes [SAK87].

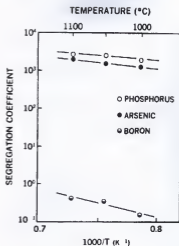


Figure 2-33. Temperature dependence of the segregation coefficient during oxidation for B, P, and As [SAK87].

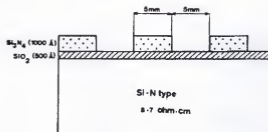


Figure 2-34. Test structure used by Charitat and Martinez to investigate boron segregation at a static Si/SiO₂ interface [CHA84].

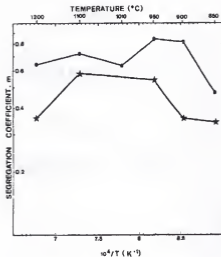


Figure 2-35. Boron segregation coefficient as a function of temperature for <100> orientation under neutral annealing ambient. Stars indicate segregation coefficients for a Si surface covered with a pad oxide only. Circles indicate segregation coefficients for a Si surface covered with a pad oxide and nitride as shown in Fig. 2-34 [CHA84].

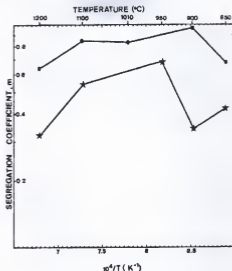


Figure 2-36. Boron segregation coefficient as a function of temperature for <111> orientation under neutral annealing ambient. Stars indicate segregation coefficients for a Si surface covered with a pad oxide only. Circles indicate segregation coefficients for a Si surface covered with a pad oxide and nitride as shown in Fig. 2-34 [CHA84].

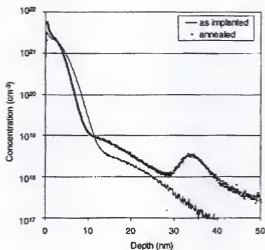


Figure 2-37. SIMS profiles of B, 0.5 keV, $1 \times 10^{15} \text{ cm}^{-2}$ annealed at 700 °C for 2 hours. Sample was preamorphized with Ge, 15 keV, $1.2 \times 10^{15} \text{ cm}^{-2}$. Note uphill diffusion of boron near surface, as well as gettering of boron to EOR damage around 34 nm [DUF03].

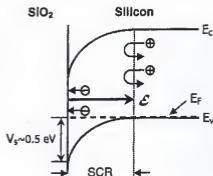


Figure 2-38. Potential energy diagram for electrons in p-type Si following Ar^+ implantation. Interfacial defects absorb positive charge from the bulk and create a space charge region (SCR) and electric field pointing back into the bulk. Positively charged interstitials are repelled back into the bulk by the field. Interstitials close to the surface are able to recombine since the Fermi level approaches midgap [JUN04].

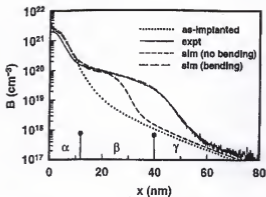


Figure 2-39. Simulation of boron TED experiment using model of Jung *et al.* Note incorporation of surface band bending results in best fit to overall profile [JUN04].

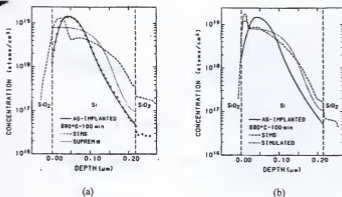


Figure 2-40. SIMS profiles of boron after BF_2 implantation at 40 keV, $1 \times 10^{14} \text{ cm}^{-2}$ into (a) 1986 and (b) 1988 SIMOX material. Anneals were 880 °C for 100 minutes in a nitrogen ambient. Note difference in pileup of boron at native oxide/surface Si interface [NOR90].

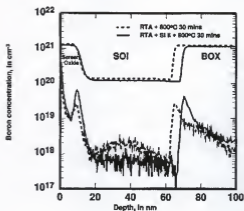


Figure 2-41. SIMS profiles of B implanted at 10 keV, $1 \times 10^{13} \text{ cm}^{-2}$ into SOITEC substrates with surface Si thickness of 60-70 nm and BOX thickness of 200 nm. Top curves show Si signals obtained from SIMS. Following the B implant a 1050 °C, 60 second anneal was performed. Solid curves had an additional Si^+ implant at 40 keV, $5 \times 10^{13} \text{ cm}^{-2}$. Both samples were then annealed at 800 °C for 30 minutes. Note increased pileup at both interfaces with addition of Si^+ implant [VUO99].

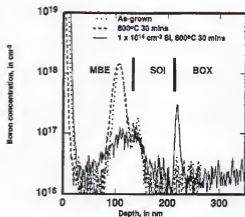


Figure 2-42. SIMS profiles of B marker layers grown on SOITEC substrates using MBE. Solid curves also had a Si⁺ implant at 25 keV, $1 \times 10^{16} \text{ cm}^{-2}$. Note enhanced segregation of B to surface Si/BOX interface with addition Si⁺ implant [VUO99].

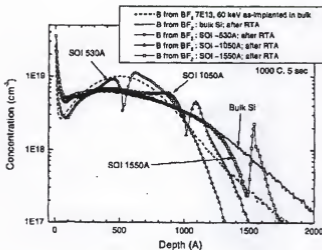


Figure 2-43. SIMS profiles of B from BF_3 implanted at 60 keV, $7 \times 10^{13} \text{ cm}^{-2}$ and annealed at 1000°C for 5 sec in nitrogen. Surface Si thickness used were 530 Å, 1050 Å, and 1550 Å [PAR99].

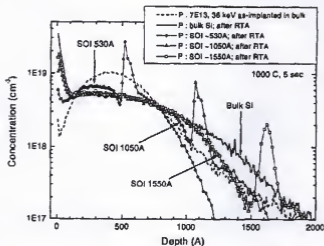


Figure 2-44. SIMS profiles of P implanted at 36 keV, $7 \times 10^{13} \text{ cm}^{-2}$ and annealed at 1000°C for 5 sec in nitrogen. Surface Si thickness used were 530 Å, 1050 Å, and 1550 Å [PAR99].

CHAPTER 3 EXPERIMENTAL METHODOLOGY

This chapter discusses the experimental design of the studies conducted in this dissertation. Details of analytical and simulation techniques used to study the proposed phenomena are discussed. Capabilities and limitations are enunciated as they relate to the particular technique.

3.1 Design of Experiments

The present experiments can be divided into three main categories. The first category was aimed at understanding self-interstitial interactions with the surface Si/BOX interface after ion implantation. These studies involved observing extended defect evolution during annealing and subsequently modeling the behavior. Extraction of the recombination velocity of interstitials yields the relative efficiency of the interface to absorb the interstitials from the extended defects. The second category focused on the physics of electrical activation and segregation of boron in SOI. In these studies, boron interstitial cluster (BIC) formation was monitored and its relationship to segregation evaluated. In each case, the kinetics of the process was investigated under a variety of implant and SOI material conditions. This provided insight into the physical mechanisms that stimulated an observance in the experiment. The final category of experimentation was aimed at investigating the viability of the local electrode atom probe (LEAP) for quantifying boron segregation at the surface Si/BOX interface.

3.1.1 Self-Interstitial Experiments

Figure 3-1 describes the methodology behind the self-interstitial experiments.

Appropriately altering the implant dose determines whether or not an implant is amorphizing. This affects the location of the defect layer as mentioned in Chapter 2. Thus, for the same implant energy the damage may be brought closer to the surface Si/BOX interface by using an amorphizing dose, since the defects form below the amorphous-crystalline interface rather than the projected range. Similarly, altering the implant dose within the non-amorphizing regime allows for observance of a particular extended defect. Lower doses can be used to form only $\{311\}$ defects that dissolve rather than unfaulting to form loops.

Implant conditions along with the anticipated defect microstructure for bulk Si materials is shown in Table 3-1. The relative thermal stability of the extended defects decreases with both energy and dose, making it difficult to observe their evolution in a reasonable time frame. For this reason, doses above $1 \times 10^{14} \text{ cm}^{-2}$ were studied. Implant energies were altered for the non-amorphizing implants in order to change the distance of the defect layer from the surface Si/BOX interface. However, the implant energy had to be capped so that the as-implanted Si^+ profile did not significantly overlap the interface resulting in a large loss of interstitials.

Essentially, three experiments were performed and are shown in Fig. 3-2 to 3-4. The first involved non-amorphizing implants at a fixed dose and annealing temperature. Implant energy and surface Si thickness were used as variables to alter the distance of the damage from the surface Si/BOX interface. The evolution of the extended defect microstructure consisting of $\{311\}$ s and dislocation loops was monitored and quantified via TEM. The goal of the second experiment was to isolate the $\{311\}$ defects from the dislocation loops by using a slightly lower dose at moderate implant energies. Thicker surface Si films were used to further prevent as-

implanted loss of interstitials to the BOX. Also, anneal temperature was varied to determine if the barrier to {311} dissolution is affected by the proximity to the interface. Different SOI substrates (SIMOX and SOITEC) were also used to determine if the manufacturing method alters the ability of the interface to interact with interstitials. Here, the two different types were thinned to the same surface Si and BOX thickness. Finally, the third experiment was aimed at investigating the effect of the interface on end-of-range (EOR) loop evolution. A single implant energy and dose was used, with the implant energy being low enough to prevent complete amorphization of the surface Si layer. As with the second experiment, the kinetics of the process were studied to determine the barrier for dissolution of the loops.

Modeling of the evolution of {311} defects was performed using the Florida Object Oriented Process Simulator (FLOOPS). The models of Law and Jones [LAW00] and Avci et al., [AVC04] were modified to predict the evolution for the case of SOI. The recombination velocity of interstitials was extracted as a function of implant energy and surface Si thickness.

3.1.2 Boron Activation Experiments

The second main class of experiments involved investigating the BIC formation process and its relation to boron segregation in SOI. This required coupling between a number of analytical techniques to determine the electrical, structural, and compositional characteristics. Table 3-2 shows the insight to be gained from the particular analytical technique with regards to boron activation and segregation. The first experiment was conducted to determine the role of the boron profile truncation at the surface Si/BOX interface on the BIC formation process. Similar to the self-interstitial experiments, implants were performed at varying energies and surface Si thickness at a constant dose of $3 \times 10^{14} \text{ cm}^{-2}$. Isothermal and isochronal anneals were performed and the fraction of active boron monitored using Hall Effect. SIMS was used for

compositional analysis, while TEM and HRXRD provided structural information. The second experiment was aimed at determining the concentration dependence of BIC formation, as well as the kinetics of the process. The implant energy was fixed and the dose altered from 3×10^{14} cm⁻² to 1×10^{15} cm⁻². Anneals were performed at a variety of temperatures and times based on previous experiments by Lilak [LIL01] and Mokheri [MOK02] that determined the activation energies for electrical activation of boron in bulk Si under similar conditions. Once again, analysis was performed using Hall Effect to calculate the fraction of active boron. The boron experiments are outlined in Figs. 3-5 and 3-6.

3.2 Analytical and Simulation Techniques

A variety of analytical and simulation techniques were used in the experiments and these are now discussed. For each technique, a brief description of the operating principles is given, as well as how it was applied to the current investigations.

3.2.1 Transmission Electron Microscopy (TEM)

Perhaps the most versatile of all conventional microscopy techniques, TEM is able to provide a wealth of information on the internal structure of materials. These include crystal structure and symmetry, lattice spacing, strain, chemical composition, defect analysis, and surface/interface topology, just to name a few. In TEM, a thin foil is irradiated with electrons of sufficient energy to be transmitted, typically in the range of 100 – 400 kV. As the beam passes thru a crystalline specimen, the electrons are scattered in a variety of directions. Constructive interference of these scattered electrons off specific crystallographic planes creates an electron diffraction spot pattern. The appearance of this pattern is determined by the structure factor, specimen orientation relative to the beam direction, and the lattice spacing. Imaging using these diffracted beams, referred to as dark field (DF) imaging, allows for viewing along specific

crystallographic directions. Generally, this results in excellent contrast relative to imaging with the direct transmitted beam in bright field (BF) mode.

Common plan-view (PTM) sample preparation of single crystal Si substrates consists of drilling a 3 mm disk, mechanically thinning to $\sim 100 - 200 \mu\text{m}$, then etching using a solution of $\text{HNO}_3:\text{HF}$ (3:1). Drilling can be done using a mechanical drill press with a diamond slurry or ultrasonic disk cutter with a silicon carbide slurry. Thinning of the 3 mm disk is done by mounting the Si surface to a rigid structure using a thermoplastic polymer and then polishing from the backside of the disk using an alumina slurry or SiC paper. Etching is performed from the backside of the thinned disk and the Si surface must be protected from the acid by covering with paraffin wax. The nitric acid serves to oxidize the Si to form SiO_2 , which can then be readily etched with HF according to the reactions shown below.



The solution continues to etch the silicon until a hole is produced with very thin areas around the perimeter. The samples are then placed in heptane in order to dissolve the paraffin wax before imaging.

For imaging of extended defects in (001) Si, a $\langle 220 \rangle$ diffracted beam or g_{220} is typically selected. This is done by aligning the g_{220} beam in DF mode with the direct beam in BF mode. A second step involves tilting slightly off the $\langle 001 \rangle$ zone axis and aligning the deficit and excess $\langle 220 \rangle$ kirkuchi lines with the beam direction and g_{220} , respectively in BF, coupled with aligning the lines along the g_{220} and $2g$ in DF. This is followed by shifting the kirkuchi lines slightly off the g_{220} and $2g$ to excite the $3g$ beam to its intersection with the Ewald sphere. The g_{220} is not precisely at the Bragg reflection, rather scattering from the $3g$ allows for the excellent

contrast around the strain field of the defects. This is referred to as weak beam dark field (WBDF) imaging under $g(3g)$ conditions and is illustrated in Fig. 3-7 [WIL96]. A high diffraction intensity occurs close to the dislocation core because, only there are the planes bent back to the Bragg condition.

The major drawback of conventional TEM is that it often requires tedious sample preparation that can take several hours. It is also difficult to image defects with a size less than 50 Å, since they may not sufficiently scatter the electron beam. TEM is a destructive testing technique due to the sample preparation, so samples are not usable after analysis. Despite these disadvantages, the information gained often is unattainable by any other single technique.

3.2.2 Hall Effect

Hall effect is used to describe the motion of charge carriers within a conductive material, as a result of applied electric and magnetic fields. It was first described by Hall [HAL79] using a gold foil specimen and is now routinely used to characterize the activation of dopants in semiconductors. It essentially shows that when a magnetic and electric field are applied perpendicular to each other, another electric field is setup within the conductor that is perpendicular to the two applied fields. The direction of the current of the induced field identifies the type of charge carrier. A van der Pauw [PAU58] geometry, consisting of a number of shapes, is typically used, but is not a prerequisite for doing Hall experiments. The most common shapes include a circle, cloverleaf, square, and bridge-shape.

Figure 3-8 illustrates the Hall effect for a sample uniformly doped to be p-type. The applied electric field is in the x-direction and magnetic field in the z-direction. The current produced by the electric field is given as

$$I = qApv_x = qwdpv_x \quad (3.3)$$

where q is the magnitude of the electron charge (1.6×10^{-19} C), A the cross-sectional area of the specimen, p the hole concentration, and v_x the velocity of the charge carriers. The voltage along the x -direction is then given by

$$V_p = \frac{\rho s I}{A} \quad (3.4)$$

where ρ is the resistivity. This produces a drift of the holes in the $(-)y$ -direction. The Lorentz force exerted on the holes is given by the expression

$$\vec{F} = q(\vec{E} + \vec{v} \times \vec{B}) \quad (3.5)$$

where q is the magnitude of the electron charge, \vec{E} the applied electric field, \vec{v} the drift velocity vector, and \vec{B} the magnetic field vector. Combination of Eq. 3.3 and 3.5 yields the induced electric field in the y -direction as

$$E_y = B v_x = \frac{BI}{qAp} \quad (3.6)$$

which results in the Hall voltage

$$\int_0^{V_H} dV = V_H = - \int_w^0 E_y dy = - \int_w^0 \frac{BI}{qwdp} dy = \frac{BI}{qt\rho} \quad (3.7)$$

where t is the wafer thickness [SCH98]. Another useful quantity is the Hall coefficient and is given as

$$R_H = \frac{1}{qp} = \frac{dV_H}{BI} \quad (3.8)$$

Ion implanted layers typically result in a non-uniform distribution of the carrier concentration. The actual measurement given by Hall effect is actually an average value for mobility, carrier density, and resistivity. For spatially varying values more involved equations are needed

$$R_{HS} = \frac{\int_0^d p(x) \mu_p^2(x) dx}{q \left(\int_0^d p(x) \mu_p(x) dx \right)^2} \quad (3.9)$$

$$\rho_s = \frac{1}{q \int_0^d p(x) \mu_p(x) dx} \quad (3.10)$$

$$\langle \mu_H \rangle = \frac{\int_0^d p(x) \mu_p^2(x) dx}{\int_0^d p(x) \mu_p(x) dx} \quad (3.11)$$

Resistivity and mobility profiles can be achieved by removing layers of the specimen and making Hall measurements as a function of thickness.

A final consideration when performing Hall measurements is to include scattering factors. This is due to carrier scattering around ionized impurities, as well as a result of lattice vibrations. Sasaki et al., determined scattering factors in the concentration range from 10^{17} to $3 \times 10^{20} \text{ cm}^{-3}$ for p-type material [SAS88]. They found it to vary with hole concentration with a maximum value of 0.8 at $5 \times 10^{17} \text{ cm}^{-3}$ and decreased to 0.7 above $5 \times 10^{18} \text{ cm}^{-3}$.

In the current investigations Hall effect was used to determine the resistivity, mobility, and active dose of B in SOI and bulk Si. A square van der Pauw structure was fabricated using a dicing saw or via scribing. Prior to applying electrical contacts the sample surface was etched using a buffered oxide etch (6:1) to remove any native and/or cap oxide. An ohmic contact between a metal and Si requires the work function of the metal to be greater than that of Si ($\phi = 3.6$) [HUM01]. Indium meets this requirement ($\phi = 4.12$) and was used for making contact from the electrodes to the sample surface.

3.2.3 Four-Point Probe

The method of four-point probe is among the simplest, but most popular for determining the resistivity of semiconductors [SCH98]. This apparatus consists of 4 collinear probes spaced an equidistance apart. A current is passed across the outer probes, while the two inner probes measure the voltage drop across the sample. The resistivity is related to the mobility and concentration of charge carriers according to

$$\rho = \frac{1}{q\mu_n n + q\mu_p p} \quad (3.12)$$

where n and p denote the particular charge carrier concentration. For uniform probe spacings,

$$\rho = 2\pi s \frac{V}{I} \quad (3.13)$$

where s is the probe spacing. In very thin samples, where the thickness of the conducting layer is thin compared to the probe spacing (e.g. implanted layers) the resistivity becomes

$$\rho = \frac{\pi}{\ln(2)} \frac{V}{I} = 4.532 \frac{V}{I} x_j \quad (3.14)$$

where x_j is the junction depth. Most values are typically given as a sheet resistance, or average resistance over an arbitrary area, given as

$$R_s = \frac{\rho}{x_j} = \frac{\pi}{\ln(2)} \frac{V}{I} = 4.532 \frac{V}{I} \quad (3.15)$$

with units of ohms/square [PLU00].

Four-point probe was used mainly to confirm Hall effect measurements of resistivity in the current studies. Due to the versatility of Hall effect in providing a greater number of quantities, four-point probe measurements were relatively few.

3.2.4 Secondary Ion Mass Spectrometry (SIMS)

SIMS uses a narrow, monoenergetic beam of primary ions to impinge on a surface; this leads to removal or sputtering of surface atoms, so long as the primary ion energy is sufficiently high. The sputtered atoms are referred to as secondary ions and contain the chemical information of the sample. A mass spectrometer is used to accelerate and then separate the secondary ions according to their mass-to-charge ratio. Comparison with standards allows the secondary ion counts to be converted to concentration. A profilometer is used to measure the sputtered crater depth *ex-situ*, allowing for compositional depth profiles to be produced [BRU92].

Among established analytical techniques, SIMS provides the best chemical resolution for trace impurities in the range of parts per billion. Dynamic SIMS is the common variant for producing concentration profiles, while static SIMS uses lower ion fluences to increase surface sensitivity [BRU92]. The primary advantage of SIMS is that it can detect all elements from H to U, as well as all isotopes. Others include the ability to provide composition images, limited sample preparation, excellent vertical resolution, and very low detection limits. The disadvantages are that the process is destructive, need for standards, and generally poor lateral resolution. Unfortunately, SIMS is notoriously poor at resolving compositions near interfaces, as in the case of SOI. This is a result of differences in the sputter rate between two matrices, as well as differences in the secondary ion yield of the element in the particular matrix material [BRU92].

Analysis of B in Si is done using an O^+ primary beam because it enhances the secondary ion yield. Care must also be exercised when profiling B in SiO_2 because the secondary yield once again increases due to the extra oxygen atoms. This creates a problem for profiling SOI

materials when the surface Si/BOX interface is reached. These problems were somewhat overcome in these studies by using an acute incidence angle and low primary beam energy. This increased the resolution around the interface and provided better vertical resolution.

3.2.5 High Resolution X-Ray Diffraction (HRXRD)

The most precise determination of lattice parameters in bulk and thin film materials can be done using XRD. So what is the difference between conventional XRD and HRXRD? Although, there is no clear, unambiguous definition of HRXRD it could be described as the analysis of crystals, both thin film and bulk, at resolutions unattainable using a common diffractometer. This requires an excellent x-ray source, primary optics, goniometer, and secondary optics, such as those shown in Fig. 3-9 for the Philips X'Pert system. This system allows for a number of applications depending on the optics settings. A 6-axis goniometer is used to tilt and rotate in three dimensions. Phase analysis, texture analysis, rocking curves, space maps, reflectivity, and pole figures, can all be generated with the X'Pert diffractometer. In these studies, high resolution rocking curves were performed for analyzing strain in ion implanted SOI and bulk materials.

Rocking curve analysis is useful for measuring minute changes in lattice parameter, Δa , due to strain. This is done by rocking the sample about a particular Bragg angle, ω , while rotating the detector relative to the source, an angle described as 2θ . This allows the detection of satellite peaks close to, but not precisely at the Bragg angle. The strain between a satellite peak and substrate peak at the Bragg angle is given as

$$\frac{\Delta a}{a} = -\Delta\theta \tan\theta, \quad (3.16)$$

where Δa is the difference in lattice spacing between the peaks, and $\Delta\theta$ the difference in diffraction angles ($\theta_f - \theta_s$) between the film and substrate. [TUK88] The composition of substitutional impurities in a Si film may then be determined using Vegard's law according to

$$a_s = a_{Si} - \beta C_A \quad (3.17)$$

where a_{Si} is the unstrained lattice parameter, β the strain rate coefficient, and C_A the concentration of the impurity. The strain rate coefficient is given as

$$\beta = \left(\frac{1+\nu}{1-\nu} \right) \frac{a_A - a_{Si}}{n_A} \quad (3.18)$$

where ν is Poisson's ratio for Si (0.278), a_A the lattice parameter of the impurity, and n_A the atomic density of Si ($5 \times 10^{22} \text{ cm}^{-3}$) [TAK02].

The primary and secondary optics for rocking curve analysis using the X'Pert system are shown in Fig. 3-10. The hybrid mirror is used because it provides the best resolution of all the optics. It has a monochromator that filters the beam so that only $K\alpha_1$ radiation is used. Single crystals often diffract a very high intensity because of their perfection, so a beam attenuator must be used in some cases to prevent destruction of the detector. The attenuator is always present when aligning the sample, but is set to engage at given intensity when running a scan. The secondary optics consist of a triple axis and rocking curve attachment. The detector sits in one of two positions available in the attachment. The position shown in Fig. 3-10 is for medium resolution and contains a 6 mm aperture, corresponding to a 1° acceptance angle. In the other position, a channel cut analyzer Ge crystal, with an acceptance angle of 12 arc seconds, is used to convert the system to the triple axis mode. The diffracted beam goes through three (022) reflections before it impinges on the detector.

For ion implanted Si, a number of artifacts can be distinguished using rocking curve analysis. Those appearing to the right of the bulk Bragg angle, or unstrained lattice parameter,

represent tensile strain in the lattice, while those to the left are a result of compressive strain. Vacancies within the lattice cause the local Si-Si bonds to stretch creating a tensile stress. Interstitials create a compressive stress by making the bond lengths of nearby atoms shorter. In the case of B, it may reside in both interstitial and substitutional form within the Si lattice. Substitutional B results in tensile strain because it is a smaller atom (atomic radius = 0.097 nm) than Si (atomic radius = 0.117 nm).

3.2.6 UT-Marlowe

The Monte Carlo simulator UT-Marlowe is used to simulate the trajectory of ions into crystalline and amorphous materials. It is able to account for a variety of implant physical processes including channeling, dechanneling, damage production, oxide thickness, as well as tilt and twist angles. This program was used to simulate all the Si⁺ and B⁺ ion profiles, as well as the damage profiles used in these studies. Two main damage models are currently incorporated into UT-Marlowe: the kinectic accumulation damage model (KADM) and Kinchin-Pease damage model [MAR50].

The KADM model divides the damage process into two parts. The first involves simulating the damage cascade that takes place on the order of picoseconds. The second part involves the interaction of the defects produced during the first phase; this takes place on the time scale of 0.1 milliseconds, or so. The goal is then to be able to feed the damage profiles into a diffusion simulator (e.g., FLOOPS) for predicting the motion of the defects and implanted species. The following assumptions are made in this model: implantation is performed near room temperature, the only mobile species are single point defects, vacancies migrate about regular lattice sites, interstitials diffuse through a tetrahedral-hexagonal path, and every mobile defect has the opportunity to interact with nearest neighbor atoms at each time interval.

Migration energies for neutral point defects are 0.45 and 0.55 for a vacancy and interstitial, respectively [MAR50].

A somewhat simpler model is the Kinchin-Pease. It accounts for the processes of defect production, accumulation, dechanneling, and amorphization. Unfortunately, this model fails to accurately predict profiles at high energies where the energy of the primary ions is not deposited locally. It also assumes the vacancy concentration to be equal to the interstitial concentration, which is not necessarily the case [MAR50].

3.2.7 Florida Object Oriented Process Simulator (FLOOPS)

A number of semiconductor process simulators are currently available including, T-SUPREM IV, DADOS, and FLOOPS [FLO01]. These programs allow for simulation of the entire microelectronic fabrication process on a UNIX or LINUX platform. In conjunction with the Florida object oriented device simulator (FLOODS), it is also able to predict device characteristics after the fabrication process. FLOOPS uses tool command language (Tcl) for issuing the commands that are fed into the simulator. For the present studies, FLOOPS was used to simulate the {311} defect evolution using the models of Law [LAW00] and Avci [AVC02].

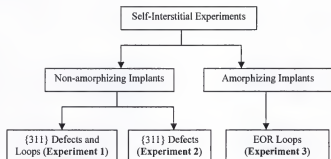


Figure 3-1. Logic behind design of self-interstitial experiments. Implants are designated as amorphizing or non-amorphizing. Appropriately altering implant energy and dose allows observance of a particular extended defect.

Table 3-1. Implant conditions and anticipated defect microstructures of interest in current self-interstitial experiments. Shaded boxes indicate implant conditions that were actually studied. Note: microstructures are only valid for bulk Si.

Energy (keV)	Dose (cm ⁻²)				
	5 00E+13	1 00E+14	2 00E+14	3 00E+14	1 00E+15
5	No Defects	Dot Defects	Zig-zag {311}s & Loops	Zig-zag {311}s & Loops	{311}s & EOR Loops
10	No Defects	{311}s	{311}s & Loops	{311}s & Loops	{311}s & EOR Loops
20	No Defects	{311}s	{311}s & Loops	{311}s & Loops	{311}s & EOR Loops
40	{311}s	{311}s	{311}s & Loops	{311}s & Loops	{311}s & EOR Loops
50	{311}s	{311}s	{311}s & Loops	{311}s & Loops	{311}s & EOR Loops

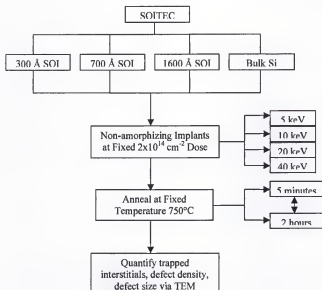


Figure 3-2. Experimental methodology invoked in first self-interstitial study of $\{311\}$ defects and dislocation loops for non-amorphizing implants. Samples were implanted at a fixed dose with energies varying from 5 to 40 keV. Anneals were performed at 750°C for times ranging from 5 minutes to 2 hours. Note: all substrates were fabricated using the SOITEC method.

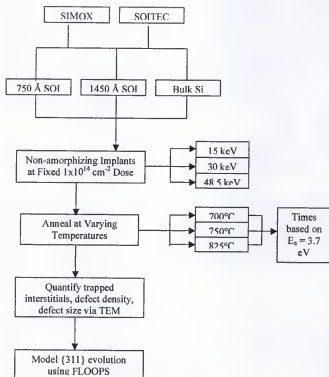


Figure 3-3. Design of experiment 2 for determining kinetics of {311} defect evolution in SIMOX and SOITEC substrates.

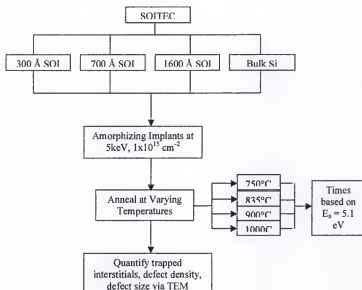


Figure 3-4. Experiment 3 methodology for determining effect of surface Si/BOX interface on EOR dislocation loop formation.

Table 3-2. Insight gained from analytical techniques with regards to the BIC evolutionary process and boron segregation in SOI.

SIMS	TEM	Hall Effect	Four Point Probe	XRD
Boron Concentration	Defect Microstructure	Active Dose	Sheet Resistance	Strain
Clustered Dose	Qualitative w.r.t. BICs	Clustered Dose		Active Dose
Segregated Dose		Sheet Resistance		

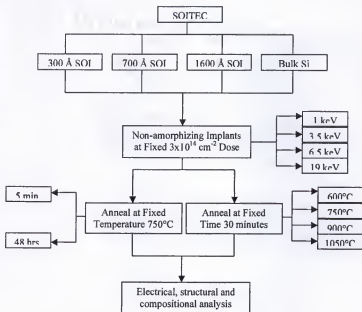


Figure 3-5. Experimental design for first study of boron activation in SOI.

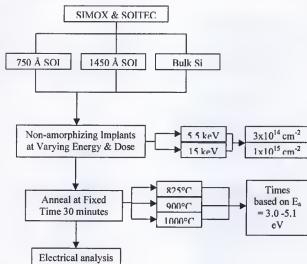


Figure 3-6. Design of second experiment for investigating kinetics of BIC dissolution in SOI and bulk Si.

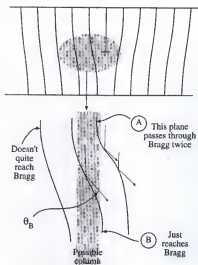


Figure 3-7. Principle behind weak beam dark field imaging in TEM for an edge dislocation. High intensity occurs close to dislocation core because planes are bent back to Bragg condition. From [WIL96]

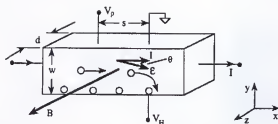


Figure 3-8. Illustration of Hall effect occurring in a p-type specimen. From [SCH98].

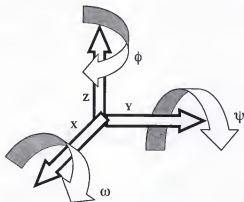
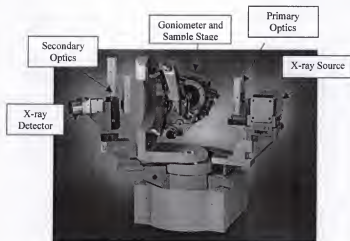
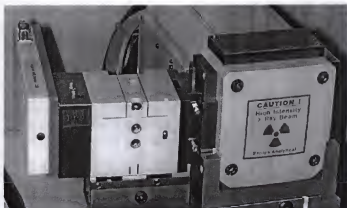
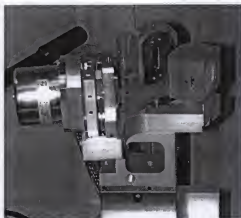


Figure 3-9. Primary components of Philips X'Pert System with 6-axis goniometer. From [PAN04].



(a)



(b)

Figure 3-10. Optics setup for rocking curve analysis using Philips X'Pert system. (a) Primary optics – hybrid mirror and (b) secondary optics – triple axis detector. From [LIN04].

CHAPTER 4 SELF-INTERSTITIAL EXPERIMENTS IN SOI

4.1 Introduction

This chapter describes the self-interstitial experiments that were performed in SOI. The first set of experiments was for non-amorphizing implant conditions. These centered around the evolution of $\{311\}$ defects and dislocation loops as a function of distance from the surface Si/BOX interface. Amorphizing implants compose the other set of experiments, which focused on EOR loop and OSF evolution.

4.2 Non-Amorphizing Implants

Interface effects on $\{311\}$ evolution and their kinetics are described in the first two experiments of this section. Dislocation loop evolution is discussed in the final experiment.

4.2.1 Interface Effects on $\{311\}$ Defect Evolution

While quality of Separation by Implantation of Oxygen (SIMOX) material has made great strides since its conception [IZU78], there is concern over differences in quality of a synthetic BOX (e.g., SIMOX) versus a grown thermal BOX (e.g., SOITEC) [CON96]. Due to the large oxygen doses used for BOX formation in the SIMOX process, residual oxygen is expected to be left in the surface silicon layer. The excess oxygen could theoretically serve as traps for interstitials, thus affecting dopant diffusion and interstitial recombination. The current study investigates the dependence of point defect populations on the type of surface silicon/BOX interface (e.g., SIMOX or SOITEC), as well as proximity to the interface. This is accomplished by monitoring trapped interstitials within extended defects (e.g., $\{311\}$ defects and dislocation

loops). The study focuses specifically on {311} defect formation, rather than both {311} and dislocation loop formation.

4.2.1.1 Experimental

In the experiment, Czochralski, SIMOX and SOITEC wafers (p-type, 200 mm, {001}) having a BOX thickness of 1300 Å were used. Thinning of the surface silicon layer from 1450 Å down to 750 Å with a thickness variation of ± 50 Å was done for selected SOI wafers using oxidation then etching with dilute hydrofluoric acid. $^{28}\text{Si}^+$ implants were performed at a non-amorphizing dose of $1 \times 10^{14} \text{ cm}^{-2}$ with a 7° tilt and 22° twist angle. Implant energies were performed at 15, 30 and 48.5 keV for the 1450 Å and bulk specimens. The 750 Å specimens were implanted at 15 and 30 keV, but not 48.5 keV due to concerns over dose loss to the BOX. Thermal processing was performed in a Thermolyne quartz tube furnace under a nitrogen ambient at 750°C for times ranging from 5 minutes to 1 hour. Plan-view transmission electron microscopy (PTM) SOI specimens were prepared in the following sequence: backside grinding using 15 μm alumina slurry, backside etching using $\text{HNO}_3:\text{HF}$ 3:1, buffered oxide etching (6:1). The buffered oxide etching step assisted with removal of the BOX, thus it was not required for fabrication of bulk PTM specimens. A JEOL 200CX TEM with an accelerating voltage of 200 kV and emission current of 125 μA was used to image the PTM specimens. Weak beam dark field (WBDF) images were taken under $g(3g)$ conditions using a g_{220} diffracted beam. Quantitative TEM (QTEM) was used to measure the concentration of trapped interstitials, defect density and defect size.

4.2.1.2 Results

Figure 4-1 shows UT-Marlowe [MAR50] simulations of the ion profiles for the Si⁺ implants. The projected range for the 15, 30, and 48.5 keV implants was measured to be 180 Å, 330 Å, and 550 Å, respectively. All the implants punch thru into the BOX for the SOI specimens, but is more severe for the 750 Å SOI. Integration of the profile confined to the surface silicon layer allows for the calculation of the initial dose loss of Si⁺ ions to the BOX (Figure 4-2). The 750 Å SOI loses approximately 3% of the implanted dose at 15 keV, 10% at 30 keV, and 30% at 48.5 keV. The dose loss for the 1450 Å SOI was approximately 1% at 30 keV and 3% at 48.5 keV.

Figure 4-3 shows WBDF images for the 15 keV specimens after annealing for 5 minutes and 15 minutes. There does not appear to be a difference between SOITEC and SIMOX for either the 750 Å or 1450 Å specimens. A high density of small dot defects appear at short times, which evolve into {311} defects in the 1450 Å and bulk as annealing proceeds. However, the 750 Å SOI appears to avoid growth of {311} defects above a certain length. Rather, the dot defects appear to be much more stable in the 750 Å SOI than {311} defects. Figure 4-4 shows the concentration of trapped interstitials in all extended defects. A slight enhancement in the decay of the trapped interstitial population occurs in the 750 Å SOI at longer times. However, as indicated above no differences can be distinguished between SOITEC and SIMOX.

Figure 4-5 shows PTEM images illustrating the extended defect evolution for the 30 keV, $1 \times 10^{14} \text{ cm}^{-2}$ SIMOX and bulk specimens after annealing 5 minutes and 15 minutes. Once again, the microstructure appears similar between the SIMOX and bulk after annealing for five minutes. However, after 15 minutes the dot defects have evolved into {311} defects in the bulk,

but not in the 750 Å SIMOX. The QTEM trapped interstitial data for the 30 keV specimens is shown in Fig. 4-6. Despite a 10% initial dose loss in the 750 Å SOI, no decrease in the initial trapped interstitial population can be seen. As annealing proceeds, a significant enhancement in the decay rate of the trapped interstitial population in SOI is observed. This effect is further illustrated in Fig. 4-7 by quantifying the concentration of trapped interstitials within {311} defects only. The 750 Å SIMOX and SOITEC decay to the TEM detection limit of $\sim 1 \times 10^{11} \text{ cm}^{-2}$ after annealing for 15 minutes. A decrease in trapped interstitials in {311}s also appears in the 1450 Å specimens, but is not as dramatic as in the 750 Å. Figure 4-8 shows the average size of {311} defects in SOI and bulk. Growth of {311} defects appears in the 1450 Å SOI and bulk, but shrinkage is observed in the 750 Å SOI. On the contrary, the 750 Å SOI tends to favor dislocation loop formation over {311} defects, as seen in the micrographs in Fig. 4-5.

Figure 4-9 shows the PTEM micrographs for the 1450 Å SOI and bulk specimens implanted at 48.5 keV. As before, dot defects appear at early times, which then evolve into {311} defects in the bulk. However, a clear reduction in the {311} defect size and density can be seen in the 1450 Å SIMOX and SOITEC. The QTEM data appears in Figs. 4-10 and 4-11. An enhancement in the decay rate is observed for the 1450 Å SOI despite only a 3% dose loss from the implant. This enhancement is once again attributed to a reduction in the {311} population, shown in Fig. 4-11. Figure 4-12 shows the average size of the {311} defects in the 1450 Å SOI and bulk. The {311}s appear to reach a critical size of approximately 150 Å in the 1450 Å SOI, after which they begin to dissolve. Growth of the {311} defects continues in the bulk silicon up to an average size above 300 Å.

4.2.1.3 Discussion

Comparison of the decay of the trapped interstitial population between SOI and bulk silicon agrees well with previous experiments [SAA02a, SAA02b]. For ion and interstitial profiles confined to the surface silicon layer, little difference is seen between SOI and bulk. However, no measurable decrease in the initial trapped interstitial concentration is observed in the 750 Å SOI despite a 10% dose loss at 30 keV. A reduction in the initial trapped interstitial concentration has been previously observed for dose losses as low as 6% [SAA02a, SAA02b]. The previous experiments, discussed later in this chapter, also showed that an enhancement in the decay rate was not observed without more than a 13% dose loss. The instability of the {311} defect compared to the dislocation loop is the likely cause of these observations. This is a result of the lower dose used in the current experiment. A $1 \times 10^{14} \text{ cm}^{-2} \text{ Si}^+$ dose in the energy range of 20-80 keV tends to form {311} defects, which mostly dissolve after approximately 1 – 1.5 hours at 750 °C. The $2 \times 10^{14} \text{ cm}^{-2} \text{ Si}^+$ dose used in the previous experiments forms {311} defects, but these tend to unfault to form stable dislocation loops. The enhanced decay rate in the trapped interstitial concentration in SOI is a result of the enhanced dissolution of {311} defects in SOI. We discuss the affects of dose loss/implant energy, SOI thickness, and interface roughness below.

The most interesting observation from the data presented is that {311} defects do not go through the same growth process in SOI as in bulk silicon. This occurs despite minimal dose loss of interstitials to the buried oxide. Clearly, growth of {311} defects is observed in bulk silicon. However, the amount of elongation of {311} defects in SOI depends strongly on the surface silicon thickness. The average size of the {311} defects increases as the surface silicon layer thickness is increased. This leads to the following propositions below.

The $\{311\}$ defect is known to reside along $\{311\}$ planes and elongate in $\langle 110 \rangle$ directions [EAG94]. For the $\langle 110 \rangle$ family of directions, 6 directions are inclined to the surface for a $\{001\}$ oriented silicon crystal. The $\{311\}$ defects are prevented from elongating into the buried oxide, since it is amorphous. Thus, the $\{311\}$ defects which elongate inclined to the surface can only grow to a certain length before they are pinned by the BOX. This would depend on the implant energy and the surface silicon thickness. The higher the implant energy or the thinner the surface silicon layer, the smaller the size of $\{311\}$ defects observed. This theory supports the results that have been presented.

There is one problem with the proposed theory; it does not account for $\{311\}$ defects that elongate in the plane of the surface silicon layer. Those $\{311\}$ defects are expected to still elongate to the same length as those in bulk silicon. However, this is not observed in the PTM micrographs. This may indicate that $\{311\}$ defects simply are not as stable in SOI as in bulk silicon. Future experiments will set out to investigate the role of stress on $\{311\}$ evolution in SOI due to differences in thermal expansion coefficients between silicon and SiO_2 .

The measured "+1" value [GIL91] for the initial trapped interstitial concentration in extended defects was not strongly affected even when the ion profile overlapped the surface Si/BOX interface. However, there is typically a variation of 20% in QTEM measurements of $\{311\}$ defects in Si. Thus, a variation in the "+1" value between SOI and bulk is within the error of the measurements. The expected variation, based on simulation, in the "+1" value as a function of surface Si thickness is shown in Fig. 4-13. This value was obtained by subtracting the vacancy profile from the interstitial profile and integrating over the surface Si thickness. It should be noted that these values ignore outdiffusion of interstitials from the BOX into the surface Si layer. It shows that the "+1" value does not vary significantly until the thickness is

scaled below 450 Å for the 15 keV implant energy. For the 48.5 keV implant energy the "+1" value begins to decrease significantly below a surface Si thickness of 1000 Å. From this, interstitial dose loss can be ruled out as the primary reason for the instability of {311}s in SOI; at least for the surface Si thickness and implant energies used in this study. It is pointed out that the easiest way to lose interstitials to the BOX is by increasing the implant energy, thus truncating more of the ion/interstitial profiles. Interstitial dose loss has been attributed to the observance of reduced dislocation loop size in SOI [SAA02a].

Another mechanism that may affect the interstitial decay from {311}s is roughness of the surface Si/BOX interface. This has been suggested previously [SAA02a]. As the surface Si/BOX interface sees more of the dose, the roughness of the interface is likely to increase. This could increase the dangling bond and kink site densities allowing more interstitials to recombine. However, if this is the primary mechanism it is much stronger than observed in the previous experiment [SAA02a].

One final discussion with regards to the differences between SIMOX and SOITEC interfaces is necessary. There is no distinguishable difference in the ability of the surface silicon/BOX interface of either material to allow interstitials to recombine or diffuse into the BOX. It seems obvious that the interfaces are more similar than may have been expected. A SOITEC buried oxide is a grown, thermal oxide, whereas a SIMOX buried oxide is a synthetic oxide. However, developments in SIMOX technology, such as the internal thermal oxidation (ITOX) process used to produce the wafers in this experiment, may yield an interface similar to a grown thermal oxide. If this is the case, then the results certainly make sense.

4.2.1.4 Conclusions

The effect of interface type (e.g. SIMOX or SOITEC) and surface silicon thickness on {311} defect evolution has been investigated via QTEM. We show that both SIMOX and SOITEC interfaces allow for similar defect evolution and recombination of trapped interstitials. A significant difference in {311} nucleation and growth in SOI is observed. Dose loss, SOI thickness, and interface roughness are proposed as mechanisms by which the {311} stability is reduced in SOI. {311} defects in SOI are not as stable and appear to favor formation of dislocation loops as the surface Si layer is thinned. The enhanced dissolution of {311}s in SOI are believed to be the reason for the enhancement in the decay of the trapped interstitial population for low dose losses.

4.2.2 Kinetics of {311} Defect Evolution in SOI

This study set out to investigate the reaction kinetics of {311} defect dissolution in SOI, and then compare it to bulk silicon.

4.2.2.1 Experimental

Separation by Implantation of Oxygen (SIMOX) and bonded (SOITEC) wafers were used, along with Czochralski wafers, in the experiment. All wafers were p-type, 200 mm, {001}, with a BOX thickness of 1300 Å. Some of the 1450 Å SOI wafers were thinned to 750 Å using oxidation and etching in dilute hydrofluoric acid (10:1). Ion implantation was done at angles of 7° tilt and 22° twist; implants consisted of $^{28}\text{Si}^+$ ions at a non-amorphizing dose of $1 \times 10^{14} \text{ cm}^{-2}$. The implant energies were 15 keV, 30 keV, and 48.5 keV for the 1450 Å SOI and bulk silicon. For the 750 Å SOI only the 15 keV and 30 keV energies were performed in order to prevent substantial dose loss to the BOX. Furnace anneals were performed at 700 °C and 750 °C in a Thermolyne quartz tube furnace with a nitrogen ambient. An AG Associates rapid thermal annealing (RTA) system was used in order to provide controllability for shorter anneals

at 825 °C. The methodology for determining the anneal times is described in the following paragraph. Plan-view transmission electron microscopy (PTM) SOI specimens were fabricated by mechanical grinding with 15 µm alumina, followed by etching using HNO₃:HF 3:1. Buffered oxide etching (6:1) was used to help remove the BOX from the SOI specimens. A JEOL 200CX TEM operating at accelerating voltage of 200 kV was used for imaging under weak beam dark field g(3g) conditions using a g₂₂₀ diffracted beam. Micrographs were taken at 50,000X and then printed at a total magnification of 150,000X so that quantitative TEM (QTEM) could be performed. QTEM was used to measure the trapped interstitial dose, defect size, and defect density.

The trapped interstitial decay for {311} defects varies exponentially with time according to Eq. 2.1 and the time constant can be shown to follow an Arrhenius expression, such as in Eq. 2.2. Anneal times were determined by assuming an activation energy of 3.7 eV [SOL91] for {311} dissolution, corresponding closely with previous studies of enhanced diffusion and extended defect evolution [LIJ99]. Thus, if one determines the time for annealing at a particular temperature an equivalent time can be determined at another temperature by equating the ratio of the activation rates. This allows for observation of similar microstructures at different annealing temperatures, rather than a simple isochronal sequence. For example,

$$t_2 = [t_1/t_2] \times t_1 = [e^{-3.7\text{eV}/kT_1} / e^{-3.7\text{eV}/kT_2}] \times t_1 \quad (4.1)$$

where t_1 is the annealing time at temperature T_1 and t_2 is the unknown time for temperature T_2 . Perhaps the most common temperature for observing {311} defect evolution is 750 °C, since the {311}s do not dissolve too fast or slow. Thus, 750 °C was used as a baseline for determining the equivalent annealing times at 700 °C and 825 °C. Table 4-1 shows equivalent annealing times for 700 °C, 750 °C and 825 °C based on this procedure.

4.2.2.2 Results

Tables 4-2 and 4-3 show the as-implanted stopping range statistics for the Si⁺ implants obtained from UT-Marlowe [MAR50] and SRIM [SR100]. Dose loss due to implant overlap with the buried oxide was calculated by truncating the implant profile obtained from UT-Marlowe at the surface Si/BOX interface and integrating only the ions left in the surface silicon layer. This value was then subtracted from the actual implanted dose of $1 \times 10^{14} \text{ cm}^{-2}$.

Figure 4-14 shows a series of micrographs comparing the defect evolution between 750 Å SIMOX and bulk silicon for the 30 keV implant energy. Upon annealing, this non-amorphizing implant evolves into Type I extended defects consisting of {311} defects and extrinsic dislocation loops. [JON88] At early times, a high density of dot defects appear, which may or may not be small {311} defects. As annealing proceeds, the {311} defects grow and then either dissolve or unfault [LIJ98] to form dislocation loops. The {311} defects are clearly smaller in the 750 Å SIMOX samples than in the bulk Si.

Figures 4-15 – 4-17 show the time dependency of the trapped interstitial dose in {311}s for the 3 implant energies at the three temperatures. In each of the cases, the {311} defects appear to be less stable in the 750 Å SOI compared to the 1450 Å SOI and bulk Si. As the implant energy is increased to 48.5 keV the {311} defects in the 1450 Å SOI appear to be less stable than bulk Si. These phenomena have been discussed in the experiment above. It should be noted that all trapped interstitials are assumed to be in {311} defects at the first time point for each of the three temperatures. The validity of this assumption is discussed below.

{311} defects are metastable in the sense that they can undergo an unfaulting reaction to form a dislocation loop, but a dislocation loop cannot form a {311}. It is believed that {311} defects nucleate from sub-microscopic interstitial clusters (SMICs) [COF00]. Thus, it makes

sense that the small dot defects at early times are more similar to the $\{311\}$ rather than a stable dislocation loop, since they preclude $\{311\}$ formation. The dot defects do not appear to simply skip $\{311\}$ formation and nucleate into stable dislocation loops.

Figure 4-18 shows the plot of the time constant, τ , for $\{311\}$ dissolution versus $1/kT$. Time constants were obtained by fitting the trapped interstitial decay curves in Figures 4-15 - 4-17 with an exponential function of the form in Eq. 2.1. This was done using a least squares fit through the data points. Similarly, fitting the curves in Fig. 4-18 with an exponential yields the activation energy, E_a , according to Eq. 2.2. These values appear in Table 4-4. Standard deviation, σ , was calculated by fitting exponential functions through the maximum and minimum of the error bars in the first and last $1/kT$ value, respectively. The activation energy for $\{311\}$ dissolution in the 750 Å SOI is slightly less than the 1450 Å SOI and bulk Si for the 15 keV and 30 keV implants. However, E_a for the 1450 Å SOI is similar to bulk Si at each of the implant energies. No difference in E_a due to the type of SOI substrate can be seen in the data.

4.2.2.3 Discussion

The data from Figures 4-14 - 4-17 agree with other studies of dislocation loop and $\{311\}$ evolution in SOI discussed elsewhere in this chapter. As the implant energy increases, or the surface silicon thickness decreases, it becomes easier for interstitials to recombine at the surface Si/BOX interface. It has been hypothesized that damage to the interface strongly affects the ability of interstitials to recombine [SAA02a]. Thus, as the implant energy increases more of the incident ions reach the BOX increasing the damage to the interface. Interstitials have a high diffusivity [HUS94] at the temperatures under investigation, so it could be set forth that recombination at the interface is a reaction rate-limited process. In other words, interfacial

recombination is limited by the ability of interstitials to dissociate from the {311} rather than their diffusion to the interface. This goes along with the observations of Li et al., [LJ98] and the model of Law and Jones [LAW00].

The decrease in the activation energy in the 750 Å SOI indicates a reduced barrier for interstitial dissociation from the {311} defect. Whether or not this is the result of interstitial recombination or simply due to a reduction of defect size is unclear. It has been shown that smaller {311}s dissolve faster than larger {311}s [LJ98]. However, a reduction in defect size should not change the activation energy for {311} dissolution. Another process, e.g., recombination, could change the activation energy.

The thermal behavior of {311}s in thick SOI is the same as bulk Si, as long as the implant energy is not sufficiently high. Smaller {311} defects are observed in the 1450 Å SOI at the 48.5 keV implant energy, yet the activation energy is approximately the same as bulk Si. This would also lend support to the interstitial recombination at the surface Si/BOX interface theory, since the smaller defects dissolve faster. However, the defect layer is far enough away from the interface that the activation energy for dissolution is not affected.

It can be theorized that the activation energy will continue to decrease if the surface Si thickness is scaled further. This may result in a nearly athermal behavior of the {311} defect in SOI as the defect layer approaches the surface Si/BOX interface. King et al., found a activation energy of approximately 1.0 eV for defects in the proximity of the surface in bulk Si [KIN03]. A proximity investigation in SOI is difficult due to the large dose losses that occur if the project range of the implant is placed in the vicinity of the surface Si/BOX interface. This could potentially prevent extended defects from even forming in SOI, unless the dose is sufficiently high.

4.2.2.4 Conclusions

The reaction kinetics of {311} defect dissolution in SOI have been studied via quantitative TEM. A reduction in defect size leads to an enhanced decay rate of {311}s in SOI. Thinning of the surface silicon layer results in a decrease in the activation energy of {311} dissolution in SOI. Increasing the implant energy also results in a reduction in the activation energy in 750 Å SOI. It is hypothesized that interstitial recombination at the surface Si/BOX interface is responsible for the reduction in activation energy when the defect layer is within ~500 Å. It is also proposed that the dissolution kinetics will tend towards athermal behavior as the implant damage is placed closer to the interface.

4.2.3 Interface Effects on Dislocation Loop Evolution

The effects of the surface Si/BOX interface on interstitial storage in non-amorphizing loops are described in this experiment.

4.2.3.1 Experimental

Czochralski and UNIBOND® wafers (200 mm, {001}, 14 – 22 Ω cm) having a BOX thickness of 4000 Å were used in the experiment. The surface silicon layer of the SOI wafers was thinned using oxidation and etching from 1600 Å down to 670 – 688 Å and 299 – 305 Å, respectively. The surface Si layer thickness was monitored using a Rudolf dual wavelength ellipsometer. The wafers were then implanted with $^{28}\text{Si}^+$ ions at energies ranging from 5 keV to 40 keV and a constant dose of $2 \times 10^{16} \text{ cm}^{-2}$. The implant conditions did not result in amorphization of any of the materials. Anneals were done in a quartz tube furnace with a nitrogen ambient at 750°C for times ranging from 5 minutes up to 8 hours. Plan-view transmission electron microscopy (PTM) samples were prepared and imaging was done using a JEOL 200CX TEM operating at 200 kV. Images were taken using a g_{220} diffracted beam

under g(3g) weak beam dark field conditions. Finally, quantitative TEM (QTEM) was used to calculate the concentration of trapped interstitials (Si_i) in extended defects.

4.2.3.2 Results

Figure 4-19 shows the interstitial concentration (C_i) profiles simulated using UT-Marlowe. This illustrates that as the implant energy increases and the surface Si thickness decreases, the concentration of interstitials in the BOX increases. Thus, fewer excess interstitials are available to aid in the formation of extended defects within the surface Si layer. Figure 4-20 shows the percent of dose retained in the surface Si layer as a function of implant energy. The 1600 Å SOI essentially receives the same dose as the bulk for all the implants, while the 700 Å SOI loses up to 25% at 40 keV. The 300 Å SOI loses approximately 45% and 80% at 20 and 40 keV, respectively.

Figures 4-21 and 4-22 show the PTEM micrographs and QTEM data for the 5 keV samples. After annealing at 750°C for 15 minutes, a combination of small interstitial clusters and zig-zag $\{311\}$ defects can be seen in the 300Å and bulk. The zig-zag $\{311\}$ defects, which have been observed previously, [AGA97a] coarsen after annealing for 60 minutes. They begin to dissolve, as well as form small dislocation loops after 120 minutes. The dislocation loops appear much smaller in the 300 Å after 120 minutes, but the defect density is also much greater. As a result, the concentration of trapped interstitials in Figure 4-22 is similar for each of the materials. Data for 5 keV, $3 \times 10^{14} \text{ cm}^{-2}$, Si^+ implants from Agarwal et al., [AGA97a] is included for comparison.

The defect evolution for the 10 keV 300 Å SOI and bulk Si is shown in Figure 4-23. At this energy, a larger portion of the dose ($\approx 14\%$) is lost to the BOX compared to 5 keV. Thus, a decrease in the density of extended defects, as well as concentration of trapped interstitials

occurs in the 300 Å SOI. There is also an increase in the size of the dislocation loops in bulk Si as implant energy increases. Close examination of the micrographs reveals the defects dissolve faster in the 300 Å SOI than the bulk. Quantification of the trapped interstitials (Figure 4-24) shows a similar trend. A decrease in the concentration of trapped interstitials, as well as an increase in the dissolution rate occurs in the 300 Å. In addition, the decrease in Si_i is much greater than that predicted from the dose loss. However, the 700 Å, 1600 Å and bulk all behave similarly.

The 20 keV defect evolution for the 700 Å SOI and bulk Si are shown in Figure 4-25. Dislocation loops appear to form from the unfaulting of $\{311\}$ defects and the nucleation of the small interstitial clusters. Extended defects do not form in the 300 Å SOI due to the dose loss to the BOX. There appears to be a decrease in the defect size, as well as defect density in the 700 Å compared to the bulk. This would be expected due to the 6% dose loss at this energy. The concentration of trapped interstitials in Fig. 4-26 shows a similar trend. However, there is a larger decrease in trapped interstitials ($\sim 35\%$) than predicted from the dose loss alone. In contrast, there is not an increase in the dissolution rate in the 700 Å. Overall, there is not a decay in the trapped interstitial concentration due to the stability of the dislocation loops at this energy.

Figure 4-27 shows the defect evolution for the 40 keV 700 Å SOI and bulk Si after annealing at 750°C. Once again, a decrease in the defect size appears obvious in the 700 Å SOI, which could be attributed to the dose loss of 25%. The small dislocation loops in the 700 Å do not appear to coarsen, but rather appear to dissolve. The $\{311\}$ defects begin to unfault and form dislocation loops after 30 minutes in the bulk samples. The dislocation loops are still present after annealing for up to 8 hours. Figure 4-28 shows the QTEM data for the 40 keV

samples. The 700 Å SOI exhibits a decrease in the concentration of trapped interstitials of approximately 95%, which is much larger than the 25% dose loss at 40 keV. There also appears to be an enhancement in the dissolution rate for the 700 Å. Like 20 keV, the 1600 Å SOI behaves similar to the bulk.

4.2.3.3 Discussion

The dissolution behavior for the 5 keV data set compares favorably with that done previously by Agarwal et al. [AGA97a]. The surface Si/BOX interface does not appear to have a strong effect on recombination of trapped interstitials at this energy. This may be expected due to the projected range (100 Å) being furthest from the interface. However, there is a 5% dose loss in the 300 Å SOI, but there is not a detectable decrease in Si_i in Fig. 4-22. There have been a number of theories as to why there is an enhanced dissolution rate for low energy compared to higher energy Si^+ implants [LJM95, SAL00, MOL98]. The presence of a higher supersaturation of excess interstitials may be the reason fewer extended defects are observed. Defects may not be able to trap as many interstitials due to the high supersaturation, creating a large flux into the crystal, rather than the surface being a dominant sink for interstitials [OMR96, KIN03].

At 10 keV, the enhanced dissolution rate and decrease in Si_i in the 300 Å SOI is attributed to recombination at the surface Si/BOX interface. This is because the decrease in Si_i is much larger than the dose loss to the BOX. However, the fact that the other SOI samples behave similar to the bulk indicates that there is not an interface effect in thicker SOI at 10 keV.

For the 20 keV, a large decrease in Si_i for the 700 Å SOI is observed, but there is not an enhancement in the dissolution rate. This indicates that there is a dose loss threshold that must be exceeded before a decrease in Si_i can be quantified. This appears to occur around 6%.

An enhancement in the dissolution rate is observed for the 700 Å SOI at 40 keV. This indicates there is also a threshold for dose loss before an enhancement in the dissolution rate is observed. This threshold is approximately 15% since the 300 Å and 700 Å SOI show enhancement above 15%, but do not below 15%. There may also be a threshold for the formation of extended defects in SOI at the $2 \times 10^{14} \text{ cm}^{-2}$ dose. This is between 30 - 45% since no extended defects formed in the 300 Å at 20 keV (45% dose loss) and the extended defects were very small in the 700 Å at 40 keV (25% dose loss). However, this threshold is expected to vary depending on the implanted dose.

A number of theories have been proposed for the recombination of interstitials at a Si/SiO₂ interface [DUN92, LAW98, LAW91, TSO93]. As an interstitial approaches the Si/SiO₂ interface it may do a number of things: recombine along kink sites, diffuse into the oxide, react with the oxide, etc. Di-interstitial recombination¹² and formation of silicon monoxide¹³ have been used to account for a wide range of experimental data. Production of SiO from the reaction $2\text{Si} + \text{SiO}_2 \rightarrow 2 \text{SiO}$ has been used to account for the significant diffusivity of self-interstitials in silicon dioxide [CEL89a]. Enhanced and retarded diffusion of certain dopants due to a vacancy supersaturation has also been attributed to SiO [AHN89, CEL89b]. However, the production of SiO is a high temperature process and is unlikely to form under the annealing conditions used in this study [AHN89].

There appears to be one requirement for interstitial recombination to take place at the surface Si/BOX interface – dose loss to the BOX. Since the Si/SiO₂ interface is typically a very smooth interface for thicker thermally grown oxides, [BRU97] it is a logical conclusion that the interface must be damaged in order to serve as a sink for trapped interstitials. This damage occurs whenever the implant profile is truncated by the BOX. By increasing the number of kink

sites and dangling bonds at the interface, it is proposed the interstitials have a greater probability of recombining at the surface Si/BOX interface. However, without the damage the interface is unable to compete with the ability of extended defects to trap interstitials.

An alternative explanation is that the peak interstitial concentration must be within 100–200 Å of the interface before the trapped interstitial population is affected. However, the straggle of the implant is a more important parameter for this argument. At 20 keV, there is a noticeable decrease in Si_i for the 700 Å SOI, yet the peak interstitial concentration is 350–400 Å from the surface Si/BOX interface. The straggle is much greater at this energy. This could explain why there is not a decrease in Si_i for the 300 Å SOI at 5 keV. The peak interstitial concentration is only ~ 200 Å from the interface, but the straggle is much less at this energy so there is no noticeable decrease in Si_i . In order to place the peak interstitial concentration close to the interface the straggle must increase, thus more of the implant is truncated by the BOX leading to a damaged surface Si/BOX interface. This supports the proposition in the preceding paragraph.

4.2.3.4 Conclusions

The effect of the surface Si/BOX interface on extended defect evolution in SOI scaled to 300 Å has been investigated via plan-view TEM. It is observed that the interface does not enhance the dissolution rate of extended defects unless $\geq 15\%$ of the dose is truncated by the BOX. Further, no reduction in the trapped interstitial concentration is seen unless $\geq 6\%$ of the dose is truncated. It is concluded that the surface Si/BOX interface does not serve as a significant sink for interstitial recombination, as long as the interstitial profile is mostly confined to the surface Si layer. It is proposed that by effectively damaging the surface Si/BOX interface as the implant energy increases, the number of kink sites and dangling bonds are increased and

the interstitials have a greater probability of recombining at the interface. Without the damage, the interface is unable to compete with the ability of the extended defects to trap interstitials.

4.3 Amorphizing Implants

This experiment set out to investigate the effect of the interface on EOR loop evolution in SOI. Nucleation of oxidation stacking fault (OSF) defects off the EOR damage was also studied.

4.3.1 Experimental

Starting materials in this experiment were the same as those in the previous one. Si⁺ implantation was performed at room temperature at 5 keV, $1 \times 10^{15} \text{ cm}^{-2}$ with tilt and twist angles of 7° and 22°, respectively. Anneal temperatures were chosen to be 750 °C, 835 °C, 900 °C, and 1000 °C, while times were chosen based on a activation energy for dissolution of 5.1 eV, similar to the design in the {311} experiments. Inert ambient furnace anneals were performed for times of five minutes or less in a Lindberg furnace. Rapid thermal annealing (RTA) using an AG Associates RTA was used for short times. PTEM analysis and quantification were performed in a manner similar to the experiments discussed previously. Oxide thickness was measured using a multi-wavelength spectroscopic ellipsometer.

4.3.2 Results

Figure 4-29 shows the damage profiles simulated using UT-Marlowe. The continuous amorphous layer appears to be approximately 15-16 nm thick. This was confirmed using ellipsometry to be $167.5 \pm 7.5 \text{ \AA}$. This meant that slightly more than 10 nm of the surface Si film was not amorphized in the 300 Å SOI specimens.

The EOR loop evolution at 835°C is shown in Fig. 4-30 for the 300 Å, 1600 Å, and bulk Si, specimens. Interestingly, many of the loops show an indiscrete morphology about their circumference that was not observed in the non-amorphizing loop study above. This could be a

result of the low energy used, such as that observed for boron by Earles [EAR02]. Comparing the different materials, the loops in the 300 Å appear smaller than the 1600 Å or bulk Si. However, the 1600 Å shows similar characteristics to the bulk. Figure 4-31 shows the QTEM data at 835°C for the 300 Å, 700 Å, 1600 Å, and bulk Si. Defect size was calculated by measuring the area contained within the loop, and assuming the loop to be circular. The diameter of the loop could then be extracted. A reduction in the concentration of trapped interstitials in the loops occurs in the 300 Å SOI, but no enhancement in decay rate appears at 835°C. The defect density among the different materials does not vary significantly, but the defect size of the 300 Å is measurably less than the others.

Upon further annealing, oxidation stacking faults (OSFs) appear to nucleate from the undissolved loops. This is evidenced by the PTEM micrographs in Fig. 4-32. Initially, there does not appear to be a significant difference in the evolution of the OSFs between the different materials. However, after annealing for two days at 835°C a clear difference is observed in the OSF growth in the 300 Å SOI. The lengths of the faults appear relatively constant in the different materials, but the width is substantially less for the 300 Å. Thus, the interfaces appear to pin the fault, preventing it from adding additional {111} layers and growing. The QTEM data for the OSFs at 835°C is shown in Fig. 4-33. The major axis is essentially the fault length, while the aspect ratio was calculated as the length divided by the width. Figure 4-34 shows the concentration of trapped interstitials for both EOR loops and OSFs at 835°C. The decrease and subsequent increase in the concentration indicates that interstitial injection is occurring to create the OSFs. Ellipsometry confirmed that this was the case, but no difference in the oxide growth rate was observed among the materials.

The QTEM data for EOR loops and OSFs at 900°C are shown in Figs. 4-35 and 4-36, respectively. Interestingly, the loops in the 300 Å appear to dissolve faster than in the other materials. The concentration of trapped interstitials in OSFs was also less for the 300 Å. Once again, significant differences in the aspect ratio are seen as the surface Si layer is thinned. The EOR loops appeared to dissolve in less than 10 seconds at 1000°C during the RTA, so only the OSF data is reported in Fig. 4-37. In this case, there appears to be differences between the OSF evolution among the SOI and bulk materials. A reduction in the concentration of trapped interstitials is observed in the SOI materials, while the bulk Si continues to increase. The defect density is similar, but much larger OSFs formed in the bulk materials at this temperature.

4.3.3 Discussion

Solid phase epitaxial regrowth (SPE) did not result in the formation of twins within the surface Si layer, as might have been expected. This indicates that the amorphous layer depth may be brought even closer than 100 Å to the surface Si/BOX interface, as SOI devices continue to scale.

Compared to the non-amorphizing loop study discussed previously, a significant reduction in the concentration of trapped interstitials in the 300 Å SOI was observed at 835°C. Thus, an effect of the interface occurred by allowing the loops to form around the EOR instead of near the projected range, despite the equivalent implant energy. The difference in ranges was around 5 – 6 nm at the implant energy of 5 keV. The EOR loops are also much more stable, although this is mostly due to the increased dose.

The peculiar shape of many of the loops is not completely understood. It could be hypothesized that this is a low energy effect, as mentioned above. Zig-zag {311} defects are expected to form under these conditions before the stable EOR loops. It could be proposed that

the unfauling of the zig-zag {311}s creates the observed non-uniformity in the loop morphology. The morphology also resembles that of a dislocation loop network, similar to that observed by Earles during laser annealing of B implanted Si [EAR02].

Formation of OSFs, indicates that the nitrogen ambient used to anneal the specimens contains residual oxygen. The amount of residual oxygen varied between those specimens annealed in the RTA versus furnace annealed ones. In order to avoid this, a reducing ambient (e.g. H_2) or ultrahigh vacuum conditions should be used.

A temperature dependence of the interface characteristics also appears to be evident. No enhancement in the decay of the trapped interstitial population from EOR loops was observed for the 300 Å at 835°C. However, an enhancement did occur at 900°C. There did not appear to be differences in the EOR loop evolution between the 700 Å, 1600 Å and bulk Si.

For the 700 Å and 1600 Å at 1000°C, OSFs did not seem to grow the same as at lower temperatures. The OSFs in the bulk appeared to continue to grow, while those in the SOI shrunk. This could indicate that there is a temperature dependence to the ability of the surface Si/BOX interface to absorb interstitials from OSFs.

4.3.4 Conclusions

The effect of the surface Si/BOX interface on EOR dislocation loop and OSF evolution has been studied for surface Si thickness of 300 Å, 700 Å, and 1600 Å. It was shown that the decay of trapped interstitials varied for the 300 Å SOI depending on whether or not the implant was amorphizing for the same implant energy. Despite annealing in nitrogen, enough residual oxygen was present to lead to the nucleation of OSFs after annealing for long times or at high temperatures. At 835°C the concentration of trapped interstitials in EOR loops for the 300 Å SOI was more than 2X less than the other materials. However, no enhancement in the decay

was observed until annealing at 900°C. No difference in EOR evolution was observed between the 700 Å, 1600 Å, and bulk. Upon annealing for long times at 835°C, aspect ratios of OSFs varied significantly as the surface Si layer was thinned to 300 Å. OSF evolution appeared to depend significantly on temperature for the SOI materials. Annealing at 1000°C resulted in the eventual shrinkage of OSFs in the 700 Å and 1600 Å SOI. This indicates a possible temperature dependence to the ability of the interface to absorb interstitials from OSFs.

4.4 Summary

This chapter has centered around understanding the effect of the surface Si/BOX interface on the evolution of Type I and II extended defects in SOI. It was shown that the behavior of the interface is extremely sensitive to the implant conditions used. {311} defect evolution seemed to be affected the most by the presence of the buried interface, while dislocation loops were relatively impervious until significant as-implanted dose loss occurred. Simulation of {311} defects in SOI is the subject of the following chapter. Distinction was also made between non-amorphizing and amorphizing loop evolution. For FD-SOI material, the evolution of loops was affected when an amorphizing dose was used due to the reduced proximity to the interface. Annealing ambient also appeared to play a role, as significant differences in OSF growth and shrinkage were observed between SOI and bulk Si, particularly at high temperatures.

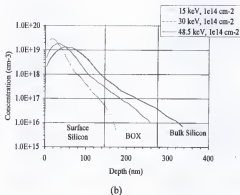
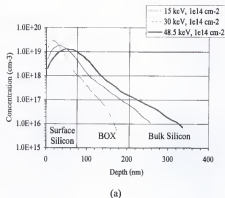


Figure 4-1. UT-Marlowe ion profile simulations for Si^+ implants into (a) 750 Å and (b) 1450 Å SOI at 15, 30 and 48.5 keV, $1 \times 10^{14} \text{ cm}^{-2}$.

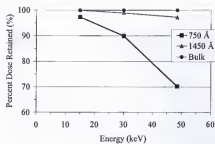


Figure 4-2. Dose loss calculated from UT-Marlowe simulations for implant energies used in the study.

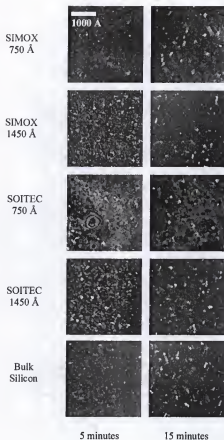


Figure 4-3. Weak beam dark field images of SOI and bulk silicon for Si^+ , 15 keV, $1 \times 10^{14} \text{ cm}^{-2}$ implants after annealing at 750 °C for 5 and 15 minutes.

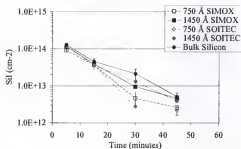


Figure 4-4. Concentration of trapped interstitials in all extended defects for Si^+ , 15 keV, $1 \times 10^{14} \text{ cm}^{-2}$ annealed at 750 °C.

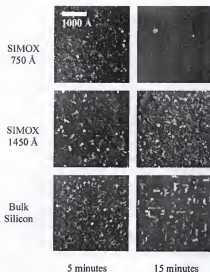


Figure 4-5. Weak beam dark field images of SOI and bulk silicon for Si⁺, 30 keV, $1 \times 10^{14} \text{ cm}^{-2}$ implants after annealing at 750 °C for 5 and 15 minutes.

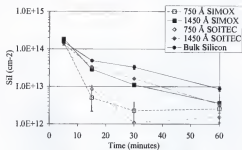


Figure 4-6. Concentration of trapped interstitials in all extended defects for Si⁺, 30 keV, 1×10^{14} cm⁻² annealed at 750 °C.

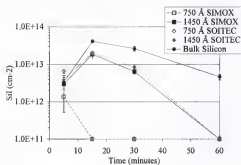


Figure 4-7. Concentration of trapped interstitials in only {311} defects for Si^+ , 30 keV, $1 \times 10^{14} \text{ cm}^{-2}$ annealed at 750 °C.

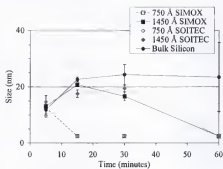


Figure 4-8. Average size of {311} defects in SOI and bulk for Si^+ , 30 keV, $1 \times 10^{14} \text{ cm}^{-2}$ annealed at 750 °C.

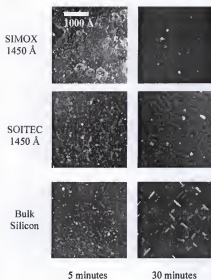


Figure 4-9. Weak beam dark field images of SOI and bulk silicon for Si^+ , 48.5 keV, $1 \times 10^{14} \text{ cm}^{-2}$ implants after annealing at 750 °C for 5 and 30 minutes.

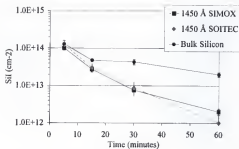


Figure 4-10. Concentration of trapped interstitials in all extended defects for Si⁺, 48.5 keV, $1 \times 10^{14} \text{ cm}^{-2}$ annealed at 750 °C.

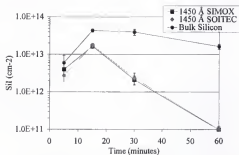


Figure 4-11. Concentration of trapped interstitials in only {311} defects for Si^+ , 48.5 keV, $1 \times 10^{14} \text{ cm}^{-2}$ annealed at 750 °C.

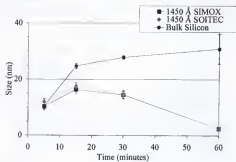


Figure 4-12. Average size of {311} defects in SOI and bulk for Si^+ , 48.5 keV, $1 \times 10^{14} \text{ cm}^{-2}$ annealed at 750 °C.

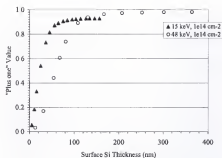


Figure 4-13, "1" value as a function of surface Si thickness for different implant energies used in the study.

Table 4-1. Equivalent annealing times assuming 3.7 eV activation energy for {311} defects in bulk Si.

Temp	Time				
700 °C	40 min.	122 min.	244 min.	489 min.	979 min.
750 °C	5 min.	15 min.	30 min.	60 min.	120 min.
825 °C	18 sec.	55 sec.	110 sec.	220 sec.	440 sec.

Table 4-2. Ion range statistics determined using UT-Marlowe and SRIM simulations.

	UT-Marlowe	SRIM
Energy	R_p (Å)	R_p (Å)
15 keV	180	240
30 keV	330	446
48.5 keV	550	700

Table 4-3. Dose loss for 750 Å and 1450 Å SOI determined using UT-Marlowe.

	750 Å SOI	1450 Å SOI
Energy	Dose Loss (%)	Dose Loss (%)
15 keV	3	<1
30 keV	10	1
48.5 keV	30	3

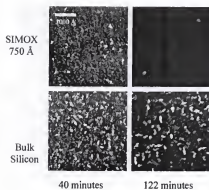
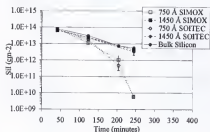
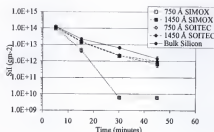


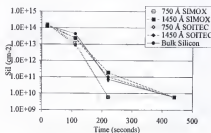
Figure 4-14. Weak beam dark field micrographs of 750 Å SIMOX and bulk silicon for Si^+ , 30 keV, $1 \times 10^{14} \text{ cm}^{-2}$ implants after annealing at 700 °C for 40 and 122 minutes.



(a)

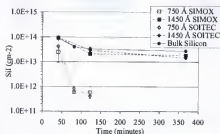


(b)

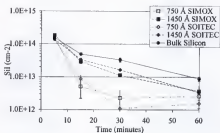


(c)

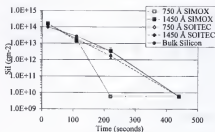
Figure 4-15. Concentration of trapped interstitials in $\{311\}$ defects for Si^+ , 15 keV, $1 \times 10^{16} \text{ cm}^{-2}$ annealed at (a) 700 °C, (b) 750 °C, and (c) 825 °C. (Note: $S_{II} = 6 \times 10^9 \text{ cm}^{-2}$ is TEM detection limit)



(a)

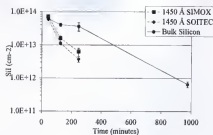


(b)

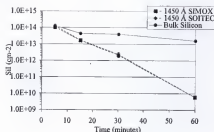


(c)

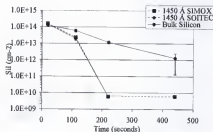
Figure 4-16. Concentration of trapped interstitials in $\{311\}$ defects for Si^+ , 30 keV, $1 \times 10^{14} \text{ cm}^{-2}$ annealed at (a) 700 °C, (b) 750 °C, and (c) 825 °C.



(a)

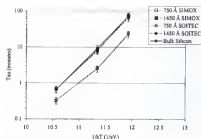


(b)

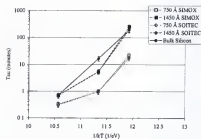


(c)

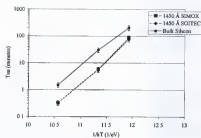
Figure 4-17. Concentration of trapped interstitials in {311} defects for Si^+ , 48.5 keV, $1 \times 10^{14} \text{ cm}^{-2}$ annealed at (a) 700 °C, (b) 750 °C, and (c) 825 °C.



(a)



(b)



(c)

Figure 4-18. Plot of time constant as function of $1/kT$ for (a) 15 keV, (b) 30 keV, and (c) 48.5 keV.

Table 4-4. Extracted activation energies from Figure 4-18 for SIMOX, SOITEC and bulk Si.

Energy (keV)	Activation Energy, E_a (eV)				
	SIMOX 750 Å	SIMOX 1450 Å	SOITEC 750 Å	SOITEC 1450 Å	Bulk Si
15	3.13 ± 0.3	3.45 ± 0.30	3.10 ± 0.30	3.38 ± 0.30	3.47 ± 0.3
30	3.03 ± 0.33	4.26 ± 0.30	2.9 ± 0.3	4.1 ± 0.3	4.13 ± 0.3
48.5		4.09 ± 0.30		3.99 ± 0.3	3.64 ± 0.3

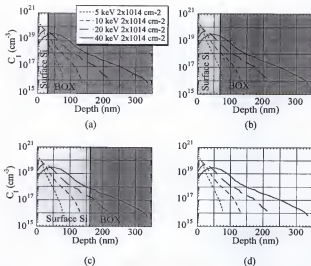


Figure 4-19. Ion profiles from UT-Marlowe for (a) 300 Å, (b) 700 Å, (c) 1600 Å, and (d) bulk Si after Si^+ implantation from $5 - 40 \text{ keV } 2 \times 10^{14} \text{ cm}^{-2}$.

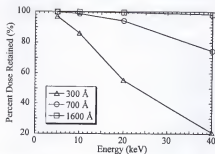


Figure 4-20. Percentage of dose retained in surface Si layer of SOI for Si⁺ implants from 5 keV to 40 keV, $2 \times 10^{14} \text{ cm}^{-2}$.

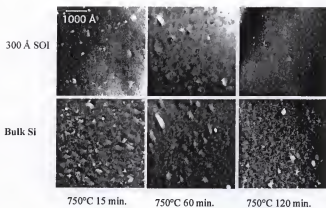


Figure 4-21. Plan-view TEM micrographs illustrating defect evolution in 300 Å SOI and bulk Si for 5 keV, $2 \times 10^{14} \text{ cm}^{-2}$ after annealing at 750° C.

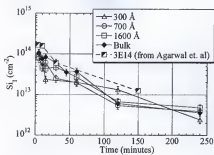


Figure 4-22. Concentration of trapped interstitials (S_i) in extended defects for 5 keV, $2 \times 10^{14} \text{ cm}^{-2}$ after annealing at 750° C.

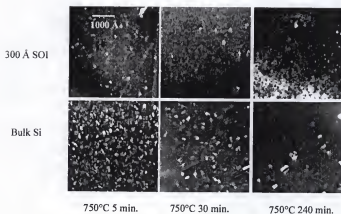


Figure 4-23. Plan-view TEM micrographs illustrating defect evolution in 300 Å SOI and bulk Si for 10 keV, $2 \times 10^{14} \text{ cm}^{-2}$ after annealing at 750° C.

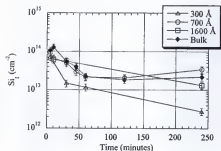


Figure 4-24. Concentration of trapped interstitials in extended defects for 10 keV, $2 \times 10^{14} \text{ cm}^{-2}$ after annealing at 750°C.

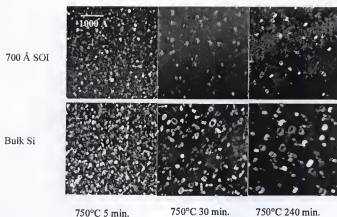


Figure 4-25. Plan-view TEM micrographs illustrating defect evolution in 700 Å SOI and bulk Si for 20 keV, $2 \times 10^{14} \text{ cm}^{-2}$ after annealing at 750° C.

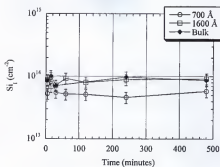


Figure 4-26. Concentration of trapped interstitials in extended defects for 20 keV, $2 \times 10^{14} \text{ cm}^{-2}$ after annealing at 750° C.

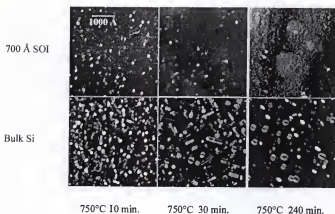


Figure 4-27. Plan-view TEM micrographs illustrating defect evolution in 700 Å SOI and bulk Si for 40 keV, $2 \times 10^{14} \text{ cm}^{-2}$ after annealing at 750° C.

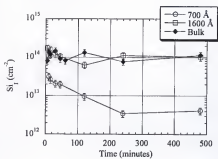


Figure 4-28. Concentration of trapped interstitials in extended defects for 40 keV, $2 \times 10^{14} \text{ cm}^{-2}$ after annealing at 750° C.

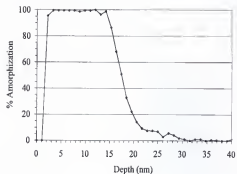


Figure 4-29. UT-Marlowe RBS profile showing percent amorphization versus depth. Amorphous layer is approximately 15 nm thick.

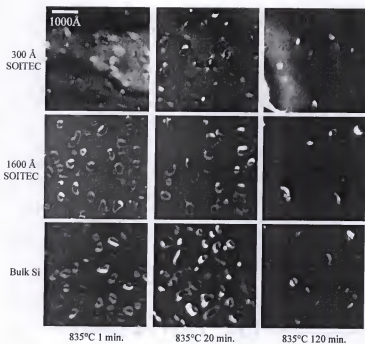


Figure 4-30. PTM micrographs of EOR loops in SOITEC and bulk Si after annealing at 835 °C in nitrogen. Implant was Si⁺, 5 keV, $1 \times 10^{15} \text{ cm}^{-2}$.

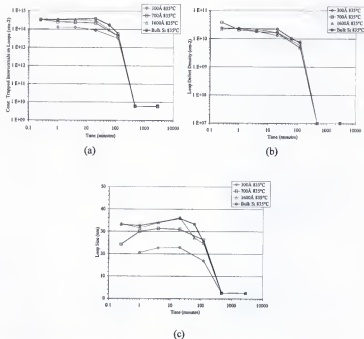


Figure 4-31. QTEM data for EOR loops annealed at 835°C including (a) concentration of trapped interstitials, (b) defect density, and (c) defect size.

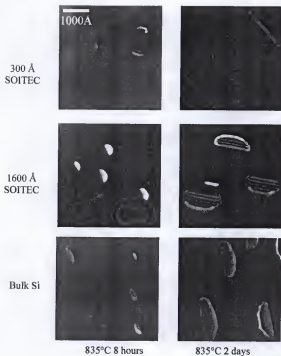


Figure 4-32. PTEM micrographs of oxidation stacking faults (OSFs) that appeared to nucleate off EOR loops upon further annealing at 835 °C. Note significant difference in aspect ratio between 300 Å SOI and the other materials. Implant was Si⁺, 5 keV, $1 \times 10^{15} \text{ cm}^{-2}$.

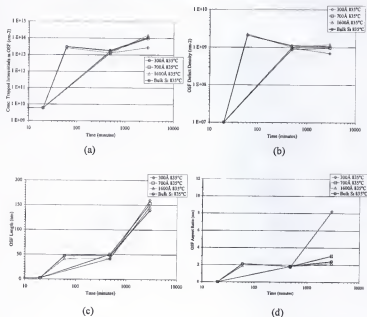


Figure 4-33. QTEM data for OSFs at 835°C including (a) concentration of trapped interstitials, (b) defect density, (c) major axis length, and (d) aspect ratio.

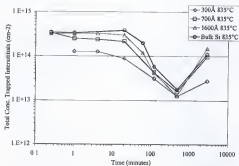


Figure 4-34. Concentration of trapped interstitials for both loops and OSFs at 835°C. Note increase in concentration as OSFs begin to nucleate off EOR loops.

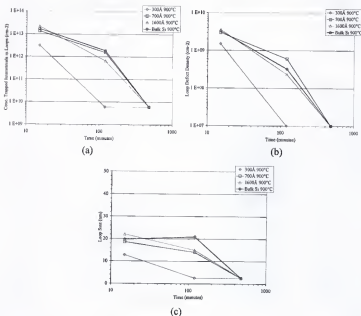


Figure 4-35. QTEM data for EOR loops annealed at 900°C including (a) concentration of trapped interstitials, (b) defect density, and (c) defect size.

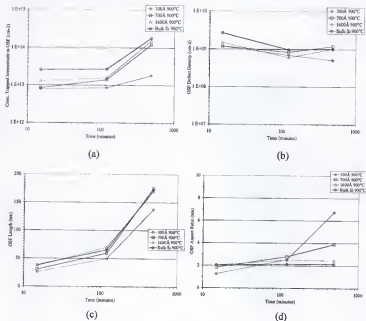


Figure 4-36. QTEM data for OSFs at 900°C including (a) concentration of trapped interstitials, (b) defect density, (c) major axis length, and (d) aspect ratio.

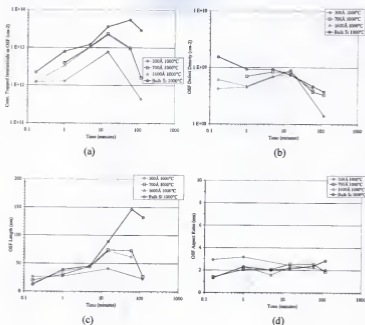


Figure 4-37. QTEM data for OSFs at 1000°C including (a) concentration of trapped interstitials, (b) defect density, (c) major axis length, and (d) aspect ratio.

CHAPTER 5 MODELING EXTENDED DEFECT EVOLUTION IN SOI

5.1 Introduction

Development of an accurate $\{311\}$ model for SOI must account for interstitial interactions with the surface Si/BOX interface, in addition to the native oxide/surface Si interface. This study attempted to validate the recent $\{311\}$ model of Law and Jones [LAW00] with SOI using the University of Florida version of FLOOPS. The model was tested using quantitative transmission electron microscopy (QTEM) data of Si^+ implants into separation by implantation of oxygen (SIMOX) and SOITEC materials discussed in the previous chapter.

5.1.1 Model Background

Unlike most previous models, the model of Law and Jones assumes $\{311\}$ dissolution to be controlled by release of interstitials from the ends of the defects rather than diffusion limited to the surface. This would seem to be a good approximation for application to SOI, since two interfaces are present. In that case, the $\{311\}$ s will not be largely affected by interface recombination; consistent with the QTEM data. The Law model also neglects an energy dependence on the defect size, since $\{311\}$ s are line defects. Lastly, the model assumes heterogeneous nucleation of defects on damage due to implantation.

A surface diffusion limited model is likely to account too strongly for the surface Si/BOX interface. The model of Rafferty et al., [RAF96] predicts the flux of interstitials from $\{311\}$ s to the surface to be inversely proportional to the projected range ($1/R_p$). For SOI, this would mean an increase in flux would depend on the distance of the projected range to the surface silicon/BOX interface.

A grid was developed which allows input of SOI parameters (e.g., surface Si, BOX thickness). Damage profiles were obtained from UT-Marlowe [MAR50] simulations. FLOOPS was used to simulate the room temperature damage evolution following the implant. FLOOPS then modeled the evolution of interstitials into submicroscopic interstitial clusters (SMICs) during the anneal. Simulation of the {311} nucleation and dissolution process was also done using FLOOPS. As in Law's model, {311} defects nucleate from submicroscopic interstitial clusters (SMICs).

5.1.2 Modeling Results

UT-Marlowe was used to simulate the interstitial profiles for the Si⁺ implants into the SOI and bulk materials. The time dependency of the trapped interstitial dose and the defect density for the 15 keV, $1 \times 10^{16} \text{ cm}^{-2}$ specimens is illustrated in Figs. 5-1 and 5-2, respectively. Reduction in the trapped interstitial dose occurs in the 750 Å SOI as annealing proceeds. Similarly, an enhancement in the decay of the defect density in the 750 Å SOI is observed. Figures 5-3 and 5-4 show the QTEM data for the 30 keV specimens. Once again, enhancement in the decay of the trapped interstitial population and defect density occurs in SOI. The effect is more pronounced in the 750 Å SOI, which is expected since significant as-implanted dose loss occurred.

The model fits the bulk Si data very well for both the 15 and 30 keV implants. However, the model fails to correctly predict the trapped interstitial decay in SOI. While the initial trapped interstitial dose is close to bulk Si, a significant enhancement in {311} dissolution occurs as the anneal time increases. As the surface silicon layer is thinned, the model breaks down more severely. This results in no {311} defects nucleating in the 750 Å SOI, even when the surface Si/BOX interface recombination velocity is made to be very low. The model is

unable to accurately account for the differences in {311} nucleation between SOI and bulk Si. This could be due to a reduction in the SMIC population if the interstitial recombination is too high. Since SMICs are the seed for {311}s, a reduction in their density and size will also result in an enhancement in the decay of the {311}s.

The model does predict a reduction in defect size in SOI, but the trend is overestimated. This is illustrated in figure 5-5, showing the defect size simulated for the 1450 Å SOI and bulk Si. From Law's model, the defect density decay rate (dD_{311}/dt) is assumed to be inversely proportional to the defect size (D_{311}/C_{311}). Thus, the enhanced decay in defect density can be thought to be due to a reduction in defect size in SOI. Once again, this is attributed to problems associated with the SMIC nucleation.

5.2 Summary

A first model for {311} defect evolution in SOI materials based on quantitative TEM measurements was attempted. We demonstrate that current models are unable to accurately predict evolution of {311} defects in SOI. This likely inhibits the nucleation of submicroscopic interstitial clusters (SMICs) in SOI, which serve as the seed for the {311} defects. However, Law's model does account for the experimental observation of reduced defect size in SOI. Future models need to account less for interstitial recombination at interfaces and more on nucleation mechanisms.

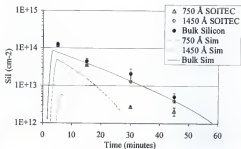


Figure 5-1. Trapped interstitial dose in SOI and bulk Si for Si^+ , 15 keV, $1 \times 10^{14} \text{ cm}^{-2}$ annealed at 750 °C. Data points are from QTEM data, lines are FLOOPS simulations. Note reduction in Si_i in 750 Å SOI as annealing proceeds.

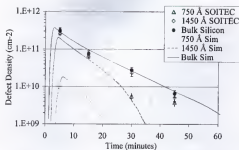


Figure 5-2. Defect density for Si^+ , 15 keV, $1 \times 10^{14} \text{ cm}^{-2}$ annealed at 750 °C. Defects dissolve faster in 750 Å SOI as anneal time proceeds. Model predicts large decrease in initial defect density in 750 Å SOI.

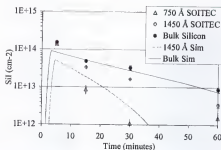


Figure 5-3. Trapped interstitial dose in SOI and bulk Si for Si^+ , 30 keV, $1 \times 10^{14} \text{ cm}^{-2}$ annealed at 750 °C. Note reduction in S_II in 750 Å and 1450 Å SOI as annealing proceeds. Model predicts no {311} formation in 750 Å SOI.

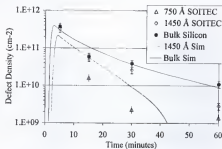


Figure 5-4. Defect density for Si^+ , 30 keV, $1 \times 10^{14} \text{ cm}^{-2}$ annealed at 750 °C. A significant enhancement in defect decay rate occurs in 750 Å SOI. Model predicts no defects form in 750 Å SOI.

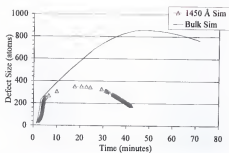


Figure 5-5. FLOOPS simulation of defect size for 1450 Å and bulk Si implanted at Si⁺, 30 keV, $1 \times 10^{14} \text{ cm}^{-2}$. Model overestimates differences in defects size between SOI and bulk Si.

CHAPTER 6 INVESTIGATION OF BORON INTERSTITIAL CLUSTERING IN SOI

6.1 Introduction

Formation of boron interstitial clusters (BICs) is a major problem in attempting to activate ultra shallow junctions. Instead of the maximum active carrier concentration being limited by solid solubility of boron, BICs form at much lower concentrations. It could be hypothesized that the segregation phenomenon might affect the degree to which certain dopants tend to cluster as they pileup or deplete at the interface. Simulations by Vuong et al., [VUO99] suggest that clustering of boron in SOI is similar to bulk Si.

Robinson et al., investigated electrical activation of arsenic in separation by implantation of oxygen (SIMOX) substrates and found little difference to bulk Si [ROB90]. Other investigations of mobility in SOI metal-oxide-semiconductor field effect transistors (MOSFETs) have found reduced electron and hole mobility due to phonon scattering as the surface Si thickness is reduced [SHO99, MAS01, GAM98, GAM01a]. On the other hand, for thicker SOI films the mobility in SOI is enhanced due to volume inversion [VAN01, GAM01b]. However, these cases for MOSFETs are quite different from that of SOI material that has not been fabricated into a device. These experiments set out to investigate the effect of surface Si thickness and dopant segregation on electrical activation of implanted boron in SOI. The first study set out to understand more about how secondary defect evolution differs in boron doped SOI compared to bulk silicon. The second study was aimed at investigating the time and temperature dependence of BIC formation in SOI. The third study concerns the concentration

dependence of BIC evolution. The chapter concludes by discussing the role of strain on B activation, as well as the relationship between B segregation and TED.

6.2 TEM Analysis of Boron Implanted SOI

6.2.1 Experimental

200 mm, p-type, {001}, $14 - 22 \Omega \cdot \text{cm}$, 4000 Å buried oxide UNIBOND® and 200 mm, p-type, {001}, $9 - 18 \Omega \cdot \text{cm}$ bulk silicon wafers were used in the experiment. SOI wafers were thinned from an initial surface silicon thickness of 1600 Å to 700 Å using thermal oxidation in wet O_2 , followed by etching in dilute HF (10:1). This yielded two SOI thickness (700 Å and 1600 Å) for comparison to the bulk silicon control. Thin screen oxides (20 Å) were deposited using low pressure chemical vapor deposition (LPCVD) to reduce channeling of the implanted ions. Wafers were then implanted with non-amorphizing, $^{11}\text{B}^+$, 6.5 keV and 19 keV, $3 \times 10^{14} \text{ cm}^{-2}$ ions at room temperature with 7° tilt and 22° twist angles. A 200 Å low temperature oxide (LTO) cap oxide was deposited via CVD in order to prevent out-diffusion of the boron during thermal processing. Samples were heated in a Thermolyne quartz tube furnace at 750°C for times ranging from 5 minutes to 8 hours under a nitrogen ambient.

Standard preparation techniques were used to make plan-view transmission electron microscopy (PTM) samples. These included cutting a 3 mm diameter disk, followed by grinding using a 15 µm alumina slurry. Chemical etching was done using a solution of HF:HNO_3 (1:3) until a hole was made. A buffered oxide etch (BOE) 6:1 for approximately 3 to 5 minutes was necessary in order to assist in removal the buried oxide following etching in HF:HNO_3 . A JEOL 200CX TEM, operating at 200 kV, was used to image the PTM specimens under g(3g) weak-beam dark field (WBDF) conditions. Quantitative TEM (QTEM)

was used to calculate the trapped interstitials in extended defects and interstitial clusters, as well as the defect density and defect size.

6.2.2 Results

It should be understood that a certain amount of dose and interstitials are lost to the BOX when the implant profile overlaps with the interface. This overlap becomes increasingly important as the implant energy is increased and/or the surface silicon layer thinned. Ion profiles were simulated using UT-Marlowe in order to approximate the retained dose within the surface silicon layer of the SOI [MAR50]. Significant overlap occurs for both implant energies in the 700 Å SOI. The 700 Å SOI loses approximately 6% of the dose at 6.5 keV and more than 50% at 19 keV. The 1600 Å retains the entire dose at 6.5 keV and loses 3% at 19 keV.

PTEM micrographs for the 6.5 keV implant energy are shown in Figure 6-1, illustrating the extended defect evolution process in SOI and bulk. In the bulk silicon, an assortment of {311} and dot defects can be seen after both 15 and 30 minutes of annealing. However, in the SOI only dot defects appear. A significant difference, not only in the defect structure, but also the size and density can also be seen. The dot defects in the 700 Å SOI are much smaller than those in the 1600 Å and have nearly dissolved after annealing for 30 minutes. After annealing for 60 minutes, the defects in the 700 Å can no longer be resolved due to the QTEM detection limit of $6 \times 10^9 \text{ cm}^{-2}$; they are assumed to have dissolved at this point. The defects in the 1600 Å and bulk dissolve after annealing between 1 and 2 hours. The QTEM data for the 6.5 keV specimens is shown in Fig. 6-2. It shows the concentration of interstitials trapped in extended defects as a function of the annealing time at 750°C. This is partly explained by the truncation of the implant profile by the surface silicon/BOX interface. In the 1600 Å, there appears to be a

reduction in Si_i (~50%) after annealing 30 minutes, but no enhancement in the decay rate compared to the bulk silicon.

Figure 6-3 shows some of the PTEM micrographs for the 1600 Å and bulk implanted at 19 keV. The 700 Å SOI does not form extended defects, which is partly attributed to the large dose loss (> 50%) of the implanted profile. Thus, no QTEM data can be obtained for the 700 Å. The 1600 Å shows an assortment of small dot defects, while the bulk silicon shows elongated {311} defects. These {311}s can be seen to coarsen in the bulk silicon, while the dot defects in the 1600 Å have nearly dissolved after 30 minutes. The concentration of trapped interstitials for the 19 keV specimens is shown in Fig. 6-4. The 1600 Å loses 3% of the dose initially, but a 50% decrease in the initial value of Si_i is observed. There is also an enhancement of approximately 2X in the decay rate in the 1600 Å compared to the bulk silicon. After annealing for 2 hours, the 1600 Å Si_i decays to the detection limit.

6.2.3 Discussion

Obviously, there is significant difference between SOI and bulk, in terms of defect microstructure after B^+ implantation. When compared to the previous experiments involving Si^+ implantation into SOI, significant difference in extended defect evolution is obtained by using a non-isovalent species such as boron. In the present study significant difference in Si_i is observed between SOI and bulk for dose losses much less than 6%. An enhanced decay rate is observed for as low as 3% dose loss in the 1600 Å SOI at 19 keV. The reason for the reduction in Si_i for low dose losses most obviously may be attributed to segregation of boron towards the surface Si/BOX interface. If a boron-interstitial pair was easily able to diffuse towards the surface Si/BOX interface, it may explain why fewer trapped interstitials were observed in SOI. However, no segregation was observed in SIMS data performed on the 1600 Å SOI, 19 keV,

$3 \times 10^{14} \text{ cm}^{-2}$ after annealing for 30 minutes at 750°C . Instead, the boron profiles showed no difference between the 1600 \AA SOI and bulk until the BOX was reached. Another hypothesis may then be proposed. This may be an enhancement in the formation of boron-interstitial clusters (BICs) in SOI compared to bulk silicon. This could explain the decrease in the trapped interstitial populations observed in the SOI, since the BICs are sub-microscopic. At the implanted dose of $3 \times 10^{14} \text{ cm}^{-2}$, the threshold for clustering of boron ($1 \times 10^{19} \text{ cm}^{-3}$) is well exceeded. However, at this point it would be premature to speculate on the source or mechanism causing this to occur within the surface silicon layer.

6.2.4 Conclusions

Secondary defect evolution after B^+ implantation has been studied in SOITEC SOI material and bulk silicon. Discrete differences in defect microstructure are observed between 1600 \AA SOI and bulk despite complete confinement of the implant profile within the surface silicon layer. A decrease in the trapped interstitial concentration is observed in SOI even with minimal dose loss to the buried oxide. Enhancements in the decay rate of the trapped interstitial population is also observed at lower than expected dose losses.

6.3 Time and Temperature Dependence of Boron Activation in SOI

6.3.1 Experimental

In the experiment 200 mm , (001) , p-type, $14\text{--}22 \text{ }\Omega\text{cm}$ UNIBOND® and Czochralski substrates were used. All the SOI substrates had a BOX thickness of 400 nm . The SOI substrates, having an initial surface Si thickness of 1600 \AA , were thinned to 700 \AA and 300 \AA using oxidation and etching in dilute HF (10:1). Prior to ion implantation, a screen oxide was thermally grown in a wet oxygen ambient to help reduce channeling of the boron ions. Room temperature non-amorphizing ion implantation of $^{11}\text{B}^+$ at a dose of $3 \times 10^{14} \text{ cm}^{-2}$ was performed for energies ranging from 1 keV to 6.5 keV at a 7° tilt and 22° twist angle. Implant energies

were designed to place the projected range of the implant at varying depths within the surface Si layer. Following the implants, a low temperature oxide (LTO) of 20 nm was deposited at 425°C in order to prevent dopant out diffusion of the shallow implants. This was performed using a plasma enhanced chemical vapor deposition system (PECVD) with the screen oxide still in place. Specimens were scribed into squares ranging from 10 mm x 10 mm to 14 mm x 14 mm. Anneals were performed in a Lindberg quartz tube furnace in a nitrogen ambient. Isothermal anneals at 750°C for times of 5 minutes to 48 hours were done to activate the implanted boron. Separate isochronal anneals for 30 minutes at temperatures of 450°C to 1050°C was also performed to understand the temperature dependence of the activation process.

Hall Effect was performed using an MMR Technologies system with a MPS-50 programmable power supply and H-50 Hall, van der Pauw field controller. A magnetic field of 3000 Gauss was used in all of the measurements. Current was varied from 1×10^{-7} A to 1×10^{-3} A in order to check the linearity of the Hall measurements. This allowed measurement of the hole mobility, sheet number, and sheet resistance. Hall scattering factors were determined by annealing specimens at 1000°C for 2 hours to obtain complete activation of the specimens. The active dose obtained was then divided by the implanted dose to yield the scattering factor. These were approximately 0.9, 0.9, 0.7, and 0.85, for the 300 Å, 700 Å, 1600 Å, and bulk, respectively.

Four-point probe measurements were done using a Jandel Multi Height Probe. A current of 438.02 μ A was used for bulk Si and 38.02 μ A for SOI. Geometrical correction factors were used since sample sizes greatly exceeded the probe spacing. Four-point probe was mainly used to compare sheet resistance values with those obtained from the Hall-van der Pauw, ensuring the reliability of the measurements.

Secondary ion mass spectrometry (SIMS) was performed using a CAMECA IMS-3F secondary ion mass spectrometer. An O_2^+ primary ion beam with an energy of 15 keV and 15° incident angle was used for obtaining boron concentration profiles. An ion beam current of 100 nA was used, along with an electron gun to assist with charge neutralization in the BOX. This helped determine the amount of boron segregation towards the BOX as annealing proceeded.

6.3.2 Results

UT-Marlowe [MAR50] simulations were used to determine the amount of as-implanted dose loss to the BOX. This was done, in the case of SOI, by truncating the ion/boron concentration profile at the surface Si/BOX interface and integrating the portion of the profile remaining in the surface Si layer. Figure 6-5 shows the ion concentration profiles obtained using UT-Marlowe, while Figure 6-6 shows percent dose retained calculated from the simulations. This is important to keep track of, since boron can certainly not serve as an acceptor if it lies in the BOX. Thus, it would affect the electrical measurements obtained from Hall and four-point probe. All the implant energies resulted in dose loss in the 300 Å SOI, ranging from less than 1 % at 1 keV to 50 % at 6.5 keV. The 700 Å SOI lost 6% of the dose at 6.5 keV, but did not lose any for the 1 keV or 3.5 keV. No dose loss to the BOX occurred in the 1600 Å SOI for any of the implants simulated.

Electrical data obtained from Hall effect measurements for the 1 keV and 6.5 keV implant energies annealed at 750°C are shown in Figures 6-7 and 6-8, respectively. Significantly less activation (Fig. 6-7a and 6-8a) can be seen to occur in all of the SOI specimens compared to bulk Si. Even after annealing for 48 hours, the active dose in SOI does not approach that of bulk Si. The hole mobility (μ_h) and sheet resistance (R_s) are also lower in SOI by roughly 300 cm^2/Vs . The sheet resistance in the 1600 Å SOI appears to be slightly less

than the 700 Å and 300 Å. The bulk Si results compare favorably with those of Lilak [LIL01], in terms of active dose, for boron implants at similar energies and doses. However, when compared to mobilities obtained by Sasaki et al., [SAS88] the problem appears to be that the bulk Si has an enhanced mobility rather than SOI being degraded. Sasaki et al., found mobilities for boron concentrations between $1 \times 10^{19} \text{ cm}^{-3}$ and $1 \times 10^{20} \text{ cm}^{-3}$ to be between 70 and $53 \text{ cm}^2/\text{Vs}$, respectively [SAS88]. This indicates that there is a contribution from the substrate to the active dose of B in the bulk Si specimens. This contribution corresponds to $5 \times 10^{13} \text{ cm}^{-2}$ to $6 \times 10^{13} \text{ cm}^{-2}$ for the background doping concentration in the p-type bulk substrates. Thus, the active doses in Figs. 6-7 and 6-8 must be reduced in accordance with the background contribution. When this is taken into account, the bulk is only slightly more active than SOI at early times. Figure 6-9 compares the sheet resistance obtained from 4-pt. probe with Hall Effect for each of the implant energies. The R_s values agree well, indicating the measurements are indeed reliable and not a result of instrument error.

Figures 6-10 and 6-11 show the isochronal Hall effect data for the 1 keV and 6.5 keV implant energies, respectively. For the 1 keV SOI specimens, the active dose was over 2 orders of magnitude less compared to bulk Si for temperatures less than 600°C. Significant activation occurs between 600°C and 750 °C in SOI. The 700 Å and 1600 Å activates slightly more than bulk Si as the annealing temperature exceeded 900 °C. Once again, lower mobility and sheet resistance occur in SOI, but the mobility is close to that found in [SAS88]. A significant decrease in mobility occurs in SOI and bulk Si as the temperature increases. However, the substrate contribution must once again be accounted for in the bulk specimens, as mentioned above. This is attributed to ionized impurity scattering as more boron atoms begin to occupy Si lattice sites [SCH98]. The sheet resistance in SOI does begin to approach bulk Si as the

annealing temperature increases. For the 300 Å SOI implanted at 6.5 keV, the active dose is higher below 600°C than the 700 Å and 1600 Å. This is surprising considering the increase in dose loss in the 300 Å SOI; intuitively, one would expect less dose to result in a lower active dose since carriers cannot activate in an oxide. However, it is likely due to a reduction in the BIC population for the 300 Å SOI. This is discussed further in the discussion section below.

SIMS profiles for the 300 Å SOI annealed at 750 °C are shown in Fig. 6-12.

Segregation of boron into the BOX occurs after annealing for 30 minutes, indicated by the depletion of boron as the surface Si/BOX interface is approached. Most segregation appears to take place in the first 30 minutes at 750°C, as evidenced by the 120 minute profile.

6.3.3 Discussion

The data acquired shows that a difference exists in the activation process between SOI and bulk. Activation in bulk Si shows a diminished temperature dependence compared to SOI. However, it is difficult to directly compare the two because of the higher activation in bulk Si at low thermal budgets. The boron implants were non-amorphizing, so solid phase epitaxy (SPE) did not occur in the experiments. This may have explained the higher activation in bulk Si at low temperatures, but this was not the case. Significant transient enhanced diffusion (TED) was observed in the bulk Si SIMS profiles. This eliminates the possibility of other thermal processing accidentally taking place that could have activated the boron in bulk Si. This may have been a valid point if no TED was observed, but this was also not the case. It could also be speculated that the results are simply an artifact of performing Hall effect on thin Si films. If this were the case full activation would not have been obtained, yet the results in Fig. 6-10 and 6-11 show that 100% activation was obtained in thick SOI annealed at high temperatures. When the contribution of the substrate is considered, it becomes clear that the difference

between bulk and SOI is not as significant. The effects of boron clustering, segregation, impurity trapping, and thermal strain, on the electrical activation results presented above are each discussed separately.

As indicated previously, high concentrations of boron in the presence of an interstitial supersaturation can result in the formation of boron-interstitial clusters (BICs) [STO97]. This is generally accepted to occur between $1 \times 10^{18} \text{ cm}^{-3}$ and $1 \times 10^{19} \text{ cm}^{-3}$ boron concentrations [STO97, MIR03, RAD02, LIL02]. Clustering is often observed as immobile peaks in SIMS profiles, low Hall doses, as well as reductions in the trapped interstitial population in extended defects [LIU96]. The boron concentrations in the present study are well above the clustering limit according to Fig. 6-12. Thus, it could be proposed that the lack of activation is a result of an increase in BICs in SOI. If more of the boron binds with the excess interstitials, it could reduce the electrical activation, assuming that particular BIC complex is not electrically active. Also, if a higher interstitial supersaturation is present in the surface Si layer it could provide the extra interstitials to allow for the increase in BIC population [MAN00].

It has been shown in the previous experiment that a reduction in the trapped interstitial dose in $\{311\}$ defects occurs in SOI after boron implantation at 6.5 keV and 19 keV, $3 \times 10^{14} \text{ cm}^{-2}$. This was attributed to an increase in BIC formation in SOI. However, the microstructure consists mainly of small dot defect clusters at 1 keV and 3.5 keV, rather than larger extended defects such as $\{311\}$ s and dislocation loops. The dot defects are more difficult to accurately quantify due to their small size, thus there could be significant error in the QTEM measurements at the lowest energies. This would tend to support the BIC theory in thick SOI.

A theory could be proposed suggesting that perhaps the surface Si/BOX interface actually prevents interstitials from diffusing into or recombining at the BOX. Rather, the

interface tends to behave as a more reflective boundary for interstitials. Interstitials released from the extended defects would tend to remain within the surface Si layer and be available to participate in the BIC process. This would explain the low activation observed for SOI. This theory would not be out of the realm of possibility based on results from previous experiments that show the interface is a weak sink for interstitials unless a large amount of the dose is lost to the BOX during the implant [SAA02a, SAA02b, SAA04a, SAA04b]. It has also been conjectured that the contact potential at the Si/SiO₂ interface sets up an electric field that is likely to repel interstitials for p-type material [DEV03].

A BIC theory also explains why the 300 Å SOI activated more than the thicker SOI at low temperatures for the 6.5 keV implant. Figure 6-13 shows the clustered dose in SOI and bulk Si for the 6.5 keV annealed at 750°C. The clustered dose was obtained by subtracting $1 \times 10^{19} \text{ cm}^{-3}$ from the boron concentration in the SIMS profiles and then integrating over the surface Si thickness. The significant reduction in clustered dose for the 300 Å SOI explains the higher activation that was measured despite the dose loss of boron to the BOX. This is due to an immediate loss of interstitials to the BOX due to the implant energy. The influence of a shallow vacancy rich region near the surface could also become more critical as interstitial loss to the BOX occurs. MeV energy Si⁺ implants have been used previously to provide a vacancy rich region closer to the surface. This, in conjunction with boron implantation near the peak of the vacancy profile, allows for I-V recombination to occur and thus reduce BIC formation [KAL03]. However, the influence of a vacancy rich region produced by low keV implants without the aid of the MeV Si⁺ implantation has not been experimentally observed to affect clustering. Figure 6-14 shows the fraction of active boron and has been adjusted to account for the dose loss in thin SOI. The fractional active dose was computed by dividing the active dose

measured from Hall by the total retained dose within the surface Si layer. It illustrates that the 300 Å SOI is able to approach bulk Si in terms of fractional activation at low temperatures. This further supports that interstitials are being lost to the BOX in thin SOI, thus reducing the BIC population. The dose loss argument explains why the active dose does not approach that of the thick SOI at higher temperatures.

Another theory that could be proposed to explain the lack of activation in SOI is that of boron segregation to the BOX. Significant segregation could result in dose loss to the BOX that would prevent the boron from activating. It is also not known whether boron pileup at the surface Si/BOX interface is active or not. The theory of dose loss can be disproved by realizing the amount of boron that would be required to segregate to the BOX in thick SOI. Significant segregation/dose loss does not occur in the 1600 Å SOI at the energies studied, so it cannot explain the low activation. Rather, the segregation is limited by the segregation coefficient (~ 0.3 for B) [JAE02] for boron in the two materials. Once the chemical potential between the two materials is equilibrated the boron ceases to segregate. The issue of pileup in thin SOI can be addressed by comparing the active dose obtained from Hall to the integrated SIMS dose remaining in the surface Si layer. This results in an active fraction of boron in the 300 Å SOI of 0.2-0.25, while the 1600 Å is closer to 0.1-0.13 (see Fig. 6-14). This indicates that the segregation in thin SOI does not result in significant deactivation of the boron. Rather, as indicated above, the reduction in BIC population promotes the activation of the boron in thin SOI.

A third theory might involve contaminants, such as C and O, serving as traps for the interstitials [WER98]. If this was the case the C and O could trap the interstitials present in the extended defects [GRI87, RUC99]. This could explain the QTEM data discussed in the

previous experiment [SAA04c]. However, it does not explain the QTEM data performed for Si⁺ implants into SOI where no significant difference was observed for implant profiles confined to the surface Si layer [SAA02a]. This indicates that the presence of boron is the major source of the reduction in trapped interstitials in [SAA04c]. Figure 6-15 shows C and O SIMS profiles obtained for SOI and bulk Si. The carbon levels for SOI and bulk are similar, while slightly more oxygen exists in bulk Si. This difference does not affect the trapping efficiency of extended defects in the bulk, though.

One final theory could be developed based on thermal strain present in SOI. This is due to differences in the linear thermal expansion coefficient between silicon and silicon dioxide, as well as the BOX and surface Si thickness. These values are $2.6 \times 10^{-6} \text{ }^{\circ}\text{C}^{-1}$ and $5 \times 10^{-7} \text{ }^{\circ}\text{C}^{-1}$ for silicon and silicon dioxide, respectively [PLU00]. Compressive stresses have been shown to significantly affect dopant diffusion in Si depending on their magnitude [ZHA99, AZI01, PAR95]. Enhancements of 2X in the diffusivity of boron have been observed for pressures approaching 5 Gpa [ZHA99]. Unfortunately, there have not been many studies to understand the affect of stress on activation in Si. It could be proposed that as SOI is annealed the strain in the surface Si layer increases due to the mismatch, thus preventing the boron from occupying substitutional lattice sites. However, above a certain temperature the BOX begins to viscously flow [CHI97] and accommodate the strain in the surface Si layer. The process of viscous flow of SiO₂ typically occurs around 1000°C, but this can be reduced depending on whether or not the SiO₂ is hydrated. This would allow the boron to occupy substitutional sites in the lattice and increase the activation in SOI. This theory could explain the lack of activation in SOI at low temperatures, as well as the activation at higher temperatures.

For tensile thermal stresses, the linear expansion coefficient is related the change in elongation per unit temperature according to

$$\alpha = \frac{\Delta l}{l_0(T - T_0)} \quad (6.1)$$

where α is the linear thermal expansion coefficient, Δl is the change in elongation, l_0 is the original length, and ΔT is the change in temperature in Kelvin. The tensile strain is given as

$$\varepsilon = \frac{\Delta l}{l_0} = \alpha(T - T_0) \quad (6.2)$$

where ε is the engineering strain. Using Hooke's Law, the thermal stress is

$$\sigma = E\varepsilon = E\alpha(T - T_0) \quad (6.3)$$

where σ is stress. Stoney [STO09] developed a method, based on the mechanics of beam bending, by which the stress in thin films on substrates may be calculated. Stoney's formula is commonly stated as

$$\sigma_f = \frac{F_f}{d_f w} = \frac{1}{6R} \frac{E_s d_s^2}{(1 - \nu_s) d_f} \quad (6.4)$$

where σ_f is the film stress, F_f the force exerted by the thin film, d_f the film thickness, w the width of the film, R the radius of curvature of the film, E_s the elastic modulus of the substrate material, d_s the substrate thickness, and ν_s Poisson's ratio of the substrate [OHR92]. Combining the effects of thermal strain and mechanical strain the total strain in the film and substrate are given as

$$\varepsilon_f = \alpha_f \Delta T + \frac{F_f (1 - \nu_f)}{E_f d_f w} \quad (6.5)$$

$$\varepsilon_s = \alpha_s \Delta T - \frac{F_f (1 - \nu_s)}{E_s d_s w} \quad (6.6)$$

In order for mechanical equilibrium to hold, ϵ_f must be equal to ϵ_s . This allows for calculation of the thermal mismatch force, F_f , by manipulating Eqs. 6.5 and 6.6. Since $d_s \gg d_f$, for case involving partially depleted SOI and fully depleted SOI, the film stress due to thermal mismatch between a film and its substrate can be stated as

$$\sigma_f(T) = \frac{F_f}{d_f w} = \frac{(\alpha_s - \alpha_f) \Delta T E_f}{(1 - \nu_f)} \quad (6.7)$$

SOI can be thought of as a multilayer structure consisting of two thin films on a bulk Si substrate. During annealing, the Si substrate expands at a greater rate than the BOX, thus creating a tensile stress in the overlying BOX. As SOI is allowed to cool down, the substrate also contracts at a greater rate than the BOX, allowing for a residual compressive stress to form in the layers. The intrinsic compressive stress in thermally grown SiO_2 has been measured to be between -0.2 GPa and -0.3 GPa, which is close to that predicted by Eq. 6.7 assuming viscous flow above 1000°C [HUS91]. According to Hooke's Law, this would correspond to a strain of 0.25% - 0.38% in the BOX. However, this stress would tend to be reduced during annealing since the films would expand/contract oppositely from that occurring during cool down. This pressure would not be significantly high enough to enhance the diffusivity of B in Si according to Zhao et al., [ZHA99], thus tending to shed doubt on this theory. SIMS profiles on the thick SOI and bulk Si confirmed that this was the case, as the diffusivity within the tail of the profiles appeared similar.

6.3.4 Conclusions

We have investigated the process of electrical activation of boron in SOI scaled to 300 Å using Hall Effect, Four Point Probe, and SIMS. We show a slight decrease in the active dose of boron in SOI compared to bulk Si at low annealing temperatures. This becomes obvious when the active dose contributed from the background concentration is considered. Lower mobility

and increased sheet resistance are also observed, but the mobility in SOI is close to that observed previously. Above approximately 900 °C the boron active dose in SOI approaches that of bulk Si. All these effects appear regardless of the surface Si thickness and implant energy. It is also shown that as the implant energy increases, fractional activation in thin SOI increases, likely due to a reduction in boron interstitial clusters in the surface Si layer. A number of theories are proposed to explain the lack of activation in SOI, but boron interstitial clustering appears the most likely source. These results could have significant impact on low temperature processes in SOI such as solid phase epitaxy, as well as high temperature annealing using high ramp rates.

6.4 Concentration Dependence of Boron Activation in SOI

This study aimed to investigate the concentration dependence of BIC dissolution in SOI. The effect of SOI substrate material was also studied to see if the method of fabrication plays a role in activation. It is believed that defects remaining within the surface Si film of materials produced using the separation by implantation of oxygen (SIMOX) method might affect the quality of the interface. Bonded SOI substrates (e.g., SOITEC) consist of a BOX formed by thermal oxidation and are thought to possess a superior interface.

6.4.1 Experimental

In the experiment, 200 mm p-type (001) SIMOX, SOITEC and Czochralski (CZ) wafers having resistivities of 14 – 22 Ω cm were used. Starting wafers had surface Si thickness of 1450 Å and BOX thickness of 1300 Å. Thinning of the surface Si film was done using oxidation and etching using HF to achieve the 750 Å SOI. A thin screen oxide of 2 nm was grown before implantation to assist with the randomization of the incident ions. Room temperature, non-amorphizing implantation of $^{11}\text{B}^+$ ions was performed at a constant energy of 15 keV. The dose

of the implant was varied from $3 \times 10^{14} \text{ cm}^{-2}$ to $1 \times 10^{15} \text{ cm}^{-2}$ to provide a varying boron peak concentration. After implantation, a low temperature oxide (LTO) was deposited using plasma enhanced chemical vapor deposition (PECVD) at 425°C to prevent outdiffusion of boron during annealing. A Kulicke and Soffe dicing saw system was used to dice samples into $12 \times 12 \text{ mm}$ square samples. A temperature of 825°C was used to activate the boron after implantation. Anneals for times less than 5 minutes were performed in an AG Associates rapid thermal annealing (RTA) system. Longer anneals were done in a Lindberg quartz tube furnace.

An MMR Technologies system with a MPS-50 programmable power supply and H-50 Hall, van der Pauw field controller was used to perform Hall Effect measurements. A 3000 Gauss magnetic field was used in each of the measurements. Single point mode was used to determine the hole mobility, sheet number, and sheet resistance. This flows 85% of the maximum current through the sample to provide one optimal reading. Hall scattering factors from the experiment above were used. These were taken to be 0.9, 0.7, and 0.85, for the 750 \AA , 1450 \AA , and bulk, respectively.

6.4.2 Results and Discussion

Boron ion profiles were obtained using UT-Marlowe 5.0 with the kinetic accumulation damage model (KADM). These are shown in Figure 6-16 along with the percent dose retained in the surface Si film. The retained dose was calculated by ignoring the boron implanted into the BOX and integrating the remaining concentration profile in the surface Si film. The 15 keV profiles can be seen to significantly overlap the surface Si/BOX interface for the 750 \AA SOI within the BIC regime. This resulted in a dose loss of 40-45%. Approximately 3-4% dose loss occurred in the 1450 \AA .

Figure 6-17(a) shows the active dose or sheet number for the $3 \times 10^{14} \text{ cm}^{-2}$ dose.

Significantly lower active dose was observed in SOI versus bulk Si. The 750 Å SOI was also less active than the 1450 Å in terms of sheet number. This was expected since the dose loss in the 750 Å was much greater. The time dependency of the sheet number was also much stronger in SOI than bulk Si.

The fraction of active boron in the 750 Å approached bulk Si, whereas the 1450 Å was the lowest. This can be understood by noting in Fig. 6-16 that the peak of the boron profile was placed close to the surface Si/BOX interface. The loss of boron was also coupled with a loss of interstitials. This effectively caused a reduction in the BIC population since they form in the areas of high concentration.

Figure 6-18(a) shows the hole mobility for the $3 \times 10^{14} \text{ cm}^{-2}$ implanted samples. The mobility in SOI appeared significantly lower than bulk Si, but no difference due to SOI thickness was observed. The SOI hovered around 50-60 cm^2/Vs , while bulk Si was in the range of 300 cm^2/Vs . As in the previous experiment, it is unclear why the mobility is so much higher in bulk Si. It should be pointed out that the mobility in SOI is similar to that found by Sasaki et al. [SAS88]. Once again, there appears to be a contribution from the substrate in the bulk Si specimens. This makes the active dose appear greater by approximately $5 \times 10^{13} \text{ cm}^{-2}$ to $6 \times 10^{13} \text{ cm}^{-2}$. Figure 6-18(b) illustrates that the sheet resistance was significantly higher in SOI. Bulk Si sheet resistance was around 100 Ω/square , while it was 700 Ω/square and 1500 Ω/square for the 1450 Å and 750 Å, respectively. The difference between the 750 Å and 1450 Å was likely due to the difference in the sheet number.

The sheet number and fraction of active boron for the 15 keV, $1 \times 10^{15} \text{ cm}^{-2}$ specimens appear in Fig. 6-19. In this instance the active dose of boron in SOI was much closer to bulk Si

than was the case for the $3 \times 10^{14} \text{ cm}^{-2}$ dose. As time proceeds, the 1450 Å actually significantly exceeded the bulk Si. This becomes even greater when the background contribution is considered for bulk Si. Similar to before, the truncation of the boron profile in the 750 Å SOI resulted in a significant enhancement in the fraction of active boron. Once again, the rate of activation in the 1450 Å was much faster than bulk Si. Mobility and sheet resistance trends were similar to the lower dose. SOI exhibited much lower mobility and higher sheet resistance.

Finally, Figure 6-20 shows the sheet number for the 750 Å and 1450 Å SIMOX and SOITEC specimens after annealing at 750 °C for 30 seconds. Differences between the two materials were within margins of error expected for the Hall effect. This indicates that the two main methods of SOI fabrication may not be as different as traditionally believed. This is attributed to the internal oxidation of silicon (ITOX) process, now in common usage when fabricating SIMOX wafers. This may remove many of the defects that used to plague SIMOX materials.

6.4.3 Conclusions

The concentration dependence of BIC dissolution has been investigated in SIMOX and SOITEC materials with surface Si thickness of 750 Å and 1450 Å. At lower concentrations, SOI exhibited significantly lower sheet numbers. As the boron concentration was increased SOI began to approach and exceed bulk Si. This is even more apparent when the background active dose is subtracted from the bulk Si. Degraded mobility and sheet resistance was observed at all concentrations compared to bulk Si, but is comparable with accepted standards. However, truncating the boron profile over the surface Si/buried oxide interface enhanced the fraction of active boron in the 750 Å SOI. This also led to a higher fractional activation in 750 Å SOI than bulk Si as the concentration increased due to a loss of interstitials, effectively reducing the BIC

population. Lastly, negligible difference in the sheet number between SIMOX and SOITEC materials was observed. This provides evidence that the difference in fabrication methods may not significantly affect the electrical characteristics.

6.5 Role of Strain on Boron Activation

This section describes the HRXRD analysis performed for quantifying strain within the SOI and bulk materials. This method has become popular over the years in its application to ion implanted and radiation damaged systems [SPE81, SER87, SER88, SER92, FEW93, SER93, EHR94, KLA94, THO94, MIL96, ZOL98, BOC02]. Recently, the HRXRD technique has been applied to investigating the quality of SOI materials [VEN92, ZHO96, KIM98, AHI98, COH99, COH03]. This study used ω - 2 θ rocking curves to precisely measure the strain within the surface Si and implanted layers.

6.5.1 Experimental

Starting and processed materials used in this experiment were the same as those discussed in the first two experiments of this chapter. A Philips X'Pert HRXRD system was used using the primary and secondary optics discussed in Ch. 3. A $1/2^\circ$ slit was inserted in the primary optics to prevent dispersion of the beam. No slits were used between the diffracted beam and detector. High tension and current values were 45 kV and 40 mA, respectively. $\text{Cu K}\alpha_1$ radiation ($\lambda=1.542 \text{ \AA}$) was generated from the bombardment of a Cu target with electrons from a tungsten filament tube. Samples were first mounted to a glass slide and then the slide directly mounted to the goniometer, both using double-sided scotch tape. Ni attenuation foils, 0.1 mm thick, were used to partially block the beam while the sample was being aligned. During data acquisition, the attenuator was set to engage when the count rate (cps) rose above 450,000 cps. When the count rate dropped below 400,000 cps the attenuator was set to disengage.

Alignment of the samples was performed by first aligning the surface with the beam. This was done by aligning the beam with the detector, while the sample was absent. A 2θ scan was used to swing the detector in and out of the beam to yield the maximum intensity. The detector was then aligned with the peak of the maximum intensity. The sample was slowly brought into the beam by adjusting the z-axis until an observed decrease in intensity occurred. When the sample had bisected the beam to half the maximum intensity, a ω scan was run to ensure the beam was near the center of the sample. This step was iterated until the beam was bisected at precisely the center. The second step in alignment involved aligning the lattice with the beam. The sample was moved to the particular Bragg peak of interest, usually (004) or (311), and a ω scan was done to locate the peak. This was followed by doing a ϕ scan, then ω scan to align the lattice again, as well as a ψ scan then ω scan. These steps were iterated until there were no further shifts in any of the particular axes, indicating the lattice was precisely aligned.

Rocking curves were performed using a ω - 2θ scan, but in some cases a ω scan. For fast data acquisition, a range of 2° , step size of 0.001° , and step time of 0.5 second, were used. For more accurate scans, a range of 1.5° , step size of 0.0005° , and step time of 1 second, were used. All data was collected at room temperature and pressure. Implant conditions studied were for B^+ , 3.5 keV, $3 \times 10^{14} \text{ cm}^{-2}$ samples.

6.5.2 Results and Discussion

Prudence must be exercised when performing rocking curve analysis on bonded SOI wafers, such as SOITEC. This is illustrated in Fig. 6-21. Every Si wafer is unique, in that there is always some misalignment when the wafer is cut from the crystal. Thus, the (001) planes are not precisely parallel to the surface. For bonded wafers, this becomes more complicated since two unique, miscut wafers are used to form one SOI wafer. This is shown in Fig. 6-21(a). This

results in the surfaces of the surface Si layer and bulk substrate being misaligned relative to each other. Further complications to rocking curve analysis arise during the process of direct bonding. Rotational misalignment around the [001] direction results due to the inability to perfectly align the wafers during bonding, shown in Fig. 6-21(b). Failure to recognize these misalignments can result in collection of erroneous data, such as that shown in Fig. 6-22. In those rocking curves, the beam was aligned to the lattice of the bulk substrate Bragg peak, rather than the surface Si peak. Figure 6-23 shows the misalignment between the surface Si layer and substrate for an as-implanted B⁺, 3.5 keV, $3 \times 10^{18} \text{ cm}^{-3}$ sample. It should be mentioned that SIMOX wafers do not suffer from these problems since only one wafer is used in the production. Although surface miscut exists in SIMOX wafers, the surface Si layer is still aligned relative to the substrate.

Analysis of SOI rocking curves is difficult due to the presence of Pendellosung fringes, or thickness fringes. These artifacts are illustrated in Fig. 6-24 for a 1600 Å SOITEC sample without implantation. The fringes are a result of diffracting off a finite, thin film, such as an epitaxial or in this case, a transferred layer. The intensity of the fringe relates to the scattering matter and volume sampled, while the period of the oscillation yields the film thickness. The diffracting power and excitation error are given as

$$P_{\text{eff}} = P_0 \frac{\sin^2 \xi}{\xi^2} \quad (6.7)$$

$$\xi = \frac{\sin 2\theta_B \Delta \theta t}{\gamma_H \lambda} \quad (6.8)$$

where θ_B is the Bragg angle, t the thickness, γ_H the directional cosine of the diffracted beam with respect to the inward normal to the surface, and λ the wavelength. For thinner films the oscillations are relatively long compared to thicker films, which can have very short oscillations.

Nonetheless, their presence makes comparison with bulk Si rocking curves difficult and this is discussed further below.

Figure 6-25 compares the unimplanted, as-implanted, and annealed (004) ω -2 θ rocking curves for 1600 Å SOI implanted with B⁺, 3.5 keV, 3×10^{14} cm⁻². It should be noted that the LTO deposition had occurred for the as-implanted and annealed samples. The anneal was performed at 900°C for 30 minutes. Several interesting artifacts can be pointed out, despite the interference from the thickness fringes. The fringes in the unimplanted sample exhibit similar intensities on both sides of the Bragg peak, as well as similar spacings. The as-implanted sample shows a distinctive rise on the left side of the peak indicating a compressive stress in the film. This is likely due to the presence of either self-interstitials, boron in an interstitial position, or boron interstitial clusters. The compressive stress attenuates further from the peak, indicating a gradient in the profile. This could be attributed to the interstitial profile as a result of the implant process. The fringes on the right side of the Bragg peak also appear shifted relative to the unimplanted sample. For the annealed sample, the fringes on the right side appear slightly higher than those of the unimplanted sample. This could be due to incorporation of substitutional B in the lattice.

Bulk Si (004) ω -2 θ rocking curves are shown in Figures 6-26 and 6-27 for unannealed and annealed samples, respectively. In the case of the unimplanted and as-implanted samples, similar features to SOI appear. Namely, a compressive shoulder is observed in the as-implanted case. In addition to this, a clear tensile peak appears on the right side of the substrate peak. This is also attributed to substitutional B, indicating that some activation took place during the LTO deposition. The unimplanted substrate peak appears fairly symmetric, but slight broadening on the left side is acknowledged. The substitutional B peak appears to shift towards

the left as the sample is annealed, with a distinct shoulder on the substrate peak for the 1050°C. This is explained as follows: at low temperatures the active B is highly localized within the implanted region. As annealing proceeds the B diffuses and becomes less concentrated within a single region. This explains the shift in the lattice parameter. After annealing at 1050°C the implanted profile is highly diffused, resulting in an active B gradient into the bulk.

Compressive shoulders and peaks also appear in the 600°C and 1050°C. The interstitial profile in the 600°C sample may still be fairly close to the as-implanted case and has not formed extended defects. The formation of defects could explain the compressive peak in the 750°C, since the defect band would be localized. Small dot defects were indeed observed after annealing at 750°C for 30 minutes. Injection of interstitials due to oxidation at the surface could produce the shoulder observed for the 1050°C sample. This could be similar to the process observed to form the OSFs discussed in Ch. 4.

Figures 6-28 and 6-29 compare the rocking curves for the 1600 Å SOI and bulk Si before and after annealing at 900°C, respectively. The as-implanted cases do show similar behavior as far as the interstitial profile goes. However, the SOI does not appear to achieve the same level of substitutional B as bulk Si. This would support the Hall measurements that showed significant activation in bulk Si at low temperatures. For the 900°C annealed samples, the compressive side of the surface Si peak does not drop off as rapidly as in bulk Si. The right side fringes in the SOI sample appear higher than the left side, but do not necessarily mimic the shape of the bulk Si peaks. Too much should not be read into a direct comparison of the curves between SOI and bulk Si since maximum intensities vary between the materials. Essentially, the substrate intensity is so much greater than that produced by the surface Si layer due to its finite thickness.

6.5.3 Conclusions

The processes of B activation and interstitial evolution after B⁺ ion implantation in SOI and bulk Si were investigated using the method of HRXRD. 1600 Å SOITEC and bulk Si samples were implanted with B⁺, 3.5 keV, $3 \times 10^{14} \text{ cm}^{-2}$ and annealed under isochronal conditions at a variety of temperatures. The substitutional B peak in bulk Si tended to shift towards the substrate peak as the thermal budget was increased. This is explained as delocalization of the B as the implant profile diffuses. Similar results were obtained for compressive stresses to the left of the surface Si or substrate peaks. Care must be taken when analyzing SOI rocking curves, particularly in the case of bonded SOI wafers. The presence of thickness fringes makes a direct comparison between SOI and bulk very difficult.

6.6 Relationship Between Boron Segregation and TED

This section discusses the role TED may play in B segregation towards the surface Si/BOX interface. It may be hypothesized that the segregation coefficient depends on the length of TED. Here, SIMS data is coupled with the PTEM results discussed in the first experiment.

6.6.1 Experimental

SOI and bulk Si materials for this experiment were the same as those used in the first two experiments. Processing and SIMS characterization techniques were discussed in the second experiment. Temperatures of 750°C and 1050°C were used to study the segregation and TED properties of FD-SOI and PD-SOI compared to bulk Si. Retained concentrations were taken as the average across the surface Si layer, while ignoring transient effects near the interfaces in SOI. Segregation coefficients were taken as the ratio of concentrations adjacent to the interface, but not in the transient region.

6.6.2 Results and Discussion

Figures 6-30 and 6-31 show SIMS profiles for the 1 keV and 6.5 keV samples after annealing at 750°C for 30 minutes. The matrix effects, due to sputtering from the surface Si layer to BOX, are clearly visible in each figure. A slight depletion of B, upon approach of the surface Si/BOX interface, can be seen at both implant energies. However, in terms of motion in the tail region, where TED typically dominates, no difference appears between SOI and bulk Si for the 1 keV energy. This can be understood by considering the QTEM data obtained for the lower energy implants, shown in Fig. 6-32. At 1 keV and 3.5 keV, the defect microstructure consists mainly of dot defects, rather than the rod-like {311}s observed for the 6.5 keV and 19 keV. The evolution of the dot defects appears quite similar between SOI and bulk Si, while {311} evolution varies considerably between the two. If the dot defects are what drives TED after low energy implantation, then it makes sense that the profiles appear similar at 1 keV. For the 6.5 keV energy discussed at the beginning of the chapter, {311} defects were shown to be significantly less stable in SOI than bulk Si. This explains the slight enhancement in the tail of the 1600 Å SOI after annealing at 750°C, shown in Figures 6-31 and 6-33. If the {311}s are dissolving faster in the 1600 Å, then the profile should be enhanced more than bulk Si. The question can then be raised: Why is the profile for the 1600 Å at 6.5 keV enhanced, while at 19 keV (Figure 6-34) it is not? This can be answered by considering that the concentration for the 19 keV is not low enough to observe the tail enhancement. Instead the concentration range remains in vicinity of where BICs dominate. This is why there is no tail enhancement in the 300 Å or 700 Å SOI observed at any of the implant energies. It was discussed earlier in the chapter that the BIC population appeared to be reduced when the peak of B profile overlapped the interface (e.g. 300 Å SOI implanted at 6.5 keV). A similar effect was observed for the 700 Å

SOI implanted at 19 keV, indicating that this effect is not limited to FD-SOI. The depletion of B near the interface can be explained using the experiments of Jung [JUN04] and Dev [DEV03] discussed in Chapter 2. When B atoms lie within the space charge region near the Si/SiO₂ interface, their charge state is such that the interface potential no longer repels the B, but attracts it. Thus, more of the B becomes incorporated into the SiO₂.

An advantage of using SOI for junction formation is illustrated in Figures 6-35 and 6-36. They show the SIMS profiles after annealing at 1050°C for 30 minutes for the 1 keV and 6.5 keV implant energies. The BOX acts as a very efficient diffusion barrier for B, because the diffusivity of B in SiO₂ is so low. The segregation coefficient dictates that more B cannot be incorporated from the surface Si layer into SiO₂ unless sufficient B has diffused into the bulk of the SiO₂. This results in a nearly ideal, box-shaped B profile remaining in the surface Si layer. Figure 6-37 shows the retained B concentration within the surface Si layer as a function of thickness. The concentration is observed to scale linearly with surface Si thickness, so long as significant dose loss does not occur. The segregation coefficient as a function of surface Si thickness is shown in Fig. 6-38. It appears that the segregation coefficient is sensitive to the surface Si thickness and implant energy. In general, the segregation coefficient appears to decrease with implant energy and increase with surface Si thickness. It could be proposed that for thinner SOI films, it is easier for the interstitials to be transported to the interface. First of all, the roughness of the interface is expected to be greater since it saw a greater portion of the implanted dose. Second, the interstitial profile is much closer to the interface in thinner films. If the interstitials also transport B to the interface, then it makes sense that more B is incorporated into the BOX, thus reducing the segregation coefficient.

6.6.3 Conclusions

In this section, the relationship between B segregation and TED were discussed. Enhanced B diffusion in PD-SOI was observed for the case where {311} defects formed and the B concentration was low enough to observe tail diffusion. Increased interstitial transport to the surface Si/BOX interface appears to be responsible for a reduction in the segregation coefficient for thinner films. This effect was also seen at higher implant energies. BIC dissolution was also enhanced in 700 Å SOI when the B profile overlapped the interface. These results imply that an enhancement in the dissolution rate of {311}s in SOI could lead directly to a reduction in the segregation coefficient of B in SOI.

6.7 Summary

This chapter discussed the characteristics of BIC formation in SOI and how they compare to bulk Si. Hall Effect data suggests a slight increase in BIC formation occurs in SOI compared to bulk Si at low temperatures and concentrations. These observations were supported by QTEM measurements of {311} defects. At higher concentrations and temperatures this effect seems to reverse itself. Truncation of the B profile by the surface Si/BOX interface appeared to increase the fraction of active B remaining in the surface Si layer. This was attributed to a reduction in the BIC population, but the influence of a shallow, vacancy-rich region near the surface could also play a role. HRXRD measurements were performed to determine the role of strain in the activation process. The substitutional B peak in bulk Si tended to shift towards the substrate peak as the thermal budget was increased. This is explained as delocalization of the B as the implant profile diffuses. Similar results were obtained for compressive stresses to the left of the surface Si or substrate peaks. Care must be taken when analyzing SOI rocking curves, particularly in the case of bonded SOI wafers. The presence of thickness fringes makes a direct comparison between SOI and bulk very difficult. Finally, the phenomena of TED and B

segregation were addressed. Enhanced B diffusion in PD-SOI was observed for the case where {311} defects formed and the B concentration was low enough to observe tail diffusion.

Increased interstitial transport to the surface Si/BOX interface appears to be responsible for a reduction in the segregation coefficient for thinner films. This effect was also seen at higher implant energies. These results imply that an enhancement in the dissolution rate of {311}s in SOI could lead directly to a reduction in the segregation coefficient of B in SOI.

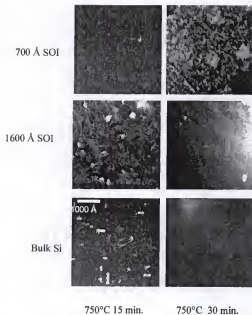


Figure 6-1. PTEM WBDF micrographs of defect evolution in SOI and bulk for B^+ , 6.5 keV, $3 \times 10^{14} \text{ cm}^{-2}$.

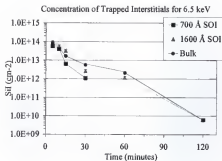


Figure 6-2. Trapped interstitial concentration (S_i) as a function of annealing time for B^+ , 6.5 keV, $3 \times 10^{14} \text{ cm}^{-2}$ specimens.

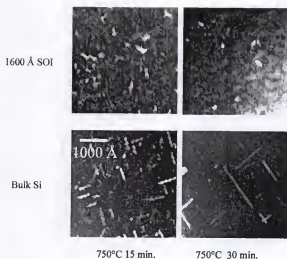


Figure 6-3. PTEM WBDF micrographs of defect evolution in SOI and bulk for B^+ , 19 keV, $3 \times 10^{14} \text{ cm}^{-2}$.

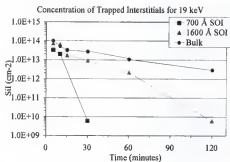


Figure 6-4. Concentration of trapped interstitials as a function of time for B⁺, 19 keV, 3×10^{14} cm⁻² specimens.

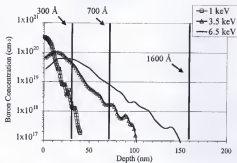


Figure 6-5. UT-Marlowe ion profile simulations for B^+ implants at 1 keV, 3.5 keV, 6.5 keV, $3 \times 10^{14} \text{ cm}^{-3}$. Note location of surface Si/BOX interface for 300 Å, 700 Å and 1600 Å SOI.

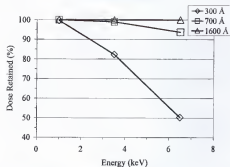


Figure 6-6. Percent retained dose of boron in surface Si layer as function of implant energy for 300 Å, 700 Å and 1600 Å SOL. Calculated using UT-Marlowe ion profiles.

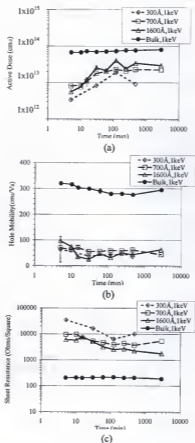
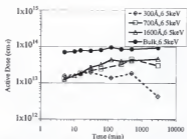
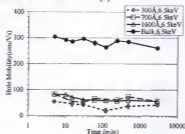


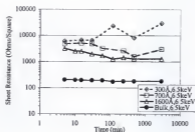
Figure 6-7. Isothermal Hall data for B^+ , 1 keV, $3 \times 10^{14} \text{ cm}^{-2}$ at 750°C including (a) active dose, (b) hole mobility, and (c) sheet resistance. Note that the active dose contribution from the background ($\sim 5 \times 10^{13} \text{ cm}^{-2}$ to $6 \times 10^{13} \text{ cm}^{-2}$) must also be subtracted from the bulk Si numbers.



(a)



(b)



(c)

Figure 6-8. Isothermal Hall data for B^+ , 6.5 keV, $3 \times 10^{14} \text{ cm}^{-2}$ at 750 °C including (a) active dose, (b) hole mobility, and (c) sheet resistance. Note that the active dose contribution from the background ($\sim 5 \times 10^{13} \text{ cm}^{-2}$ to $6 \times 10^{13} \text{ cm}^{-2}$) must also be subtracted from the bulk Si numbers.

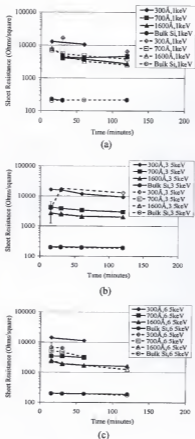


Figure 6-9. Comparison of sheet resistance data measured by four point probe and Hall Effect for (a) 1 keV, (b) 3.5 keV, and (c) 6.5 keV, $3 \times 10^{14} \text{ cm}^{-2}$ annealed at 750 °C. Solid symbols and lines represent four point probe measurements and open symbols represent Hall measurements.

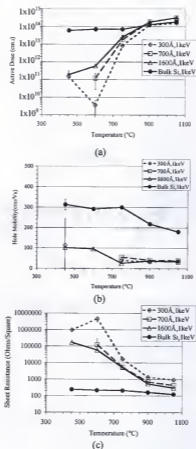


Figure 6-10. Isochronal Hall data for B^+ , 1 keV, $3 \times 10^{14} \text{ cm}^{-2}$ after annealing 30 minutes showing (a) active dose, (b) hole mobility, and (c) sheet resistance. Note that the active dose contribution from the background ($\sim 5 \times 10^{13} \text{ cm}^{-2}$ to $6 \times 10^{13} \text{ cm}^{-2}$) must also be subtracted from the bulk Si numbers.

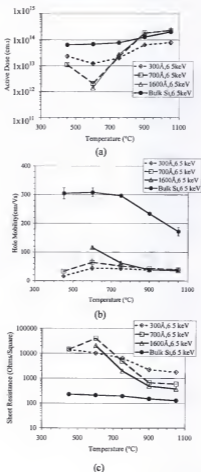


Figure 6-11. Isochronal Hall data for B^+ , 6.5 keV, $3 \times 10^{14} \text{ cm}^{-2}$ after annealing 30 minutes showing (a) active dose, (b) hole mobility, and (c) sheet resistance. Note that the active dose contribution from the background ($\sim 5 \times 10^{13} \text{ cm}^{-2}$ to $6 \times 10^{13} \text{ cm}^{-2}$) must also be subtracted from the bulk Si numbers.

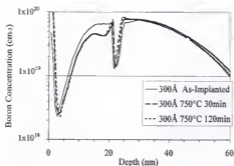


Figure 6-12. Boron concentration profiles from SIMS for 300 Å SOI implanted at 6.5 keV, $3 \times 10^{14} \text{ cm}^{-2}$ then annealed at 750 °C. Note segregation of boron into buried oxide.

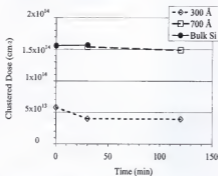


Figure 6-13. Clustered dose in SOI and bulk Si for B⁺, 6.5 keV, $3 \times 10^{14} \text{ cm}^{-2}$ annealed at 750 °C. Dose was obtained by integrating the B concentration profiles that lie above a level of $1 \times 10^{19} \text{ cm}^{-3}$.

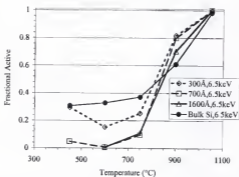


Figure 6-14. Active fraction of boron in SOI and bulk for 6.5 keV $3 \times 10^{14} \text{ cm}^{-2}$ annealed for 30 minutes.

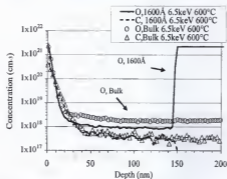
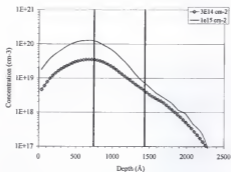
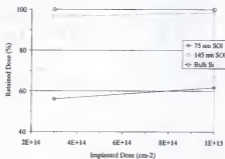


Figure 6-15. Carbon and oxygen SIMS profiles for 1600 Å SOI and bulk Si implanted with B⁺, 6.5 keV 3×10^{14} cm⁻², and annealed at 600° C for 30 minutes.

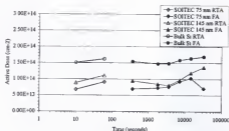


(a)

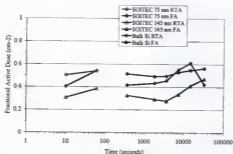


(b)

Figure 6-16. (a) Boron ion profiles from UT-Marlowe for 15 keV, $3 \times 10^{14} \text{ cm}^{-2}$ and $1 \times 10^{15} \text{ cm}^{-2}$. Vertical lines indicate the location of the surface Si/BOX interface. (b) Percent retained dose for 750 Å, 1450 Å, and bulk Si.

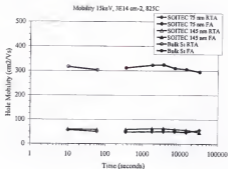


(a)

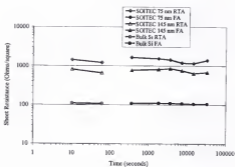


(b)

Figure 6-17. (a) Sheet number versus time for 15 keV, $3 \times 10^{14} \text{ cm}^{-2}$ annealed at 825 °C. Open symbols indicate RTA and closed circles indicate furnace anneals (FA). (b) Fractional active dose for 750 Å, 1450 Å, and bulk Si under same anneal conditions. Note that the active dose contribution from the background ($\sim 5 \times 10^{13} \text{ cm}^{-2}$ to $6 \times 10^{13} \text{ cm}^{-2}$) must also be subtracted from the bulk Si numbers.

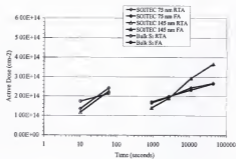


(a)

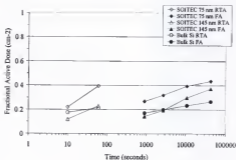


(b)

Figure 6-18. (a) Hole mobility versus time for 15 keV, 3×10^{14} cm $^{-2}$ annealed at 825 °C. Open symbols indicate RTA and closed circles indicate furnace anneals (FA). (b) Sheet resistance for 750 Å, 1450 Å, and bulk Si under same anneal conditions. Note that the active dose contribution from the background ($\sim 5 \times 10^{13}$ cm $^{-2}$ to 6×10^{13} cm $^{-2}$) must also be subtracted from the bulk Si numbers.



(a)



(b)

Figure 6-19. (a) Sheet number versus time for 15 keV, $1 \times 10^{15} \text{ cm}^{-2}$ annealed at 825 °C. Open symbols indicate RTA and closed circles indicate furnace anneals (FA). (b) Fractional active dose for 750 Å, 1450 Å, and bulk Si under same anneal conditions. Note that the active dose contribution from the background ($\sim 5 \times 10^{13} \text{ cm}^{-2}$ to $6 \times 10^{13} \text{ cm}^{-2}$) must also be subtracted from the bulk Si numbers.

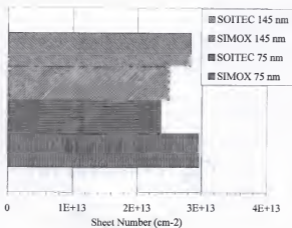


Figure 6-20. Sheet number versus time for 15 keV, $3 \times 10^{14} \text{ cm}^{-2}$ annealed at 750 °C for 30 seconds. Note insignificant difference in activation between SIMOX and SOITEC materials.

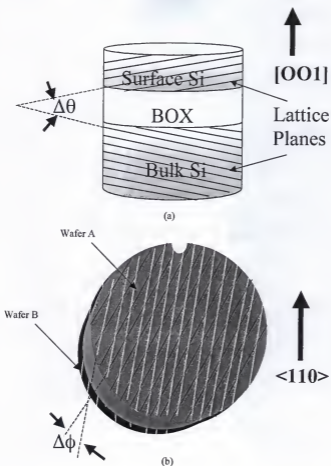


Figure 6-21. Schematic of (a) lattice/surface miscut and (b) bonding misorientation present in SOITEC materials. White lines in (b) show planes corresponding to wafer B, while black lines correspond to wafer A.

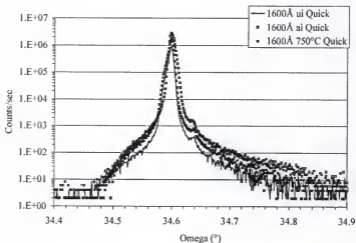


Figure 6-22. Erroneous (004) ω - 2θ rocking curves for 1600 Å SOITEC wafers implanted with B^+ , 3.5 keV, $3 \times 10^{14} \text{ cm}^{-2}$. Anneals were performed for 30 minutes at 750°C. Samples were aligned to substrate, rather than surface Si layer.

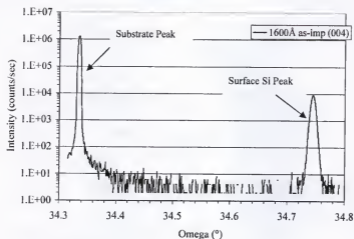


Figure 6-23. (004) ω rocking curves for 1600 Å SOITEC wafers as-implanted with B^+ , 3.5 keV, $3 \times 10^{14} \text{ cm}^{-2}$. Misalignment between the surface Si Bragg peak and substrate peak is shown.

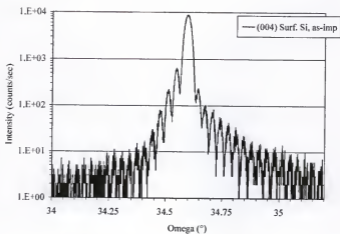


Figure 6-24. (004) ω -2 θ rocking curves for unimplanted 1600 Å SOITEC wafers, illustrating presence of Pendellosung fringes. Samples were aligned to surface Si layer.

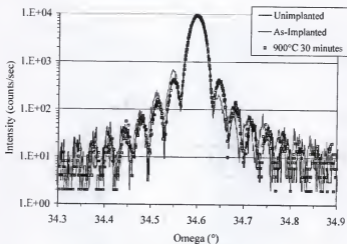


Figure 6-25. (004) ω -2 θ rocking curves for unimplanted, as-implanted, and annealed 1600 Å SOI implanted with B⁺, 3.5 keV, $3 \times 10^{14} \text{ cm}^{-2}$. Anneal was 900°C for 30 minutes.

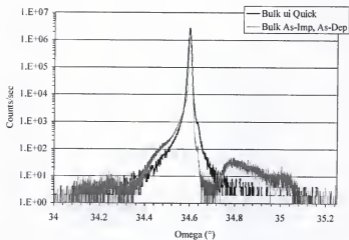


Figure 6-26. (004) ω -2 θ rocking curves for unimplanted and as-implanted bulk Si implanted with B⁺, 3.5 keV, 3×10^{14} cm⁻².

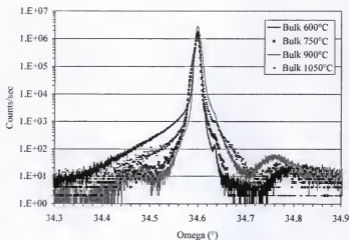


Figure 6-27. (004) ω -2 θ rocking curves for bulk Si implanted with B^+ , 3.5 keV, $3 \times 10^{14} \text{ cm}^{-2}$. Anneals were performed at 600°C, 750°C, 900°C, and 1000°C for 30 minutes.

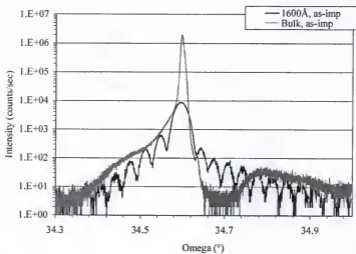


Figure 6-28. Comparison of (004) ω -2 θ rocking curves for 1600 Å SOI and bulk Si as-implanted with B⁺, 3.5 keV, 3×10^{14} cm⁻².

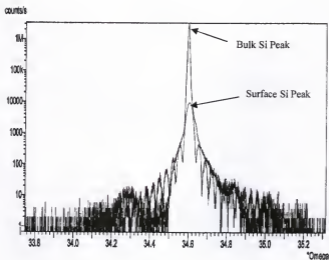


Figure 6-29. Comparison of (004) ω -2 θ rocking curves for 1600 Å SOI and bulk Si implanted with B⁺, 3.5 keV, $3 \times 10^{14} \text{ cm}^{-2}$. Anneals were performed at 900°C for 30 minutes. Oscillatory pattern belongs to SOI, while the high intensity peak is bulk Si.

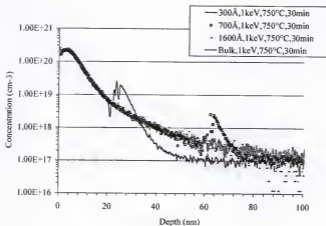


Figure 6-30. SIMS profiles of SOITEC and bulk Si materials implanted with B⁺, 1 keV, 3×10^{14} cm⁻². Anneals were 750°C for 30 minutes. Note depletion of B on surface Si side of interface, as well as pileup on BOX side.

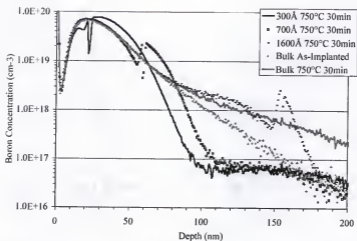


Figure 6-31. SIMS profiles of SOITEC and bulk Si materials implanted with B⁺, 6.5 keV, $3 \times 10^{14} \text{ cm}^{-2}$. Anneals were 750°C for 30 minutes.

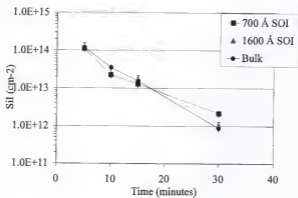


Figure 6-32. QTEM data for B^+ , 3.5 keV, $3 \times 10^{14} \text{ cm}^{-2}$ annealed at 750°C for various times. Note little difference in dissolution between SOI and bulk Si.

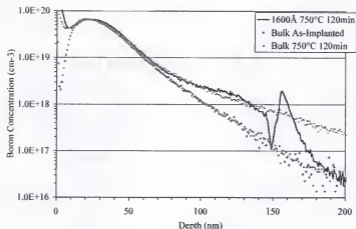


Figure 6-33. Comparison of TED behavior in 1600 Å SOI and bulk Si after implantation at B⁺, 6.5 keV, 3×10^{14} cm⁻². Anneals were performed at 750°C for 120 minutes. Note slight tail enhancement in 1600 Å SOI compared to bulk Si.

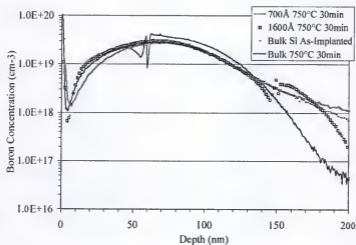


Figure 6-34. SIMS profiles of SOITEC and bulk Si materials implanted with B⁺, 19 keV, $3 \times 10^{14} \text{ cm}^{-2}$. Anneals were 750°C for 30 minutes.

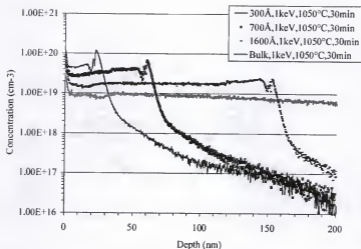


Figure 6-35. SIMS profiles of SOITEC and bulk Si materials implanted with B^+ , 1 keV, $3 \times 10^{14} \text{ cm}^{-2}$. Anneals were 1050°C for 30 minutes. Note box-shape profile after annealing SOI materials.

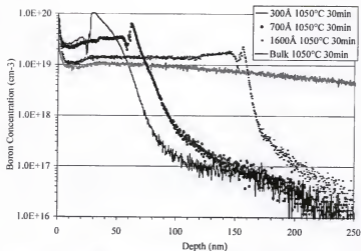


Figure 6-36. SIMS profiles of SOITEC and bulk Si materials implanted with B⁺, 6.5 keV, $3 \times 10^{14} \text{ cm}^{-2}$. Anneals were 1050°C for 30 minutes.

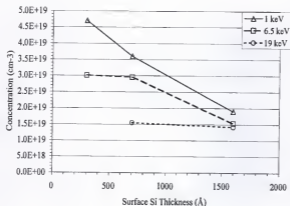


Figure 6-37. Retained concentration versus surface Si layer thickness for B⁺, 1 - 19 keV, 3×10^{14} cm⁻². Anneals were performed at 1050°C for 30 minutes. Concentrations were taken as the average concentration across the surface Si layer, while avoiding transient effects near interfaces.

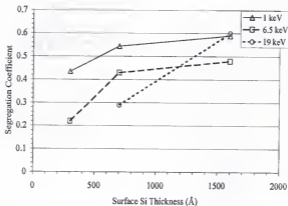


Figure 6-38. Segregation coefficients versus surface Si thickness after annealing at 1050°C for various times. Implants were B⁺, 1 keV, 6.5 keV, and 19 keV, with a dose of 3×10^{14} cm⁻².

CHAPTER 7 SUMMARY AND FUTURE WORK

7.1 Summary

This first part of this dissertation centered around understanding the effect of the surface Si/BOX interface on the evolution of Type I and II extended defects in SOI. It was shown that the behavior of the interface is extremely sensitive to the implant conditions used. $\{311\}$ defect evolution seemed to be affected the most by the presence of the buried interface, while dislocation loops were relatively impervious until significant as-implanted dose loss occurred. Simulation of $\{311\}$ defects in SOI is the subject of the following chapter. Distinction was also made between non-amorphizing and amorphizing loop evolution. For FD-SOI material, the evolution of loops was affected when an amorphizing dose was used due to the reduced proximity to the interface. Annealing ambient also appeared to play a role, as significant differences in OSF growth and shrinkage were observed between SOI and bulk Si, particularly at high temperatures.

A first model for $\{311\}$ defect evolution in SOI materials based on quantitative TEM measurements was also attempted. We demonstrate that current models are unable to accurately predict evolution of $\{311\}$ defects in SOI. This likely inhibits the nucleation of submicroscopic interstitial clusters (SMICs) in SOI, which serve as the seed for the $\{311\}$ defects. However, Law's model does account for the experimental observation of reduced defect size in SOI. Future models need to account less for interstitial recombination at interfaces and more on nucleation mechanisms.

The last studies discussed the characteristics of BIC formation in SOI and how they compare to bulk Si. Hall Effect data suggests a slight increase in BIC formation occurs in SOI compared to bulk Si at low temperatures and concentrations. These observations were supported by QTEM measurements of {311} defects. At higher concentrations and temperatures this effect seems to reverse itself. Truncation of the B profile by the surface Si/BOX interface appeared to increase the fraction of active B remaining in the surface Si layer. This was attributed to a reduction in the BIC population, but the influence of a shallow, vacancy-rich region near the surface could also play a role. HRXRD measurements were performed to determine the role of strain in the activation process. The substitutional B peak in bulk Si tended to shift towards the substrate peak as the thermal budget was increased. This is explained as delocalization of the B as the implant profile diffuses. Similar results were obtained for compressive stresses to the left of the surface Si or substrate peaks. Care must be taken when analyzing SOI rocking curves, particularly in the case of bonded SOI wafers. The presence of thickness fringes makes a direct comparison between SOI and bulk very difficult. Finally, the phenomena of TED and B segregation were addressed. Enhanced B diffusion in PD-SOI was observed for the case where {311} defects formed and the B concentration was low enough to observe tail diffusion. Increased interstitial transport to the surface Si/BOX interface appears to be responsible for a reduction in the segregation coefficient for thinner films. This effect was also seen at higher implant energies. These results imply that an enhancement in the dissolution rate of {311}s in SOI could lead directly to a reduction in the segregation coefficient of B in SOI.

7.2 Future Work

Although, these studies have provided a better understanding of ion implantation processes in SOI materials, much work can still be done to increase the knowledge in this area. Additional experiments are now proposed that would be beneficial to the SOI community.

7.2.1 Local Electrode Atom Probe (LEAP) for Monitoring Dopant Segregation in SOI

The potential to resolve impurities near the atomic level in 3-D and in the proximity of interfaces make LEAP instrumentation a viable alternative to SIMS [KEL00], particularly for SOI materials. As scaling of microelectronics continues closer to atomic dimensions, benefit can be reaped from the LEAPs ability to probe both vertically and laterally. Unfortunately, tedious sample preparation is required and only a limited sample volume ($\sim 10^9$ atoms) may be probed. Focused ion beam (FIB) milling could be used for fabricating microtips of SOI samples. This is due to its ability to resolve and micromachine the 10-100 nm diameter tip apex required. Samples also need to exhibit marginal conductivity in order to be analyzed. However, LEAP holds promise for resolving the pileup of impurities at the surface Si/BOX interface in SOI. Ideally, it should help alleviate some of the matrix effects that occur in SIMS profiles of SOI material.

LEAP relies on the principle of field emission for removing atoms from the surface of a conical/microtip specimen. A schematic of the LEAP geometry is shown in Fig. 7-1. The extraction electrode is brought close to the sample tip, since this requires lower extraction voltages to remove the atoms. This ionizes the atoms at the tip surface until they are removed. A secondary electrode is used to steer the ions towards a position sensitive mass spectrometer that records the location and time of impact. The process is continued and the tip eroded until the desired depth is reached. [KEL00]

7.2.2 Modification of Surface Potential Using a MOS Capacitor Structure

Another helpful experiment could involve the fabrication of a MOS capacitor structure, such as that shown in Fig. 7-2. Application of an electric field could be used to modify the potential at the Si/SiO₂ interface. If the potential could be changed, so that interstitials are attracted to the interface then it would prove that surface potential plays a key role in determining shallow profiles. The first step would consist of a shallow B implant with a dose high enough to produce extended defects upon annealing. A thin LTO (~10 – 20 nm) could then be deposited to serve as the dielectric material. This would be followed by a doped polysilicon deposition to serve as the top plate of the capacitor. A metal contacts would then be deposited to make contact from the voltage source to the top and bottom plates of the capacitor. The metal would need to be able to form a stable silicide at relatively high operating temperatures (700°C – 800°C). Platinum or nickel could be possible candidates for this process. However, Au and Al will not work because their eutectic temperatures are too low. All fabrication needs to be performed at low temperatures in order to prevent formation of the extended defects prior to annealing. Anneals would need to be performed in a specially designed furnace that could have electrodes extend far enough to make contact to the sample. A voltage bias would then be applied *in-situ* to alter the band bending at the interface. TEM could be used to investigate the evolution of the trapped interstitial population after annealing.

7.2.3 Critical Amorphization Depth in SOI

A fairly simple experiment could involve producing a number of amorphous layers of varying distance from the surface Si/BOX interface. The minimal distance between the amorphous-crystalline interface and surface Si/BOX interfaces for obtaining twin-free regrowth could then be determined. This would help establish how integrable SPE is with SOI fabrication techniques.

7.2.4 Concentration Threshold for BIC Formation in SOI

Another experiment could involve determining the threshold concentration for BIC formation in SOI compared to bulk Si. This could be done a couple of different ways. A series of B implants at varying doses could be done and the electrical activation monitored using Hall Effect. Once a significant drop in activation is observed, then the BIC threshold would have been reached. A somewhat cleaner experiment would involve implanting B at a variety of doses and then annealing at high temperature to produce box-shaped profiles, like those in Chapter 6. Si⁺ implantation could then be used to produce clusters by providing the necessary interstitial supersaturation. However, the dose loss of interstitials would need to be monitored to ensure that not too many are lost during the implant. Thus, these experiments would work best in PD-SOI.

7.2.5 N-Type Dopants in SOI

This dissertation focused specifically on B in SOI. Unfortunately, the literature remains scarce with regards to n-type dopant behavior in SOI. Experiments discussed above could each be applied to involve As, P, and Sb.

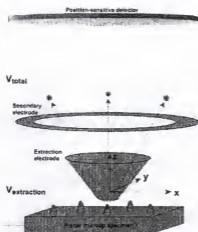


Figure 7-1. Schematic of LEAP constituents near a surface containing microtips for analysis.
From [KEL00].

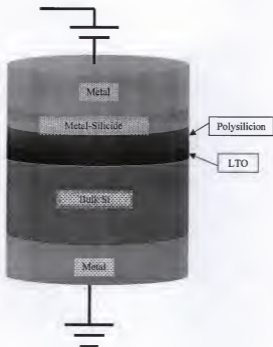


Figure 7-2. Schematic of MOS capacitor structure that could be used to alter surface potential at Si/SiO₂ interface.

APPENDIX A

QUANTITATIVE TEM FOR MEASURING TRAPPED INTERSTITIAL POPULATIONS

This Appendix describes the methodology for quantifying trapped interstitials within extended defects. Printing of a TEM negative is typically done at a total magnification of 150,000X. Defects are then marked on transparencies inside a specified area using an ultra-fine point marker. The area should be large enough so that quantification is not skewed. This is the case for small defect densities, where only a few defects are present. If the marked area is too small, the defect density will appear larger than it actually is. In order to distinguish among the different types of defects, only one type of defect should be marked at a time in a particular area. This allows for the number of trapped interstitials within a particular defect to be estimated. A total trapped interstitial number can then be estimated by summing the trapped interstitials within all defects.

The marked area is then scanned as a digital image at low resolution (e.g., 100-200 dpi). The image must then be analyzed using a imaging program, such as NIH Image, available for download at <http://rsb.info.nih.gov/nih-image/Default.html> [NIH04]. Resolution limits are first set by clicking on **Analyze⇒Set Scale** and entering the number of pixels per inch the marked image was scanned to. This is then usually converted to centimeters by changing the scale. The measurements to be made are selected by going to **Analyze⇒Options**. These are typically Area, Major Axis, and Minor Axis. Next, the image is converted to a binary image by selecting **Options⇒Threshold**. It is important to adjust threshold limits if they are too low. For example, all loops must be completely enclosed in order to be counted. This is done by adjusting the threshold bar appearing to the left of the image. If this does not work, then the pen

tool can be used to close the loops. Next, the particles are analyzed by selecting **Analyze⇒Analyze Particles**. The minimum and maximum pixel size can then be set to exclude dust particles that might appear in the scanned image. **Include hole interiors** should also be selected so that the total area is measured. **Analyze⇒Measure** and **Analyze⇒Show Results** quantify the image and the results can then be saved.

A spreadsheet program, such as Microsoft Excel, can then be used to analyze the data from NIH Image. For dislocation loops and oxidation stacking faults, the concentration of trapped interstitials is calculated as

$$C_{Loop} = \frac{C_{\{111\}} \Sigma A_{Loop}}{A_{Count} M^2} \quad (A.1)$$

$$C_{OSF} = \frac{C_{\{111\}} \Sigma A_{OSF}}{A_{Count} M^2} \quad (A.2)$$

where A_{Loop} is the total area enclosed by loops within the counted area, A_{OSF} the total area enclosed by OSFs, $C_{\{111\}}$ the areal packing density of atoms along the $\{111\}$ plane ($\sim 1.5 \times 10^{15} \text{ cm}^{-2}$), A_{Count} the total area counted, and M the magnification. The loop diameter can be estimated from the area enclosed by a single loop according to

$$L_{Loop} = \sqrt{\frac{4A_{Loop}}{\pi}} \quad (A.3)$$

with quantities defined previously. The length and width of OSFs can be extracted directly from the NIH Image data and dividing by the magnification. Defect density is calculated as

$$D_{Loop} = \frac{N_{Loop}}{A_{Count} M^2} \quad (A.4)$$

where N is the number of defects within the area counted. For $\{311\}$ defects, the concentration of trapped interstitials is given as

$$C_{\{311\}} = \frac{N_{\{311\}} \Sigma L_{\{311\}}}{A_{\text{Count}} M^2} \quad (\text{A.5})$$

where $L_{\{311\}}$ is the length of the $\{311\}$ defect and $N_{\{311\}}$ the number of interstitials per unit length (~26 interstitials per nm). $\{311\}$ size is simply the major axis divided by the magnification.

$\{311\}$ density is calculated the same as loops.

APPENDIX B FLOOPS CODE FOR SIMULATION OF {311} DEFECTS IN SOI

The FLOOPS code used to simulate {311} defect evolution is shown in this Appendix.

```
#math diffuse dim=1 umf none triplet
pdbSetSwitch Si I DiffModel Numeric
pdbSetSwitch Si V DiffModel Numeric
# Int diffusion after Ural et al. PRL 83 (1999) p3454
set k 1.0e-4
pdbSetDouble Silicon Int D0 [format {[Arrhenius [expr 5.54e-3 * %s] 0.85]} $k]
pdbSetDouble Silicon Int Cstar [format {[Arrhenius [expr 5.0e22*exp(10.2) / %s] 3.83]}
$kl]

pdbSetDouble Silicon Vac D0 {[Arrhenius 1.756e-3 0.493]}
pdbSetDouble Silicon Vac Cstar {[Arrhenius [expr 5.0e22*exp(12.8)] 4.367]}
#originally expr 2.0*...
pdbSetDouble Silicon Smic6 Bind {[expr 0.65*[Arr 2.9e-4 -1.8] * [pdbGetDouble Si Int
Cstar] ]}
pdbSetDouble Silicon Smic8 Bind {[expr 0.65*[Arr 1.8e-3 -1.55] * [pdbGetDouble Si Int
Cstar] ]}
#originally expr 1.6*...
pdbSetDouble Silicon C311 Bind1 {[expr 0.4*[Arr 7.5e-2 -0.94] * [pdbGetDouble Si Int
Cstar] ]}
pdbSetDouble Silicon C311 Bind12 {[expr 0.5*[Arr 7.5e-2 -0.94] * [pdbGetDouble Si Int
Cstar] ]}
#decent with expr 10.0+reduced Kfl for C311
pdbSetDouble Silicon Smic6 Kfl {[expr 2.0*[DiffLimit Silicon Int 0.0]]}
pdbSetDouble Silicon Smic6 Kfl2 {[expr 2.0*[DiffLimit Silicon Int 0.2] ]}
#changed from 1.0 to check
#decent with expr 10.0+reduced Kfl for C311
pdbSetDouble Silicon Smic8 Kfl {[expr 2.0*[DiffLimit Silicon Int 0.0]]}
pdbSetDouble Silicon C311 Kn12 {[expr 0.25*[DiffLimit Silicon Int 0.35] ]}
pdbSetDouble Silicon C311 Kfl {[expr 0.25*[DiffLimit Si Int 0.0] ]}
pdbSetDouble Silicon C311 Kfl2 {[expr 0.25*[DiffLimit Si Int 0.0] ]}
pdbSetDouble Si C311 Rangel 1.0
pdbSetDouble Si C311 Rangel2 3.0
pdbSetDouble Silicon C311 CombRate {0.7}
pdbSetDouble Silicon C311 NSize 4.0
solution name=Smic6 add solve !neg
```

```

solution name=Smic8 add solve !neg
pdbSetString Si C311 InitProc DefectInit
pdbSetString Si D311 InitProc DefectInit
pdbSetString Si C311 EquationProc 311Eqn
pdbSetString Si Smic6 EquationProc ClusterEqn

```

```

# parameters Smic6 KnI2, C311 KnI2 and I2 Ksurf are interlocked,
#     too little dose of 311 ... 0.4, 0.6, 0.4
#     a bit too long dissolution ... 0.6, 0.8, 0.8
#small smics dissolve too fast, 311 still do not last long enough ... 0.3, 0.5, 0.4
#     a bit too high 311 Bind1 ... 0.4, 0.6, 0.5
#     next ... 0.45, 0.6, 0.55
set IV "IV0.0"
#Initialize Native Oxide/Surface Silicon Parameters
#This value was originally set for Ea = 0 for bulk
#originally expr 1.0...
pdbSetDouble Oxide_Silicon Interstitial Ksurf {[expr 1.0*[SurfDiffLimit Oxide_Silicon
Silicon I 0.0]]}
#pdbSetBoolean Oxide_Silicon Interstitial segregation {0}
#pdbSetDouble Oxide_Silicon Interstitial Scale {[Arrhenius 4.7e-2 2.0]}
#pdbSetDouble Oxide_Silicon Interstitial Inj {[Arrhenius 5.56e-3 -0.784]}
#change from 1e14,2.8e12 for bulk
pdbSetDouble Oxide_Silicon Interstitial KinkSite {5.0e11}
#pdbSetDouble Oxide_Silicon Interstitial Krat {0.0}
#pdbSetDouble Oxide_Silicon Interstitial Trn {0.0}
#pdbSetBoolean Oxide_Silicon Interstitial time.inj {0}
#pdbSetDouble Oxide_Silicon Interstitial theta {[ComputeTheta]}
#pdbSetDouble Oxide_Silicon Interstitial seg {1.0}
#pdbSetBoolean Oxide_Silicon Interstitial recomb {1}
#Ktrap value was originally expr 10.0* ...
#pdbSetDouble Oxide_Silicon Interstitial Ktrap {[expr 10.0*[SurfDiffLimit
Oxide_Silicon Si Int 0]]}
#pdbSetBoolean Oxide_Silicon Interstitial growth.inj {1}
#pdbSetDouble Oxide_Silicon Interstitial vmole {5e22}
#pdbSetDouble Oxide_Silicon Interstitial Gpow {0.0}
#pdbSetBoolean Oxide_Silicon Vacancy segregation {0}
#pdbSetDouble Oxide_Silicon Vacancy Scale {[Arrhenius 1.87 2.14]}
#pdbSetDouble Oxide_Silicon Vacancy Kpow {0.0}
#pdbSetDouble Oxide_Silicon Vacancy injection {0.0}
#Originally 1e5
pdbSetDouble Oxide_Silicon Vacancy KinkSite {1.0e5}
#pdbSetDouble Oxide_Silicon Vacancy Krat {0.0}
#This value did not originally have expr 100.0
#pdbSetDouble Oxide_Silicon Vacancy Ksurf {[SurfDiffLimit Oxide_Silicon Si Vac 0]}
#pdbSetDouble Oxide_Silicon Vacancy Trn {0.0}

```

```

#pdbSetBoolean Oxide_Silicon Vacancy time.inj {0}
#pdbSetDouble Oxide_Silicon Vacancy theta {0.0}
#pdbSetDouble Oxide_Silicon Vacancy seg {1.0}
#pdbSetBoolean Oxide_Silicon Vacancy recomb {1}
#pdbSetDouble Oxide_Silicon Vacancy Ktrap {[expr 10.0*[SurfDiffLimit Oxide_Silicon
Si Vac 0.0]]}
#pdbSetBoolean Oxide_Silicon Vacancy growth.inj {0}
#pdbSetDouble Oxide_Silicon Vacancy vmole {5e22}
#pdbSetDouble Oxide_Silicon Vacancy Gpow {0.0}
#pdbSetDouble Oxide_Silicon I2 KinkSite {1.0e13}
#pdbSetDouble Oxide_Silicon I2 Ksurf {[expr 1.0*[SurfDiffLimit Oxide_Silicon Silicon
I2 0.0]]}
set WinTitle "Type plot title here"
#Initialize Nitride (Buried Oxide)/Silicon (Surface Silicon) Interface Parameters
#pdbSetBoolean Nitride_Silicon Interstitial segregation {0}
#pdbSetDouble Nitride_Silicon Interstitial Scale {[Arrhenius 4.7e-2 2.0]}
#pdbSetDouble Nitride_Silicon Interstitial Inj {[Arrhenius 5.56e-3 -0.784]}
#pdbSetDouble Nitride_Silicon Interstitial KinkSite {2.75e12}
#pdbSetDouble Nitride_Silicon Interstitial Krat {0.0}
#Originally at 0
#pdbSetDouble Nitride_Silicon Interstitial Ksurf {[expr 1.0*[SurfDiffLimit
Oxide_Silicon Si Int 0.0]]}
#pdbSetDouble Nitride_Silicon Interstitial Trm {0.0}
#pdbSetBoolean Nitride_Silicon Interstitial time.inj {0}
#pdbSetDouble Nitride_Silicon Interstitial theta {[ComputeTheta]}
#pdbSetDouble Nitride_Silicon Interstitial seg {1.0}
#pdbSetBoolean Nitride_Silicon Interstitial recomb {1}
#pdbSetDouble Nitride_Silicon Interstitial Ktrap {[expr 0.0*[SurfDiffLimit
Oxide_Silicon Si Int 0.0]]}
#pdbSetBoolean Nitride_Silicon Interstitial growth.inj {1}
#pdbSetDouble Nitride_Silicon Interstitial vmole {5e22}
#pdbSetDouble Nitride_Silicon Interstitial Gpow {0.0}
#pdbSetBoolean Nitride_Silicon Vacancy segregation {0}
#pdbSetDouble Nitride_Silicon Vacancy Scale {[Arrhenius 1.87 2.14]}
#pdbSetDouble Nitride_Silicon Vacancy Kpow {0.0}
#pdbSetDouble Nitride_Silicon Vacancy injection {0.0}
#Originally 1e5
#pdbSetDouble Nitride_Silicon Vacancy KinkSite {1.0e5}
#pdbSetDouble Nitride_Silicon Vacancy Krat {0.0}
#pdbSetDouble Nitride_Silicon Vacancy Ksurf {[SurfDiffLimit Oxide_Silicon Si Vac
0.0]}
#pdbSetDouble Nitride_Silicon Vacancy Trm {0.0}
#pdbSetBoolean Nitride_Silicon Vacancy time.inj {0}
#pdbSetDouble Nitride_Silicon Vacancy theta {0.0}
#pdbSetDouble Nitride_Silicon Vacancy seg {1.0}
#pdbSetBoolean Nitride_Silicon Vacancy recomb {1}

```

```

#pdbSetDouble Nitride_Silicon Vacancy Ktrap {[expr 0.0*[SurfDiffLimit Oxide_Silicon
Si Vac 0.0]]}
#pdbSetBoolean Nitride_Silicon Vacancy growth.inj {0}
#pdbSetDouble Nitride_Silicon Vacancy vmole {5e22}
#pdbSetDouble Nitride_Silicon Vacancy Gpow {0.0}
pdbSetDouble Nitride_Silicon I2 KinkSite {0.0e15}
pdbSetDouble Nitride_Silicon I2 Ksurf {[expr 0.0*[SurfDiffLimit Oxide_Silicon Silicon
I2 0.0]]}
#pdbSetDouble Nitride_Silicon V2 KinkSite {1.0e6}
#pdbSetDouble Nitride_Silicon V2 Ksurf {[expr 1.0*[SurfDiffLimit Oxide_Silicon
Silicon V2 0.0]]}
#pdbSetDouble Nitride_Silicon V2 Ktrap {[expr 0.0*[SurfDiffLimit Oxide_Silicon Si
Vac 0.0]]}

```

LIST OF REFERENCES

- [ADA98] A. O. Adan, T. Naka, A. Kagisawa, H. Shimizu, Proceedings IEEE International SOI Conference, 1998, p. 9.
- [ADE03] J. Adey, J. P. Goss, R. Jones, and P. R. Briddon, Phys. Rev. B **67**, 245325-1 (2003).
- [AGA95] A. M. Agarwal and S. T. Dunham, J. Appl. Phys. **78**, 5313 (1995).
- [AGA97a] A. Agarwal, T. E. Haynes, D. J. Eaglesham, H. -J. Gossmann, D. C. Jacobson, J. M. Poate, and Yu. E. Erokhin, Appl. Phys. Lett. **70**, 3332 (1997).
- [AGA97b] A. Agarwal, H. -J. Gossmann, D. J. Eaglesham, L. Pelaz, D. C. Jacobson, T. E. Haynes, and Yu. E. Erokhin, Appl. Phys. Lett. **71**, 3141 (1997).
- [AGA99] A. Agarwal, H. -J. Gossmann, D. J. Eaglesham, S. B. Herner, A. T. Fiory, and T. E. Haynes, Appl. Phys. Lett. **74**, 2435 (1999).
- [AHI98] T. Ahilea, E. Zolotoyabko, J. Härtwig, M. Ohler, and E. Prieur, J. Appl. Phys. **84**, 6076 (1998).
- [AHN87] S. T. Ahn, P. B. Griffin, J. D. Shott, J. D. Plummer, and W. A. Tiller, J. Appl. Phys. **62**, 4745 (1987).
- [AHN89] S. T. Ahn, H. W. Kennel, W. A. Tiller, and J. D. Plummer, J. Appl. Phys. **65**, 2957 (1989).
- [ALE98] O. V. Aleksandrov and A. N. Afonin, Semiconductors **32**, 15 (1998).
- [ANT79] D. A. Antoniadis, M. Rodoni, and R. W. Dutton, J. Electrochem. Soc. **126**, 1939 (1979).
- [ARA97] N. Arai, S. Takeda, and M. Kohyama, Phys. Rev. Lett. **78**, 4265 (1997).
- [ATA60] M. M. Atalla and E. Tannenbaum, Bell Sys. Tech. J. **39**, 933 (1960).
- [AVC02] I. Avci, Ph. D. Dissertation, University of Florida (2002).
- [AVC04] I. Avci, M. E. Law, E. Kuryliw, A. F. Saavedra, and K. S. Jones, J. Appl. Phys. **95**, 2452 (2004).
- [AZI01] M. J. Aziz, Materials Sci. in Semiconductor Processing **4**, 397 (2001).

- [BAL88] P. Balk, *Materials Science Monographs*, 32, *The Si-SiO₂ System*, (Elsevier, New York, NY, 1988), pp. 77-123.
- [BAR01] J. Bardeen and W. Brattain, "Three-Electrode Circuit Element Utilizing Semiconductive Materials," U.S. Patent 2,524,035.
- [BEN97] J. L. Benton, S. Libertino, P. Kringhoj, D. J. Eaglesham, J. M. Poate, and S. Coffa, *J. Appl. Phys.* **82**, 120 (1997).
- [BEN98] J. L. Benton, K. Halliburton, S. Libertino, D. J. Eaglesham, and S. Coffa, *J. Appl. Phys.* **84**, 4749 (1998).
- [BOC02] C. Bocchi, F. Germini, E. Kh. Mukhamedzhanov, L. Nasi, V. Privitera, and C. Spinella, *Mat. Sci. Eng. B* **91-92**, 457 (2002).
- [BOH13] N. Bohr, *Phil. Mag.* **25**, 10 (1913).
- [BOR92] L. Borucki, *Proc. NUPAD IV* (1992), 27.
- [BRU92] C. R. Brundle, C. A. Evans, Jr., and S. Wilson, *Encyclopedia of Materials Characterization*, (Butterworth-Heinemann, Boston, MA, 1992) pp. 40-41.
- [BRU96] M. Bruehl, *Nucl. Instrum. Methods in Phys. Res. B* **108**, 313 (1996).
- [BRU97] M. Bruehl, B. Aspar and A. -J. Auberton-Herve, *Jpn. J. Appl. Phys.* **36**, 1636 (1997).
- [BUL78] C. Bull, P. Ashburn, G. R. Booker, and K. H. Nicholas, *Solid State Electronics* **22**, 95 (1978).
- [CAT98] M. J. Caturia, M. D. Johnson, and T. D. de la Rubia, *Appl. Phys. Lett.* **72**, 2736 (1998).
- [CEL86] G. K. Celler, P. L. F. Hemment, K. W. West, and J. M. Gibson, *Appl. Phys. Lett.* **48**, 532 (1986).
- [CEL89a] G. K. Celler and L. E. Trimble, *Appl. Phys. Lett.* **54**, 1427 (1989).
- [CEL89b] G. K. Celler and L. E. Trimble, *Appl. Surf. Science* **39**, 245 (1989).
- [CHA84] G. Charitat and A. Martinez, *J. Appl. Phys.* **55**, 2869 (1984).
- [CHA87] P. -H. Chang and B. -Y. Mao, *Appl. Phys. Lett.* **50**, 152 (1987).
- [CHA97] E. Chason, S. T. Picraux, J. M. Poate, J. O. Borland, M. I. Current, T. Diaz de la Rubia, D. J. Eaglesham, O. W. Holland, M. E. Law, C. W. Magee, J. W. Mayer, J. Melngailis, and A. F. Tasch, *J. Appl. Phys.* **81**, 6513 (1997).
- [CHI97] Y. Chiang, D. P. Birnie III, and W. D. Kingery, *Physical Ceramics*, (John Wiley & Sons, New York, NY, 1997), pp. 83-84.

- [CLA03] A. Claverie, B. Colombeau, B. De Mauduit, C. Bonafos, X. Hebras, G. Ben Assayag, and F. Cristiano, *Appl. Phys. A* **76**, 1025 (2003).
- [COF00] S. Coffa, S. Libertino, C. Spinella, *Appl. Phys. Lett.* **76**, 321 (2000).
- [COH99] G. M. Cohen, P. M. Mooney, E. C. Jones, K. K. Chan, P. M. Solomon, and H-S. P. Wong, *Appl. Phys. Lett.* **75**, 787 (1999).
- [COH03] G. M. Cohen, P. M. Mooney, H. Park, C. Cabral, Jr., and E. C. Jones, *J. Appl. Phys.* **93**, 245 (2003).
- [COL97] J. P. Colinge, *Silicon-on-Insulator Technology: Materials to VLSI*, 2nd ed. (Kluwer Academic, Boston, MA, 1997), pp. 1-4.
- [COL98] J. P. Colinge, *MRS Bulletin* **23**, 16 (1998).
- [CON96] J. F. Conley Jr., P. M. Lenahan and B. D. Wallace, *IEEE Trans. Nucl. Sci.* **43**, 2635 (1996).
- [COW99a] N. E. B. Cowern, G. Mannino, P. A. Stolk, F. Roozeboom, H. G. A. Huizing, J. G. M. van Berkum, F. Cristiano, and A. Claverie, *Phys. Rev. Lett.* **82**, 4460 (1999).
- [COW99b] N. E. B. Cowern, D. Alquier, M. Omri, A. Claverie, and A. Nejim, *Nucl. Instrum. Meth. Phys. Res. B* **148**, 257 (1999).
- [COW99c] N. E. B. Cowern, M. J. J. Theunissen, F. Roozeboom, and J. G. M. van Berkum, *Appl. Phys. Lett.* **75**, 181 (1999).
- [COW00] N. E. B. Cowern and C. S. Rafferty, *MRS Bull.* **25**, 39 (2000).
- [CRO94a] S. W. Crowder, P. B. Griffin, C. J. Hsieh, G. Y. Wei, J. D. Plummer, and L. P. Allen, *Appl. Phys. Lett.* **64**, 3264 (1994).
- [CRO94b] S. W. Crowder, C. J. Hsieh, P. B. Griffin, and J. D. Plummer, *J. Appl. Phys.* **76**, 2756 (1994).
- [CRO95] S. W. Crowder, Ph. D. Dissertation, Stanford University (1995).
- [CRI03] F. Cristiano, X. Hebras, N. Cherkashin, A. Claverie, W. Lerch, and S. Paul, *Appl. Phys. Lett.* **83**, 5407 (2003).
- [DAB02] J. Dabrowski, H. J. Müssig, V. Zavodinsky, R. Baierle, and M. J. Caldas, *Phys. Rev. B* **65**, 245305-1 (2002).
- [DEA65a] B. E. Deal and A. D. Grove, *J. Appl. Phys.* **36**, 3770 (1965).
- [DEA65b] B. E. Deal, A. S. Grove, E. H. Snow, and C. T. Sah, *J. Electrochem. Soc.* **112**, 308 (1965).

- [DEH93] R. T. DeHoff, *Thermodynamics in Materials Science*, (McGraw-Hill, New York, NY, 1993), pp. 160-203.
- [DEV03] K. Dev, M. Y. L. Jung, R. Gunawan, R. D. Braatz, and E. G. Seebauer, *Phys. Rev. B* **68**, 195311 (2003).
- [DEV04] K. Dev and E. G. Seebauer, *Surface Science* **550**, 185 (2004).
- [DOK02] O. Dokumaci, P. Ronsheim, A. Ajmera, J. Mayo, R. Young, C. Heenan, D. Uriarte, K. P. Muller, and R. J. Miller, Presented at 2002 Mat. Res. Soc. Spring Meeting, San Francisco, CA.
- [DOU87] D. H. Douglas-Hamilton, R. P. Dolan and H. E. Friedman, *Nucl. Instrum. Methods in Phys. Res. B* **21**, 158 (1987).
- [DUF03] R. Duffy, V. C. Venezia, A. Heringa, T. W. T. Hüsken, M. J. P. Hopstaken, N. E. B. Cowern, P. B. Griffin, and C. C. Wang, *Appl. Phys. Lett.* **82**, 3647 (2003).
- [DUN92] S. T. Dunham, *J. Appl. Phys.* **70**, 685 (1992).
- [EAG94] D. J. Eaglesham, P. A. Stolk, H.-J. Gossmann, and J. M. Poate, *Appl. Phys. Lett.* **65**, 2305 (1994).
- [EAG96] D. J. Eaglesham, A. Agarwal, T. E. Haynes, H. -J. Gossmann, D. C. Jacobson, and J. M. Poate, *Nucl. Instrum. And Methods B* **120**, 1 (1996).
- [EAG00] D. J. Eaglesham, V. C. Venezia, H. -J. Gossmann, and A. Agarwal, *J. Electron Microscopy* **49**, 293 (2000).
- [EAR02] S. K. Earles, Ph. D. Dissertation, University of Florida (2002).
- [EHR94] P. Ehrhart, *J. Nuclear Materials* **216**, 170 (1994).
- [FAH89] P. M. Fahey, P. B. Griffin, and J. D. Plummer, *Rev. Mod. Phys.* **61**, 289 (1989).
- [FAI78] R. B. Fair and J. C. C. Tsai, *J. Electrochem. Soc.* **125**, 2050 (1978).
- [FAI81] R. B. Fair in *Applied Solid State Science*, edited by R. Wolfe (Academic Press, New York, NY, 1981), pp. 1-102.
- [FEW93] P. F. Fewster, *Semicond. Sci. Technol.* **8**, 1915 (1993).
- [FLA95] D. Flandre, *Mat. Sci. and Eng., B.* **29**, 7 (1995).
- [FLO01] FLOOPS, University of Florida (2001).
- [FRA02] D. J. Frank, *IBM J. Res. And Dev.* **46**, 235 (2002).

- [GAM98] F. Gamiz, J. A. Lopez-Villanueva, J. B. Roldan, J. E. Carceller, and P. Cartujo, *IEEE Trans. Electron Devices* **45**, 1122 (1998).
- [GAM01a] F. Gamiz and M. V. Fischetti, *J. Appl. Phys.* **89**, 5478 (2001).
- [GAM01b] F. Gamiz, J. B. Roldan, J. A. Lopez-Villanueva, P. Cartujo-Cassinello, J. E. Carceller, P. Cartujo, and F. Jimenez-Molinos, *Solid-State Electronics* **45**, 613 (2001).
- [GAV76] S. D. Gavazza and D. M. Barnett, *J. Mech. Phys. Solids* **24**, 171 (1976).
- [GEN97] A. H. Gencer and S. T. Dunham, *J. Appl. Phys.* **81**, 631 (1997).
- [GIL91] M. D. Giles, *J. Electrochem. Soc.* **138**, 1160 (1991).
- [GIL94] L. F. Giles, C. D. Marsh, A. Nejmi, P. L. F. Hemment, and G. R. Booker, *Nucl. Instrum. Meth. Phys. Res. B* **84**, 242 (1994).
- [GIL99a] L. F. Giles, Y. Kunii, and K. Izumi, *J. Electronic Mat.* **28**, 13 (1999).
- [GIL99b] L. F. Giles and Y. Kunii, *J. Electronic Mat.* **28**, 372 (1999).
- [GOL86] E. Goldstein, *Berlin Zitz. Ber.* **39**, 691 (1886).
- [GOS95] H. -J. Gossmann, C. S. Rafferty, F. C. Unterwald, T. Boone, T. K. Mogi, M. O. Thompson, and H. S. Luftman, *Appl. Phys. Lett.* **67**, 1558 (1995).
- [GRI87] P. B. Griffin, S. T. Ahn, G. W. Tiller, and J. D. Plummer, *Appl. Phys. Lett.* **51**, 115 (1987).
- [GRO64a] A. S. Grove, O. Leistiko, and C. T. Sah, *J. Appl. Phys.* **35**, 2695 (1964).
- [GRO64b] A. S. Grove, O. Leistiko, and C. T. Sah, *J. Phys. Chem. Solids* (1964).
- [GRO65] A. S. Grove, A. Roder, and C. T. Sah, *J. Electrochem. Soc.* **36**, 802 (1965).
- [GUI92] N. Guillemot, D. Tsoukalas, C. Tsamis, J. Margail, and A. M. Papon, *J. Appl. Phys.* **71**, 1713 (1992).
- [HAL79] E. H. Hall, *J. Mathematics* **2**, 287 (1879).
- [HAN02] A. Hand, *Semiconductor International*, **25** (2002).
- [HAY80a] T. Hayashi, S. Maeyama and S. Yoshi, *Jpn. J. Appl. Phys.* **19**, 1111 (1980).
- [HAY80b] T. Hayashi, H. Okamoto and Y. Homma, *Jpn. J. Appl. Phys.* **19**, 1005 (1980).
- [HAY00] T. E. Haynes, *MRS Bulletin* **25**, 14 (2000). [see articles therein]

- [HEM83] P. L. F. Hemment, E. Maydell-Ondrusz, K. G. Stephens, J. Butcher, D. Ioannou, J. Alderman, Nucl. Instrum. And Methods 209/210, 157 (1983).
- [HER98] S. B. Herner, H.-J. Gossmann, L. P. Pelaz, G. H. Gilmer, M. Jaraiz, D. C. Jacobson, and D. J. Eaglesham, J. Appl. Phys. 83, 6182 (1998).
- [HIR99] Y. Hirano, S. Maeda, W. Fernandez, T. Iwamatsu, Y. Yamaguchi, S. Maegawa, and T. Nishimura, Jpn. J. Appl. Phys. 38, 2487 (1999).
- [HOB97] G. Hobler, C. S. Rafferty, and S. Senkader, Proc. Intl. Conf. Simulation of Semiconductor Processes and Devices, 73 (1997).
- [HOL83] G. Hollinger and F. J. Himpsel, Appl. Phys. Lett. 44, 93 (1983).
- [HOL84] O. W. Holland, T. P. Sjoreen, D. Fathy, and J. Narayan, Appl. Phys. Lett. 45, 1081 (1984).
- [HOL88] O. W. Holland, C. W. White, and S. J. Pennycook, J. Mat. Res. 3, 898 (1988).
- [HOV96] H. J. Hovel, Proceedings IEEE SOI Conf., 1 (1996).
- [HUA99] M. B. Huang and I. V. Mitchell, J. Appl. Phys. 85, 174 (1999).
- [HUM01] R. E. Hummel, *Electronic Properties of Materials*, 3rd ed. (Springer-Verlag, New York, NY, 2001), pp. 124-125.
- [HUS74] S. M. Hu, J. Appl. Phys. 45, 1567 (1974).
- [HUS75] S. M. Hu, Appl. Phys. Lett. 27, 165 (1975).
- [HUS85a] S. M. Hu, J. Appl. Phys. 57, 1069 (1985).
- [HUS85b] S. M. Hu, J. Appl. Phys. 57, 4527 (1985).
- [HUS91] S. M. Hu, J. Appl. Phys. 70, R53 (1991).
- [HUS94] S. M. Hu, Mat. Sci. Eng R 13, 105 (1994).
- [HWA03] G. S. Hwang and W. A. Goddard, Appl. Phys. Lett. 83, 1047 (2003).
- [IAC98a] F. Iacona, V. Raineri, F. La Via, and E. Rimini, J. Vac. Sci. Technol. B 16, 619 (1998).
- [IAC98b] F. Iacona, V. Raineri, F. La Via, A. Terrasi, and E. Rimini, Phys. Rev. B 58, 10990 (1998).
- [IBI03] IBIS website, <http://www.ibis.com>, 12/31/02.
- [IBM03] IBM website, <http://www.ibm.com>, 12/31/02.

- [IZU78] K. Izumi, M. Doken, and H. Arivoshi, *Electronics Lett.* **14**, 593 (1978).
- [IZU91] K. Izumi, *Vacuum* **42**, 333 (1991).
- [IZU98] K. Izumi, *MRS Bulletin* **23**, 20 (1998).
- [JAE02] R. C. Jaeger, *Introduction to Microelectronic Fabrication*, 2nd ed. (Prentice Hall, Upper Saddle River, NJ, 2002), p. 51.
- [JAI02] S. C. Jain, W. Schoenmaker, R. Lindsay, P. A. Stolk, S. Decoutere, M. Willander, and H. E. Maes, *J. Appl. Phys.* **91**, 8919 (2002).
- [JAU85] C. Jaussaud, J. Stoemenos, J. Margail, M. Dupuy, B. Blanchard, M. Bruel, *Appl. Phys. Lett.* **46**, 1064 (1985).
- [JON88] K. S. Jones, S. Prussin, and E. R. Weber, *Appl. Phys. A* **45**, 1 (1988).
- [JON96] K. S. Jones, R. G. Elliman, M. M. Petravic, and P. Kringhoj, *Appl. Phys. Lett.* **68**, 3111 (1996).
- [JON98] E. C. Jones and E. Ishida, *Mat. Sci. and Eng.*, **R. 24**, 1 (1998).
- [JUN04] M. Y. L. Jung, R. Gunawan, R. D. Braatz, and E. G. Seebauer, *J. Appl. Phys.* **95**, 1134 (2004).
- [KAL03] R. Kalyanaraman, V. C. Venezia, L. Pelaz, T. E. Haynes, H. -J. L. Gossmann, and C. S. Rafferty, *Appl. Phys. Lett.* **82**, 215 (2003).
- [KAS98] R. Kasnavi, P. Pianetta, Y. Sun, R. Mo, P. B. Griffin, and J. D. Plummer, *Tech. Dig. IEDM*, 721 (1998).
- [KAS00] R. Kasnavi, P. B. Griffin, and J. D. Plummer, *MRS Symp. Proc.* **610**, (2000).
- [KEL00] T. F. Kelly and D. J. Larson, *Materials Characterization* **44**, 59 (2000).
- [KIL01] J. Kilby, "Miniature Semiconductor Integrated Circuit", U.S. Patent 3,115,581.
- [KIM98] S. Kimura and A. Ogura, *Jpn. J. Appl. Phys.* **37**, 1282 (1998).
- [KIM00] J. Kim, F. Kirchhoff, J. W. Wilkins, and F. S. Khan, *Phys. Rev. Lett.* **84**, 503 (2000).
- [KIN03a] A. C. King, A. F. Gutierrez, A. F. Saavedra, K. S. Jones, and D. F. Downey, *J. Appl. Phys.* **93**, 2449 (2003).
- [KIN03b] A. C. King, K. S. Jones, A. F. Saavedra, and D. F. Downey, *Ultra Shallow Junctions Symp. Proc.*, 447 (2003).
- [KLA91] J. G. E. Klappe and P. F. Fewster, *J. Appl. Cryst.* **27**, 103 (1994).

- [KOH99] M. Kohyama and S. Takeda 60, 8075 (1999).
- [LAM03] E. Lampin, F. Cristiano, Y. Lamrani, A. Claverie, B. Colombeau, and N. E. B. Cowern, *J. Appl. Phys.* **94**, 7520 (2003).
- [LAN86] E. Landi and S. Solmi, *Sol. State Electronics* **29**, 1181 (1986).
- [LAW91] M. E. Law, *IEEE Tran. Comp. Aided Design* **10**, 1125 (1991).
- [LAW96] M. E. Law and K. S. Jones, *Electrochem Soc. Proc.* **96-4**, 374 (1996).
- [LAW98] M. E. Law, Y. M. Haddara, and K. S. Jones, *J. Appl. Phys.* **84**, 3555 (1998).
- [LAW00] M. E. Law and K. S. Jones, *Tech. Dig. IEDM*, 511 (2000).
- [LEN00] T. J. Lenosky, B. Sadigh, S. K. Theiss, M. J. Caturia, and T. D. de la Rubia, *Appl. Phys. Lett.* **77**, 1834 (2000).
- [LIB01] S. Libertino, S. Coffa, and J. L. Benton, *Phys. Rev. B* **63**, 195206-1 (2001).
- [LIJ98] J. Li and K. S. Jones, *Appl. Phys. Lett.* **73**, 3748 (1998).
- [LIJ99] J. Li, P. Keys, J. Chen, M. E. Law, K. S. Jones, and C. Jasper, *Mat. Res. Soc. Symp. Proc.* **568**, 175 (1999).
- [LIL26] J. E. Lilienfield, "Method and Apparatus for Controlling Electric Currents," U.S. Patent 1,745,175.
- [LIL01] A. D. Lilak, Ph. D. Dissertation, University of Florida (2001).
- [LIL02] A. D. Lilak, M. E. Law, L. Radic, K. S. Jones, and M. Clark, *Appl. Phys. Lett.* **81**, 826 (2002).
- [LIM95] D. R. Lim, C. S. Rafferty, and F. P. Klemens, *Appl. Phys. Lett.* **67**, 2302 (1995).
- [LIN04] Central X-ray Facility at Univ. Tenn. Website, <http://web.utk.edu/~xling/main>, 6/15/04.
- [LIU96] J. Liu, Ph. D. Dissertation, University of Florida (1996).
- [LIU00] X. Y. Liu, W. Windl, and M. P. Masquelier, *Appl. Phys. Lett.* **77**, 2018 (2000).
- [LUO01] W. Luo and P. Clancy, *J. Appl. Phys.* **89**, 1596 (2001).
- [LUZ93] Z. H. Lu, M. J. Graham, D. T. Jiang, and K. H. Tan, *Appl. Phys. Lett.* **63**, 2941 (1993).
- [LUZ95] Z. H. Lu, M. J. Graham, S. P. Tay, D. T. Jiang, and K. H. Tan, *J. Vac. Sci. Tech. B* **13**, 1626 (1995).

- [MAN00] G. Mannino, N. E. B. Cowern, F. Roozeboom, and J. G. M. van Berkum, *Appl. Phys. Lett.* **76**, 855 (2000).
- [MAN01] G. Mannino, S. Solmi, V. Privitera, and M. Bersani, *Appl. Phys. Lett.* **79**, 3764 (2001).
- [MAO86] B. -Y. Mao, P. -H. Chang, H. W. Lam, B. W. Shen, and J. A. Keenan, *Appl. Phys. Lett.* **48**, 794 (1986).
- [MAR50] UT-Marlowe Version 5.0, University of Texas-Austin.
- [MAS01] M. Mastrapasqua, D. Esseni, G. K. Celler, C. Fiegna, L. Selmi, and E. Sangiorgi, *Microelectronic Engineering* **59**, 409 (2001).
- [MIL96] S. Milita and M. Servidori, *J. Appl. Phys.* **79**, 8278 (1996).
- [MIR03] S. Mirabella, E. Bruno, F. Priolo, D. De Salvador, E. Napolitani, A. V. Drigo, and A. Carnera, *Appl. Phys. Lett.* **83**, 680 (2003).
- [MIY97] M. Miyake and M. Takahashi, *J. Electrochem. Soc.* **144**, 1020 (1997).
- [MOF95] S. Moffatt, *Nucl. Inst. Meth. Phys. Res. B* **96**, 1 (1995).
- [MOK02] A. Mokheri, P. B. Griffin, J. D. Plummer, E. Paton, S. McCoy, and K. Elliot, *IEEE Trans. Electron Dev.* **49**, 1183 (2002).
- [MOL98] K. Moller, K. S. Jones, and M. E. Law, *Appl. Phys. Lett.* **72**, 2547 (1998).
- [MOO65] G. E. Moore, *Electronics* **38**, 114 (1965).
- [NAK90] S. Nakashima and K. Izumi, *Electron. Lett.* **26**, 1647 (1990).
- [NIH04] NIH Image, <http://rsb.info.nih.gov/nih-image/Default.html>, 12/31/02.
- [NOD00] T. Noda, S. Odanaka, and H. Uemoto, *J. App. Phys.* **88**, 4980 (2000).
- [NOR89] P. Normand, D. Tsoukalas, N. Guillemot, and P. Chenevier, *J. Appl. Phys.* **66**, 3585 (1989).
- [NOR90] P. Normand, D. Tsoukalas, N. Guillemot, and J. Stoemenos, *J. Electrochem. Soc.* **137**, 2306 (1990).
- [OGU01] A. Ogura and M. Hiroi, *Thin Solid Films* **397**, 56 (2001).
- [OHR92] M. Ohring, *The Materials Science of Thin Films*, (Academic Press, San Diego, 1992) pp. 416-420.
- [OMR96] M. Omri, C. Bonafos, A. Claverie, A. Nejim, F. Cristiano, D. Alquier, A. Martinez, and N. E. B. Cowern, *Nucl. Instrum. Meth. Phys. Res. B* **120**, 5 (1996).

- [PAN75] S. T. Pantelides and W. A. Harrison, *Phys. Rev. B* **13**, 2667 (1975).
- [PAN04] Pananalytic website, <http://www.pananalytic.com>, 6/15/04.
- [PAR95] H. Park, K. S. Jones, J. A. Slinkman, and M. E. Law, *J. Appl. Phys.* **78**, 3664 (1995).
- [PAR99] H. Park, E. C. Jones, P. Ronsheim, C. Cabral, Jr., C. D'Emic, G. M. Cohen, R. Young, and W. Rausch, *Tech. Dig. IEDM*, 337 (1999).
- [PAU58] L. J. van der Pauw, *Philips Res. Repts.* **13**, 1 (1958).
- [PAY92] M. C. Payne, M. P. Teter, D. C. Allan, T. A. Arias, and J. D. Joannopoulos, *Rev. Mod. Phys.* **64**, 1045 (1992).
- [PEL98] L. Pelaz, G. H. Gilmer, M. Jaraiz, S. B. Herner, H.-J. Gossmann, D. J. Eaglesham, G. Hobler, C. S. Rafferty, and J. Barbolla, *Appl. Phys. Lett.* **73**, 1421 (1998).
- [PEL99a] L. Pelaz, G. H. Gilmer, H. -J. Gossmann, C. S. Rafferty, M. Jaraiz, and J. Barbolla, *Appl. Phys. Lett.* **74**, 3657 (1999).
- [PEL99b] L. Pelaz, V. C. Venezia, H. -J. Gossmann, G. H. Gilmer, A. T. Fiory, C. S. Rafferty, M. Jaraiz, and J. Barbolla, *Appl. Phys. Lett.* **75**, 662 (1999).
- [PLO00] A. Plöbl and G. Kräuter, *Solid-State Electronics* **44**, 775 (2000).
- [PLU00] J. D. Plummer, M. D. Deal, and P. B. Griffin, *Silicon VLSI Technology: Fundamentals, Practice and Modeling*, (Prentice Hall, Upper Saddle River, NJ, 2000), pp. 113-115, 466-467.
- [RAD02] L. Radic, A. D. Lilak, and M. E. Law, *Appl. Phys. Lett.* **81**, 826 (2002).
- [RAF96] C. S. Rafferty, G. H. Gilmer, M. Jaraiz, D. J. Eaglesham, and H. -J. Gossmann, *Appl. Phys. Lett.* **68**, 2395 (1996).
- [RAI96] V. Raineri, S. Lombardo, F. Iacona, and F. La Via, *Nucl. Instrum. Meth. Phys. Res. B* **116**, 482 (1996).
- [ROB90] A. K. Robinson, K. J. Reeson, and P. L. F. Hemment, *J. Appl. Phys.* **68**, 4340 (1990).
- [RUC99] H. Rücker, B. Heinemann, D. Bolze, R. Kurps, D. Krüger, G. Lippert, and H. J. Osten, *Appl. Phys. Lett.* **74**, 3377 (1999).
- [SAA02a] A. F. Saavedra, J. Frazer, K. S. Jones, I. Avci, S. K. Earles, M. E. Law, and E. C. Jones, *J. Vac. Sci. Technol. B* **20**, 2243 (2002).
- [SAA02b] A. F. Saavedra, J. Frazer, D. Wrigley, K. S. Jones, I. Avci, S. K. Earles, M. E. Law, and E. C. Jones, *Mater. Res. Soc. Symp. Proc.* **717**, 95 (2002).

- [SAA04a] A. F. Saavedra, K. S. Jones, M. E. Law, and K. K. Chan, *J. Electrochem. Soc.* **151**, G266 (2004).
- [SAA04b] A. F. Saavedra, K. S. Jones, M. E. Law, and K. K. Chan, *Mat. Sci. Eng. B* **107**, 198 (2004).
- [SAA04c] A. F. Saavedra, A. C. King, K. S. Jones, E. C. Jones, and K. K. Chan, *J. Vac. Sci. Tech. B* **22**, 459 (2004).
- [SAI85] G. A. Sai-Halaszi, K. T. Short, and J. S. Williams, *IEEE Electron Dev. Lett.* **6**, 285 (1985).
- [SAK87] K. Sakamoto, K. Nishi, F. Ichikawa, and S. Ushio, *J. Appl. Phys.* **61**, 1553 (1987).
- [SAL00] H. Saleh, M. E. Law, S. Bharatan, K. S. Jones, V. Krishnamoorthy, and T. Buyuklimanli, *Appl. Phys. Lett.* **77**, 112 (2000).
- [SAS88] Y. Sasaki, K. Itoh, E. Inoue, S. Kishi, and T. Mitsuishi, *Solid-State Electronics* **31**, 5 (1988).
- [SAT95] Y. Sato, K. Imai, and E. Arai, *J. Electrochem. Soc.* **142**, 660 (1995).
- [SCH86] E. Scheid and P. Chenevier, *Phys. Status Solidi A* **93**, 523 (1986).
- [SCH98] D. K. Schroeder, *Semiconductor Material and Device Characterization*, 2nd ed. (John Wiley & Sons, New York, NY, 1998) pp. 510-528.
- [SCH00] E. Schroer, V. Privitera, F. Priolo, E. Napolitani, A. Carnera, and S. Moffatt, *Mat. Sci. Eng. B* **71**, 219 (2000).
- [SER87] M. Servidori, Z. Sourek, and S. Solmi, *J. Appl. Phys.* **62**, 1723 (1987).
- [SER88] M. Servidori and F. Cembali, *J. Appl. Cryst.* **21**, 176 (1988).
- [SER92] M. Servidori, F. Cembali, R. Fabbri, and A. Zani, *J. Appl. Cryst.* **25**, 46 (1992).
- [SER93] M. Servidori and R. Fabbri, *J. Phys. D* **26**, A22 (1993).
- [SHA03] L. Shao, J. Liu, Q. Y. Chen, and W. -K. Chu, *Mat. Sci. Eng. R* **42**, 65 (2003).
- [SHI01] A. Shima, T. Jinbo, N. Natsuaki, J. Ushio, J. H. Oh, K. Ono, and M. Oshima, *J. Appl. Phys.* **89**, 3458 (2001).
- [SHO03] W. Shockley, "Forming Semiconductive Devices by Ionic Bombardment," U.S. Patent 2,787,654.
- [SHO99] M. Shoji and S. Horiguchi, *J. Appl. Phys.* **85**, 2722 (1999).
- [SIG03] SIGEN website, <http://www.sigen.com>, 12/31/02.

- [SNO65] E. H. Snow, A. S. Grove, B. E. Deal, and C. T. Sah, *J. Electrochem. Soc.* **36**, 1664 (1965).
- [SOI03] SOITEC website, <http://www.soitec.com>, 12/31/02.
- [SOL91] S. Solmi, F. Baruffaldi, and R. Canteri, *J. Appl. Phys.* **69**, 2135 (1991).
- [SOL00] S. Solmi, M. Bersani, M. Sbeti, J. L. Hansen, and A. N. Larsen, *J. Appl. Phys.* **88**, 4547 (2000).
- [SPE81] V. S. Speriosu, *J. Appl. Phys.* **52**, 6094 (1981).
- [SRI00] J. F. Ziegler, SRIM 2000.
- [STA97] R. E. Stahlbush, *IEEE Trans. Nucl. Sci.* **44**, 2106 (1997).
- [STI88] G. Stinger, *Anal. Chem.* **60**, 1524 (1988).
- [STO09] G. G. Stoney, *Proceeding of the Royal Society of London A* **82**, 172 (1909).
- [STO95] P. A. Stolk, H. -J. Gossmann, D. J. Eaglesham, and J. M. Poate, *Appl. Phys. Lett.* **66**, 568 (1995).
- [STR00] B. G. Streetman and S. Banerjee, *Solid State Electronic Devices*, 5th ed. (Prentice Hall, Upper Saddle River, NJ, 2000), p. 274.
- [TAK02] Y. Takamura, A. Vailionis, A. F. Marshall, P. B. Griffin, and J. D. Plummer, *J. Appl. Phys.* **92**, 5503 (2002).
- [TAK91] S. Takeda and K. Ibe, *JEOL News* **29E**, 2 (1991).
- [TAK92] S. Takeda, S. Muto, and H. Hirata, *Mat. Res. Soc. Symp. Proc.* **262**, 209 (1992).
- [TAK94] S. Takeda, M. Kohyama, and K. Ibe, *Phil. Mag. A* **70**, 287 (1994).
- [TAK95] S. Takeda and T. Kamino, *Phys. Rev. B* **51**, 2148 (1995).
- [TAN83] K. Taniguchi, D. A. Antoniadis, and Y. Matsushita, *Appl. Phys. Lett.* **42**, 961 (1983).
- [TAU98] Y. Taur and T. H. Ning, *Fundamentals of Modern VLSI Devices*, (Cambridge University Press, Cambridge, UK, 1998), pp. 139-149.
- [THO12] J. J. Thomson, *Phil. Mag.* **23**, 449 (1912).
- [THO94] R. H. Thompson, Jr., Master's Thesis, University of Florida (1994).
- [TRU60] F. A. Trumbore, *Bell System Tech. Journal* **39**, 205 (1960).
- [TSA95] C. Tsamis, D. Tsoukalas, and P. Normand, *Microelectronic Eng.* **28**, 463 (1995).

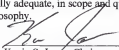
- [TSA98] C. Tsamis and D. Tsoukalas, *J. Appl. Phys.* **84**, 6650 (1998).
- [TSO93] D. Tsoukalas, C. Tsamis, and J. Stoemenos, *Appl. Phys. Lett.* **63**, 3167 (1993).
- [TSO01] D. Tsoukalas, C. Tsamis, and P. Normand, *J. Appl. Phys.* **89**, 7809 (2001).
- [TUK88] K. N. Tu and R. Rosenberg, *Analytical Techniques for Thin Films*, Vol. 27 of *Treatise on Materials Science and Technology* (Academic Press, Boston, MA, 1988), pp. 143-197.
- [UCH00] H. Uchida, Y. Ieki, M. Ichimura, and E. Arai, *Jpn. J. Appl. Phys.* **39**, L137 (2000).
- [VAN85] W. Vandervorst, F. R. Shepherd, and R. G. Downing, *J. Vac. Sci. Tech. A* **3**, 1318 (1985).
- [VAN01] A. Vandooren, S. Cristoloveanu, D. Flandre, and J. P. Colinge, *Solid-State Electronics* **45**, 1793 (2001).
- [VEE89] S. Veeraraghavan and J. G. Fossum, *IEEE Trans. on Electron Devices* **36**, 522 (1989).
- [VEN92] D. Venables, Ph. D. Dissertation, University of Florida (1992).
- [VUO99] H. -H. Vuong, H. -J. Gossmann, L. Pelaz, G. K. Celler, D. C. Jacobson, D. Barr, J. Hergenrother, D. Monroe, V. C. Venezia, C. S. Rafferty, S. J. Hillenius, J. McKinley, F. A. Stevie, and C. Granger, *Appl. Phys. Lett.* **75**, 1083 (1999).
- [VUO00] H. -H. Vuong, C. S. Rafferty, S. A. Eshraghi, J. Ning, J. R. McMacken, S. Chaudhry, J. McKinley, and F. A. Stevie, *J. Vac. Sci. Technol. B* **18**, 428 (2000).
- [WAN01] H. C. H. Wang, C. C. Wang, C. S. Chang, T. Wang, P. B. Griffin, and C. H. Diaz, *IEEE Electron Dev. Lett.* **22**, 65 (2001).
- [WAT66] M. Watanabe and A. Tooi, *Jpn. J. Appl. Phys.* **5**, 737 (1966).
- [WER98] P. Werner, H.-J. Gossmann, D. C. Jacobson, and U. Gösele, *Appl. Phys. Lett.* **73**, 2465 (1998).
- [WHI87] A. E. White, K. T. Short, J. L. Batstone, D. C. Jacobson, J. M. Poate, and K. W. West, *Appl. Phys. Lett.* **50**, 19 (1987).
- [WIE98] W. Wien, *Ann. Physik* **65**, 440 (1898).
- [WIE99] K. Wien, *Brazilian J. of Physics* **29**, 401 (1999).
- [WIL92] J. S. Williams, M. Petravic, Y. H. Li, J. A. Davies, and G. R. Palmer, *Nucl. Instrum. Meth. Phys. Res. B* **64**, 156 (1992).
- [WIL96] D. B. Williams and C. B. Carter, *Transmission Electron Microscopy*, (Plenum Press, New York, NY, 1996), pp. 423-437.

- [ZAN00] H. J. W. Zandvliet, *Rev. Mod. Phys.* **72**, 593 (2000).
- [ZHA95] L. H. Zhang, K. S. Jones, P. H. Chi, and D. S. Simons, *Appl. Phys. Lett.* **67**, 2025 (1995).
- [ZHA99] Y. Zhao, M. J. Aziz, H.-J. Gossmann, S. Mitha, and D. Shiferl, *Appl. Phys. Lett.* **74**, 31 (1999).
- [ZHO96] L. Zhong, K. Hayashi, and R. Takeda, *Appl. Phys. Lett.* **69**, 1247 (1996).
- [ZHU96] J. Zhu, T. D. de la Rubia, L. H. Yang, C. Mailhot, and G. H. Gilmer, *Phys. Rev. B* **54**, 4741 (1996).
- [ZIE00] J. F. Ziegler, *Ion Implantation Science and Technology*, (Ion Implantation Technology Co., Edgewater, MD, 2000), pp. 47-61, 335-337, 342-372.
- [ZOL98] E. Zolotoyabko, *J. Appl. Cryst.* **31**, 241 (1998).


BIOGRAPHICAL SKETCH

Antonio Fernando Saavedra, Jr. was born in Seabrook, Texas, a suburb of Houston, on October 30, 1977. His family moved to Muscle Shoals, Alabama, when he was two years old and resided there for 16 years. On June 4, 1996, he graduated from the prestigious Muscle Shoals High School with an Honors Diploma. He went on to the University of Alabama in Tuscaloosa to pursue a degree in engineering. Under the guidance of Drs. John Barnard, Ramana Reddy, and Mark Weaver he established himself within the Department of Metallurgical and Materials Engineering. He was conferred with a Bachelor of Science degree in metallurgical engineering at the level of *cum laude* on August 12, 2000. His interest in semiconductor technology took him to the Department of Materials Science and Engineering at the University of Florida in August of 2000 to pursue graduate study. There he studied under Drs. Kevin Jones and Mark Law in the areas of ion implantation, dopant diffusion, and activation for advanced silicon devices. He received the Master of Science degree on December 21, 2002. Upon receipt of the Doctor of Philosophy degree in August 2004, he will join Intel Corporation in Hillsboro, Oregon, in the Process Technology and Development sector.


I certify that I have read this study and that in my opinion it conforms to acceptable standards of scholarly presentation and is fully adequate, in scope and quality, as a dissertation for the degree of Doctor of Philosophy.


Kevin S. Jones, Chairman
Professor of Materials Science and
Engineering


I certify that I have read this study and that in my opinion it conforms to acceptable standards of scholarly presentation and is fully adequate, in scope and quality, as a dissertation for the degree of Doctor of Philosophy.


Mark E. Law
Professor of Electrical and Computer
Engineering

I certify that I have read this study and that in my opinion it conforms to acceptable standards of scholarly presentation and is fully adequate, in scope and quality, as a dissertation for the degree of Doctor of Philosophy.


Paul H. Holloway
Distinguished Professor of Materials
Science and Engineering

I certify that I have read this study and that in my opinion it conforms to acceptable standards of scholarly presentation and is fully adequate, in scope and quality, as a dissertation for the degree of Doctor of Philosophy.

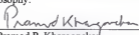

Cammy Abernathy
Professor of Materials Science and
Engineering

I certify that I have read this study and that in my opinion it conforms to acceptable standards of scholarly presentation and is fully adequate, in scope and quality, as a dissertation for the degree of Doctor of Philosophy.


Valentin Craciun
Assistant Scientist of Materials Science and
Engineering

This dissertation was submitted to the Graduate Faculty of the College of Engineering and to the Graduate School and was accepted as partial fulfillment of the requirements for the degree of Doctor of Philosophy.

August, 2004



Pramod P. Khargonekar
Dean, College of Engineering

Kenneth Gerhardt
Interim Dean, Graduate School

LD
1780
20.04

.S112

